Quantum Monte Carlo Studies of the BCS–BEC Crossover

Adam Richie-Halford

A dissertation
submitted in partial fulfillment of the
requirements for the degree of

Doctor of Philosophy

University of Washington

2020

Reading Committee:

Aurel Bulgac, Chair

Sanjay Reddy

Subhadeep Gupta

Program Authorized to Offer Degree:
Physics

University of Washington

Abstract

Quantum Monte Carlo Studies of the BCS–BEC Crossover

Adam Richie-Halford

Chair of the Supervisory Committee:
Professor Aurel Bulgac
Physics

This dissertation focuses on the physics of dilute Fermi gases in the so-called BCS–BEC crossover, with short-range attractive interactions and large scattering lengths. It introduces a new statistical ensemble, the particle asymmetry constrained ensemble, and uses it for calculations along with more conventional ensembles like the grand canonical ensemble and the canonical ensemble. The dissertation presents results for the energy, condensate fraction, superfluid critical temperature, spin susceptibility, even-odd energy pairing gap, and Tan contact and argues for the existence, or at least non-exclusion, of the pseudogap in the unitary regime with infinite scattering length. Finally, it uses the same quantum Monte Carlo techniques, this time in a zero-temperature setting, to determine the quasiparticle properties of infinite neutron matter, namely the effective mass, self-energy, and pairing gap.

TABLE OF CONTENTS

Page

LIST OF FIGURES

Figure Number Page

LIST OF TABLES

Table Number Page

GLOSSARY

AFQMC: auxiliary field quantum Monte Carlo.

BCS: Bardeen, Cooper, Schrieffer.

BEC: Bose-Einstein condensate.

DOS: density of states.

EFT: effective field theory.

EOS: equation of state.

FFG: free Fermi gas.

FFT: fast Fourier transform.

GCE: grand canonical ensemble.

GP: Gaussian process.

HS: Hubbard-Stratonovich.

HST: Hubbard-Stratonovich transformation.

INM: infinite neutron matter.

LO: leading order.

MCMC: Markov chain Monte Carlo.

MH: Metropolis-Hastings.

NLO: next-to-leading order.

N^{2}LO: next-to-next-to-leading order.

N^{3}LO: next-to-next-to-next-to-leading order.

PACE: particle asymmetry constrained ensemble.

QMC: quantum Monte Carlo.

QPE: quasiparticle excitation

RBF: radial basis function.

UFG: unitary Fermi gas.

UV: ultraviolet.

χ-EFT: chiral effective field theory.

ACKNOWLEDGMENTS

> Somewhere, something incredible is waiting to be known.
>
> Carl Sagan

> It does not take much to make us realize what fools we are,
> but the little it takes is long in coming.
>
> Flannery O'Connor

The quotes above sample the spectrum of my reactions to graduate studies. At times, physics has felt like the noblest pursuit, pushing at the frontiers of knowledge, venturing into the undiscovered country. At other times, it has felt like a fundamentally selfish endeavor, engrossing myself in mathematical curiosities while others make the world turn. The truth, of course, is somewhere in between and my development as a scientist has been marked not only by the acquisition of the technical skills necessary to perform my research, but more importantly, the life skills needed to connect meaningfully with it. I am indebted to so many people who fostered those skills in me.

First, I would like to thank my advisor, Prof. Aurel Bulgac for his patience and guidance over the years. I've lost track of all the times I've figured something out "on my own" only to realize that the thing I figured out was something Aurel was trying to explain to me earlier. I'm probably not done having that experience. I am also grateful for the help of my collaborators Gabriel Wlazłowski, Jeremy Holt, and Joaquín Drut, who shared with me their capacious minds, physical intuition, and enduring patience. I thank Kenny Roche for his technical expertise in computing, parenting advice (both accepted and rejected), and his loquaciousness on all other topics. Profs. Sanjay Reddy and Subhadeep Gupta volunteered their limited time on an accelerated review schedule during a global pandemic, all to make this document better. Finally, I must also thank the broader University of Washington community for providing me with an intellectual home over these years.

I had a non-traditional route to obtaining my Ph.D. and I am grateful for my research and professional mentors before I came to the University of Washington. I am deeply grateful for the guidance and friendship of M. Anthony Reynolds, Andreas Bill (along with the entire Department of Physics and Astronomy at California State University, Long Beach), John W. Armstrong, and Richard Woo, each of whom spurred my curiosity and pushed me to be a better scientist, communicator, and person.

I also thank my friends, family, and colleagues for their guidance, love, and support. I lack the literary skill to say this without sounding treacly but my mother and father, Deborah Richie and Carl Halford, are true role models for me and I thank them for their love, support, curiosity, and humor. My wife, Zoë True, knows me best of anyone and sticks around for some reason. She brings out the best in me and suffers my incoherent attempts to to explain my work in layman's terms. I am unfathomably fortunate to have found her. My daughter, Ida True, has given me the opportunity to grow up all over again and collaborate in our daily redefinition of love. Research time is either a theft or a loan from Zoë and Ida. If it is the latter, I will work as hard as I can to repay it.

I am also indebted to my colleagues and friends Ariel Rokem, Jason Yeatman, and Anisha Keshavan, who fostered a research interest in neuroimaging that became meaningful to me after my own neurosurgery. My nascent work with them is not described in this thesis but forms the basis of my postdoctoral research.

I would like to thank my friends and classmates who have composed my second family over the years. Thanks to the "father camping" crew, my climbing buddies who have literally held my life in their hands, Nick Abbott, Elizabeth Lhost, Audrey Lawrence, Nathan Royston, and my many friends who will never read this but whose love and support is woven throughout.

DEDICATION

To my dearest liver, Zoë.

Chapter 1

INTRODUCTION

This chapter introduces basic concepts in quantum mechanics necessary to understand the contributions of this dissertation.

1.1 Fermi and Bose gases

Elementary (and compound) particles can be classified according to their quantum mechanical statistical properties as either bosons or fermions. Particles of half odd integer spin (e.g. $1/2$, $3/2$, etc.) are fermions, obey Fermi-Dirac statistics, and obey the Pauli exclusion principle, which states that only one fermion may occupy a given quantum state at a given time. Conversely, particles of integer spin (e.g. 0, 1, etc.) are bosons, obey Bose-Einstein statistics, and may simultaneously occupy the same quantum state as many other bosons.

We will introduce the Bose-Einstein and Fermi-Dirac statistics in the context of non-interacting gases and see that even in the absence of interactions, the statistical rules give rise to rich, even macroscopic, quantum mechanical phenomena. But before differentiating the Fermi-Dirac from the Bose-Einstein statistics, let us introduce some basic formalism of statistical mechanics. For a quantum system with Hamiltonian $\hat{H}$, at temperature T, with chemical potential μ, and volume V, all of the relevant statistical information can be derived from the grand-canonical partition function, which measures the extent to which the particles are spread out over the system's energy levels,

$$\mathcal{Z}(\beta, \mu, V) = \operatorname{Tr} e^{-\beta\left(\hat{H} - \mu\hat{N}\right)}, \tag{1.1}$$

where $\beta = 1/k_B T$, $\hat{N}$ is the particle number operator and the trace is over all possible multi-particle states, known as Fock space. The constant k_B is Boltzmann's constant and for the remainder of this dissertation, we will choose units in which $k_B = 1$ so that we can write $\beta = 1/T$. The Hamiltonian $\hat{H}$ may be decomposed into kinetic energy and potential energy terms, $\hat{H} = \hat{K} + \hat{V}$, where $\hat{K}$ is a one-body operator that depends on the momentum, p, of each particle. For much of this dissertation, we assume that the potential is a two-body operator that depends on the separation between particles.

1.1.1 Bosons and Bose-Einstein condensation

For a system of non-interacting bosons with an arbitrary generic energy spectrum ϵ_k, the grand canonical partition function is

$$\mathcal{Z}(\beta,\mu,V) = \sum_{N=0}^{\infty}\sum_{\{n_k\}} \exp\left[-\beta\sum_k\left(\epsilon_k-\mu\right)n_k\right] = \prod_k \frac{1}{1-e^{-\beta(\epsilon_k-\mu)}}, \tag{1.2}$$

where the summations combine to give the trace over Fock space: N is the total particle number, n_k is the occupation number of the quantum state k. For bosons, n_k can take any value from 0 to ∞. By inspection of Eq. (1.1), the total particle number is

$$N = \frac{\partial \ln \mathcal{Z}}{\partial\left(\beta\mu\right)} = \sum_k n_k = \sum_k \frac{1}{e^{\beta(\epsilon_k-\mu)}-1}. \tag{1.3}$$

In the thermodynamic limit, $V \to \infty$ and we can replace the discrete sum in Eq. (1.3) by an integral

$$n = \frac{N}{V} = \frac{2\pi(2m)^{3/2}}{(2\pi\hbar)^3}\int_0^{\infty}\frac{\varepsilon^{1/2}\,\mathrm{d}\varepsilon}{e^{\beta(\varepsilon-\mu)}-1}, \tag{1.4}$$

where m is the particle mass. If we take N and V (and therefore n) to be fixed, then the chemical potential is a function of temperature, $\mu = \mu(T)$ and varies in order to enforce a desired density at a particular temperature. Formally, the definition of the chemical potential is[112]

$$\mu = \left(\frac{\partial U}{\partial N}\right)_{S,V}, \tag{1.5}$$

where U is the internal energy and S is the entropy. So then μ is the energy required to add a single particle to the system under constant entropy and volume. Adding an extra particle should increase the entropy of the system by increasing the number of states available to each particle (i.e. increasing the possible distributions $\{n_k\}$ in Eq. (1.2)). Holding S constant therefore requires a decrease in the internal energy. So the sign of μ is negative.

To put it another way, since n_k must be non-negative for all states k, this implies that $\mu \leq \epsilon_k$, for all k, including the ground state $|\mathbf{k}=0\rangle$, where $\epsilon_k = 0$. Therefore, we know that for the Bose gas, the chemical potential must satisfy $\mu \leq 0$. As we lower the temperature of the system (i.e. increase β), the particle (or density) constraint will require that the chemical potential increases until it reaches the value $\mu = 0$ at some temperature T_0. If we cool the gas further below T_0, then Eq. (1.5) dictates that the constraint $\mu = 0$ will only hold if the change in internal energy is zero. So cooling the system below T_0 will keep the internal energy constant, which can be satisfied when the particles collapse spontaneously to a single particle energy state. This results in a large occupation of the $|\mathbf{k}=0\rangle$ state, a phenomenon known as Bose-Einstein condensation[27, 65, 7]. The temperature T_0 is the critical temperature that separates the normal phase of the gas from the Bose-Einstein condensate (BEC) phase. In three dimensions and with the energy spectrum $\epsilon_k = \hbar^2 k^2/2m$, the critical temperature is[118]

$$T_0 \approx 3.31 \frac{\hbar^2}{m} \left(\frac{N}{V}\right)^{2/3} . \tag{1.6}$$

1.1.2 Fermions

Since fermions obey the Pauli exclusion principle, the occupation numbers are constrained to $n_k \in \{0, 1\}$. So the fermionic grand canonical partition function becomes

$$\mathcal{Z}(\beta, \mu, V) = \prod_k \sum_{n_k=0}^{1} \exp\left[-\beta \left(\sum_k (\epsilon_k - \mu) n_k\right)\right] = \prod_k \{1 + \exp\left[-\beta (\epsilon_k - \mu)\right]\} . \tag{1.7}$$

Unlike the Bose gas, where particles can all occupy the lowest state, the particles in the Fermi gas fill up the energy states according to the occupation probability

$$n_k = \frac{1}{e^{\beta(\epsilon_k - \mu)} + 1}, \tag{1.8a}$$

$$\lim_{\beta\to\infty} n_k = 1 - \Theta\left(\epsilon_k - \mu\right), \tag{1.8b}$$

where Θ is the Heaviside step function. Thus, at zero temperature, n_k becomes a step function and all states up to the so called Fermi energy ε_F are occupied, with all higher states empty. In three dimensions and with the dispersion relation $\epsilon_k = \hbar^2 k^2/2m$, the Fermi energy is given by[118]

$$\varepsilon_F = \frac{\hbar^2 k_F^2}{2m}, \quad \text{where} \quad k_F = \left(3\pi^2 \frac{N}{V}\right)^{1/3}, \tag{1.9}$$

where k_F is the Fermi momentum. The total energy of the free Fermi gas at zero temperature is

$$E_{FFG} = \frac{3}{5} N \varepsilon_F. \tag{1.10}$$

1.1.3 Boltzmann gases: the classical limit

Both the Fermi and Bose gases behave the same in the classical limit. If we take the average interparticle spacing of the gas to be $(V/N)^{1/3}$, and take the thermal de Broglie wavelength of the gas, λ_{th}, to be the average de Broglie wavelength of the particles, then the classical limit is the case where the thermal de Broglie wavelength is much smaller than the interparticle spacing,

$$\lambda_{\text{th}} \ll \left(\frac{V}{N}\right)^{1/3} \tag{1.11}$$

This inequality can be satisfied from the right-hand-side by making the gas very dilute, or from the left-hand-side by increasing the temperature. In either case, the Fermi-Dirac and Bose-Einstein distributions approach the classical Boltzmann distribution,

$$n_k = \frac{1}{e^{\beta(\epsilon_k - \mu)} \pm 1} \to e^{-\beta(\epsilon_k - \mu)}, \tag{1.12}$$

since $\beta\left(\epsilon_k - \mu\right) \gg 1$.

1.2 Interactions

We have seen that the statistical properties of a gas lead to drastically different behavior even in the absence of interactions. Once we add interactions to the picture, it is difficult to compute analytically the partition function. Indeed, one can view the rest of this thesis as an attempt to estimate accurately the partition function in a few important limiting cases. We can however, gain some intuition about the effect of the interactions by looking at the mean-field models of interacting fermions and bosons.

1.2.1 BCS superconductivity

Bardeen, Cooper, and Schrieffer[14, 13] (BCS) first developed a theory of superconductivity, in which some metals exhibit zero electrical resistance below a certain critical temperature. In doing so, they introduced the important concept of pairing, in which $|k, \uparrow\rangle$ and $|-k, \downarrow\rangle$ states form bound pairs near the Fermi surface, thereby lowering the system's energy. We will investigate the onset of superconductivity by assuming these pairs exist and considering the effective Hamiltonian

$$\hat{H} = \sum_{\mathbf{k}\sigma} \xi_{\mathbf{k}} \hat{c}^{\dagger}_{\mathbf{k}\sigma} \hat{c}_{\mathbf{k}\sigma} + \sum_{\mathbf{k}\mathbf{k}'} V_{\mathbf{k}\mathbf{k}'} \hat{c}^{\dagger}_{\mathbf{k}\uparrow} \hat{c}^{\dagger}_{-\mathbf{k}\downarrow} \hat{c}_{-\mathbf{k}'\downarrow} \hat{c}_{\mathbf{k}'\uparrow}, \tag{1.13}$$

where $\hat{c}^{\dagger}_{\mathbf{k}\sigma}$ creates a particle with momentum $\mathbf{k}$ and spin σ, we have used $\xi_k \equiv \epsilon_k - \mu$ to concisely include the chemical potential, and we assume that the interaction strength $V_{\mathbf{k}\mathbf{k}'}$ is weakly attractive. The second term in Eq. (1.13) describes the annihilation of one Cooper pair with momentum $\pm\mathbf{k}'$ and the creation of another with $\pm\mathbf{k}$. We can then perform a mean-field decoupling of the quartic term using

$$\begin{aligned} \left\langle \hat{c}^{\dagger}_{\mathbf{k}\uparrow} \hat{c}^{\dagger}_{-\mathbf{k}\downarrow} \hat{c}_{-\mathbf{k}'\downarrow} \hat{c}_{\mathbf{k}'\uparrow} \right\rangle \approx \left\langle \hat{c}^{\dagger}_{\mathbf{k}\uparrow} \hat{c}^{\dagger}_{-\mathbf{k}\downarrow} \right\rangle \hat{c}_{-\mathbf{k}'\downarrow} \hat{c}_{\mathbf{k}'\uparrow} + \hat{c}^{\dagger}_{\mathbf{k}\uparrow} \hat{c}^{\dagger}_{-\mathbf{k}\downarrow} \left\langle \hat{c}_{-\mathbf{k}'\downarrow} \hat{c}_{\mathbf{k}'\uparrow} \right\rangle \\ - \left\langle \hat{c}^{\dagger}_{\mathbf{k}\uparrow} \hat{c}^{\dagger}_{-\mathbf{k}\downarrow} \right\rangle \left\langle \hat{c}_{-\mathbf{k}'\downarrow} \hat{c}_{\mathbf{k}'\uparrow} \right\rangle, \end{aligned} \tag{1.14}$$

where the expectation value $\langle \hat{c}^{\dagger}_{\mathbf{k}\uparrow} \hat{c}^{\dagger}_{-\mathbf{k}\downarrow} \rangle$ corresponds to a single Cooper pair in the superconducting state. Using suggestive notation, we can define the gap function as

$$\Delta_{\mathbf{k}} = -\sum_{\mathbf{k}'} V_{\mathbf{k}\mathbf{k}'} \left\langle \hat{c}_{-\mathbf{k}'\downarrow} \hat{c}_{\mathbf{k}'\uparrow} \right\rangle, \tag{1.15}$$

which simplifies the expression of the effective Hamiltonian,

$$\hat{H} = \sum_{\mathbf{k}\sigma} \xi_{\mathbf{k}} \hat{c}^{\dagger}_{\mathbf{k}\sigma} \hat{c}_{\mathbf{k}\sigma} - \sum_{\mathbf{k}} \left[\Delta_{\mathbf{k}} \hat{c}^{\dagger}_{\mathbf{k}\uparrow} \hat{c}^{\dagger}_{-\mathbf{k}\downarrow} + \Delta^{*}_{\mathbf{k}} \hat{c}_{-\mathbf{k}\downarrow} \hat{c}_{\mathbf{k}\uparrow} \right] + \sum_{\mathbf{k}} \Delta_{\mathbf{k}} \left\langle \hat{c}^{\dagger}_{\mathbf{k}\uparrow} \hat{c}^{\dagger}_{-\mathbf{k}\downarrow} \right\rangle. \tag{1.16}$$

This can be solved by using a Bogoliubov transform[24, 25, 197] to define new fermionic quasiparticle operators.

$$\begin{aligned} \hat{c}_{\mathbf{k}\uparrow} &= u_{\mathbf{k}}^{*}\hat{\gamma}_{\mathbf{k}\uparrow} + v_{\mathbf{k}}\hat{\gamma}_{-\mathbf{k}\downarrow}^{\dagger}, \\ \hat{c}_{-\mathbf{k}\downarrow} &= u_{\mathbf{k}}\hat{\gamma}_{-\mathbf{k}\downarrow}^{\dagger} - v_{\mathbf{k}}^{*}\hat{\gamma}_{\mathbf{k}\uparrow}, \end{aligned} \tag{1.17}$$

where $u_{\mathbf{k}}$ and $v_{\mathbf{k}}$ must satisfy

$$|u_{\mathbf{k}}|^2 + |v_{\mathbf{k}}|^2 = 1 \tag{1.18}$$

in order to preserve the fermionic commutation relations. Rearranging Eq. (1.17), we have

$$\begin{aligned} \hat{\gamma}_{\mathbf{k}\uparrow} &= u_{\mathbf{k}}\hat{c}_{\mathbf{k}\uparrow} - v_{\mathbf{k}}\hat{c}_{-\mathbf{k}\downarrow}^{\dagger}, \\ \hat{\gamma}_{-\mathbf{k}\downarrow}^{\dagger} &= u_{\mathbf{k}}^{*}\hat{c}_{-\mathbf{k}\downarrow}^{\dagger} + v_{\mathbf{k}}^{*}\hat{c}_{\mathbf{k}\uparrow}, \end{aligned} \tag{1.19}$$

and can see that the Bogoliubov quasiparticles are mixtures of our original particles and holes.

Plugging Eq. (1.17) into the effective Hamiltonian in Eq. (1.16) and collecting terms by powers of the quasiparticle operators yields

$$\begin{aligned} \hat{H} = \sum_{\mathbf{k}} & \left[2\xi_{\mathbf{k}}|v_{\mathbf{k}}|^2 - \Delta_{\mathbf{k}}u_{\mathbf{k}}v_{\mathbf{k}}^{*} - \Delta_{\mathbf{k}}^{*}u_{\mathbf{k}}^{*}v_{\mathbf{k}} + \Delta_{\mathbf{k}}\left\langle \hat{c}_{\mathbf{k}\uparrow}^{\dagger}\hat{c}_{-\mathbf{k}\downarrow}^{\dagger}\right\rangle\right] \\ & + \sum_{\mathbf{k}} \left[\xi_{\mathbf{k}}\left(|v_{\mathbf{k}}|^2 - |v_{\mathbf{k}}|^2\right) + \Delta_{\mathbf{k}}u_{\mathbf{k}}v_{\mathbf{k}}^{*} + \Delta_{\mathbf{k}}^{*}u_{\mathbf{k}}^{*}v_{\mathbf{k}}\right]\left(\hat{\gamma}_{\mathbf{k}\uparrow}^{\dagger}\hat{\gamma}_{\mathbf{k}\uparrow} + \hat{\gamma}_{-\mathbf{k}\downarrow}^{\dagger}\hat{\gamma}_{-\mathbf{k}\downarrow}\right) \\ & + \sum_{\mathbf{k}} \left[2\xi_{\mathbf{k}}u_{\mathbf{k}}v_{\mathbf{k}} - \Delta_{\mathbf{k}}u_{\mathbf{k}}^2 + \Delta_{\mathbf{k}}^{*}v_{\mathbf{k}}^2\right]\left(\hat{\gamma}_{\mathbf{k}\uparrow}^{\dagger}\hat{\gamma}_{-\mathbf{k}\downarrow}^{\dagger}\right) \quad + \quad \text{h.c.} \quad , \end{aligned} \tag{1.20}$$

where h.c. signifies the hermitian conjugate. Up to the normalization condition, we are still free to choose $u_{\mathbf{k}}$ and $v_{\mathbf{k}}$ so we choose values such that the last summation in Eq. (1.20) goes to zero and we can bring the effective Hamiltonian into diagonalizable quadratic form. This requires

$$2\xi_{\mathbf{k}}u_{\mathbf{k}}v_{\mathbf{k}} - \Delta_{\mathbf{k}}u_{\mathbf{k}}^2 + \Delta_{\mathbf{k}}^{*}v_{\mathbf{k}}^2 = 0. \tag{1.21}$$

Solving for the coefficients and choosing only the root that gives a minimum BCS energy yields

$$\frac{v_{\mathbf{k}}}{u_{\mathbf{k}}} = \frac{\sqrt{\xi_{\mathbf{k}}^2 + |\Delta_{\mathbf{k}}|^2} - \xi_{\mathbf{k}}}{\Delta_{\mathbf{k}}^{*}}. \tag{1.22}$$

Combining this with the normalization condition in Eq. (1.18) yields

$$|u_{\mathbf{k}}|^2 = \frac{1}{2}\left(1 + \frac{\xi_{\mathbf{k}}}{E_{\mathbf{k}}}\right), \tag{1.23a}$$

$$|v_{\mathbf{k}}|^2 = \frac{1}{2}\left(1 - \frac{\xi_{\mathbf{k}}}{E_{\mathbf{k}}}\right), \tag{1.23b}$$

where

$$E_{\mathbf{k}} = \sqrt{\xi_{\mathbf{k}}^2 + |\Delta_{\mathbf{k}}|^2}, \tag{1.23c}$$

is the excitation energy of the Bogoliubov quasiparticles. We can now write the effective Hamiltonian as

$$\hat{H} = \sum_{\mathbf{k}\sigma} E_{\mathbf{k}} \hat{\gamma}^{\dagger}_{\mathbf{k}\sigma} \hat{\gamma}_{\mathbf{k}\sigma} + \sum_{\mathbf{k}} \left(\xi_{\mathbf{k}} - E_{\mathbf{k}} + \Delta_{\mathbf{k}} \left\langle \hat{c}^{\dagger}_{\mathbf{k}\uparrow} \hat{c}^{\dagger}_{-\mathbf{k}\downarrow} \right\rangle \right). \tag{1.24}$$

Now that we have the excitation spectrum and coefficient magnitudes in Eq. (1.23), we can interpret the quasiparticles that we have been using all along. Even at the Fermi level, where $\xi_{\mathbf{k}} = 0$, the excitation spectrum has a gap of size $|\Delta_{\mathbf{k}}|$. The density of states (DoS) becomes zero inside this gap[1]. We therefore require a minimum energy of $2|\Delta_{\mathbf{k}}|$ to excite the quasiparticle. For $\xi_{\mathbf{k}} \gg \Delta_{\mathbf{k}}$, $u_{\mathbf{k}} \to 1$, while for $\xi_{\mathbf{k}} \ll -\Delta_{\mathbf{k}}$, $v_{\mathbf{k}} \to 1$. Thus, far away from the Fermi surface, the quasiparticles (and quasi-holes) described by the operators $\hat{\gamma}$ become essentially identical to the original particles (and holes) described by the operators $\hat{c}$. However, when the gap $\Delta_{\mathbf{k}}$ is large enough and we are close enough to the Fermi surface, the quasiparticles are superpositions of particles and holes.

The gap $\Delta_{\mathbf{k}}$ may be calculated by substituting the operators in Eq. (1.17) into the gap definition in Eq. (1.15) so that

$$\langle \hat{c}_{-\mathbf{k}\downarrow} \hat{c}_{\mathbf{k}\uparrow} \rangle = u_{\mathbf{k}} v_{\mathbf{k}} \left[\left\langle \hat{\gamma}_{-\mathbf{k}\downarrow} \hat{\gamma}^{\dagger}_{-\mathbf{k}\downarrow} \right\rangle - \left\langle \hat{\gamma}^{\dagger}_{\mathbf{k}\uparrow} \hat{\gamma}_{\mathbf{k}\uparrow} \right\rangle \right] = u_{\mathbf{k}} v_{\mathbf{k}} \left[1 - \langle \hat{n}^{\mathrm{qp}}_{\mathbf{k}\uparrow} \rangle - \langle \hat{n}^{\mathrm{qp}}_{\mathbf{k}\downarrow} \rangle \right], \tag{1.25}$$

where $\hat{n}^{\mathrm{qp}}$ is the quasiparticle number operator. Since the quasiparticles obey Fermi-Dirac statistics and have an energy dispersion $E_{\mathbf{k}}$, we have

$$1 - \langle \hat{n}^{\mathrm{qp}}_{\mathbf{k}\uparrow} \rangle - \langle \hat{n}^{\mathrm{qp}}_{\mathbf{k}\downarrow} \rangle = 1 - \frac{2}{e^{\beta E_{\mathbf{k}}} + 1} = \tanh\left(\frac{1}{2}\beta E_{\mathbf{k}}\right) \tag{1.26}$$

---

[1] We will return to this cancellation in the DoS in § 1.3 when we discuss the pseudogap.

By combining Eqs. (1.22), (1.23) and (1.26), we have the BCS gap equation

$$\Delta_{\mathbf{k}} = -\frac{1}{2}\sum_{\mathbf{k}'} V_{\mathbf{k}\mathbf{k}'}\frac{\Delta_{\mathbf{k}'}}{E_{\mathbf{k}'}}\tanh\left(\frac{1}{2}\beta E_{\mathbf{k}'}\right), \tag{1.27}$$

which must be solved self-consistently. In the continuum limit, the gap equation becomes an integral equation

$$\Delta(\mathbf{p}) = -\frac{1}{2}\int\frac{\mathrm{d}p'}{(2\pi)^3}V\left(\mathbf{p}-\mathbf{p}'\right)\frac{\Delta(\mathbf{p}')}{E(\mathbf{p}')}\tanh\left(\frac{1}{2}\beta E(\mathbf{p}')\right), \tag{1.28}$$

which is UV divergent and must be regularized. We can regularize the integral by setting the physical scale of the problem to be a, the s-wave scattering length, described in Appendix A.

Restricting the potential to a two-body contact interaction of the form

$$\hat{V} = \sum_r g\hat{n}_\uparrow(r)\hat{n}_\downarrow(r), \tag{1.29}$$

the BCS gap equation can be written as

$$\frac{1}{g} = \int \mathrm{d}^3p\,\frac{1}{2E(p)}\tanh\left(\frac{1}{2}\beta E(p)\right), \tag{1.30}$$

where we have used the s-wave gap assumption, $\Delta_{\mathbf{k}} = \Delta \in \mathbb{R}$. We can relate the s-wave scattering length a to the bare coupling g using

$$\frac{m}{4\pi a} = \int\frac{\mathrm{d}^3p}{2\epsilon(p)} - \frac{1}{g}, \tag{1.31}$$

which has been computed for various lattice cutoffs and dispersion relations by Werner and Castin[204]. Combining Eqs. (1.30) and (1.31), we get

$$\frac{m}{4\pi a} = \int \mathrm{d}^3p\left[\frac{1}{2\epsilon(p)} - \frac{1}{2E(p)}\tanh\left(\frac{1}{2}\beta E(p)\right)\right], \tag{1.32a}$$

$$n = \frac{1}{V}\int \mathrm{d}^3p\left[1 - \frac{\xi(p)}{E(p)}\tanh\left(\frac{1}{2}\beta E(p)\right)\right], \tag{1.32b}$$

where the first equation is the gap equation and the second is the so-called number equation which accounts for the change in chemical potential required to keep a fixed density. These can be solved to obtain the chemical potential and gap for a given temperature. Because of the first term in brackets in Eq. (1.32a), the gap equation integral is no longer UV divergent.

In the weak coupling limit and at $T = 0$, we can solve the gap equation in Eq. (1.32a) without using the number equation in Eq. (1.32b), setting $\mu = \varepsilon_F$, yielding

$$\Delta(T=0) = \frac{8\varepsilon_F}{e^2} \exp\left(-\frac{\pi}{2|k_F a|}\right). \tag{1.33}$$

As we increase the temperature, the quasiparticle excitations block the available energy levels, reducing the gap parameter, which decreases from its maximum value at $\Delta(T = 0)$, vanishing to zero at

$$T_c = \frac{e^\gamma}{\pi}\Delta(T=0), \tag{1.34}$$

where γ is the Euler-Mascheroni constant, $\gamma \approx 0.577$, not to be confused with the quasiparticle operator $\hat{\gamma}$. This result as well as Eq. (1.33) was first calculated by Gor'kov and Melik-Barkhudarov in 1961[87].

1.2.2 Superfluidity

The same type of transformation used for weakly attractively interacting fermions in § 1.2.1 can be applied to the case of repulsively interacting bosons. In fact, the original application of Bogoliubov's theory was of this type, applied to liquid helium[24]. Writing the Hamiltonian in momentum space as

$$\hat{H} = \sum_{\mathbf{k}} \epsilon_{\mathbf{k}} \hat{a}^\dagger_{\mathbf{k}} \hat{a}_{\mathbf{k}} + \frac{U_0}{2V} \sum_{\mathbf{p},\mathbf{k},\mathbf{q}} \hat{a}^\dagger_{\mathbf{p}+\mathbf{q}} \hat{a}^\dagger_{\mathbf{k}-\mathbf{q}} \hat{a}_{\mathbf{k}} \hat{a}_{\mathbf{p}}, \tag{1.35}$$

where $\hat{a}^\dagger_{\mathbf{k}}$ creates a boson with momentum $\mathbf{k}$, $\epsilon_{\mathbf{k}} = \hbar^2 k^2/2m$, and $\hat{a}^\dagger_{\mathbf{k}}$ and $\hat{a}_{\mathbf{k}}$ obey the usual bosonic commutation relations.

As mentioned in § 1.1.1, the lowest-lying single-particle state (denoted by subscript 0) will be macroscopically occupied below a certain critical temperature. If N_0 is the number of particles in this state, then N_0/N will be finite even in the thermodynamic limit where N and V go to infinity while keeping the density $n = N/V$ constant. We will rewrite the Hamiltonian by pulling out the lowest lying state, rewriting $\hat{a}^\dagger_0 \hat{a}_0 = N_0$ and applying the

Bogoliubov transformation

$$\begin{aligned} \hat{a}_{\mathbf{k}} &= u_{\mathbf{k}}\hat{\alpha}_{\mathbf{k}} - v_{\mathbf{k}}\hat{\alpha}^{\dagger}_{-\mathbf{k}}, \\ \hat{a}_{-\mathbf{k}} &= u_{\mathbf{k}}\hat{\alpha}_{-\mathbf{k}} - v_{\mathbf{k}}\hat{\alpha}^{\dagger}_{\mathbf{k}}, \end{aligned} \tag{1.36}$$

where u and v may be chosen to be real. The Hamiltonian then becomes

$$\hat{H} = \frac{N_0^2 U_0}{2V} + \sum_{\mathbf{k}\neq 0}\left[E_{\mathbf{k}}\hat{\alpha}^{\dagger}_{\mathbf{k}}\hat{\alpha}_{\mathbf{k}} - \frac{1}{2}\left(\epsilon_{\mathbf{k}} + n_0 U_0 - E_{\mathbf{k}}\right)\right], \tag{1.37}$$

where $n_0 = N_0/V$ and $E_{\mathbf{k}} = \sqrt{\epsilon_{\mathbf{k}}^2 + 2\epsilon_{\mathbf{k}} n_0 U_0}$

In this bosonic case, the Bogoliubov coefficients satisfy the normalization condition

$$u_{\mathbf{k}}^2 - v_{\mathbf{k}}^2 = 1, \tag{1.38}$$

and their magnitudes satisfy

$$u_{\mathbf{k}}^2 = \frac{1}{2}\left(\frac{\xi_{\mathbf{k}}}{E_{\mathbf{k}}} + 1\right), \tag{1.39a}$$

$$v_{\mathbf{k}}^2 = \frac{1}{2}\left(\frac{\xi_{\mathbf{k}}}{E_{\mathbf{k}}} - 1\right), \tag{1.39b}$$

where $\xi_{\mathbf{k}}$ is the energy measured from the chemical potential as before.

At small momenta, the dispersion relation satisfies,

$$\lim_{k\ll 1} E_{\mathbf{k}} = sk, \tag{1.40}$$

where $s = \sqrt{n_0 U_0/m}$, which satisfies Landau's criterion for superfluidity[117], whereby a quantum fluid flows without dissipation below a certain critical velocity,

$$v_c = \min_k\left(\frac{E_k}{k}\right). \tag{1.41}$$

For the interacting Bose gas, the critical velocity is

$$v_c = s = \sqrt{\frac{n_0 U_0}{m}}. \tag{1.42}$$

1.2.3 BCS–BEC crossover

In § 1.2.1, we solved for the gap in the low coupling regime. However, there is no reason we cannot just blindly solve Eq. (1.32) to see what the behavior is at different coupling strengths. Let us look at the zero temperature behavior of Δ and μ so that all factors of $\tanh(\beta E/2) \to 1$. Equation (1.32) is more manageable in its dimensionless form

$$\frac{\pi}{2k_F a} = \int_0^\infty \mathrm{d}x \left[1 - \frac{x^2}{\sqrt{\left(x^2 - \widetilde{\mu}\right)^2 + \widetilde{\Delta}^2}}\right], \tag{1.43a}$$

$$\frac{2}{3} = \int_0^\infty \mathrm{d}x\, x^2 \left[1 - \frac{x^2 - \widetilde{\mu}}{\sqrt{\left(x^2 - \widetilde{\mu}\right)^2 + \widetilde{\Delta}^2}}\right], \tag{1.43b}$$

where the tildes on $\widetilde{\mu}$ and $\widetilde{\Delta}$ indicate that they are measured in units of the Fermi energy ε_F. In Fig. 1.1 we show our solutions for $\widetilde{\Delta}$ and $\widetilde{\mu}$ for a range of scattering lengths.

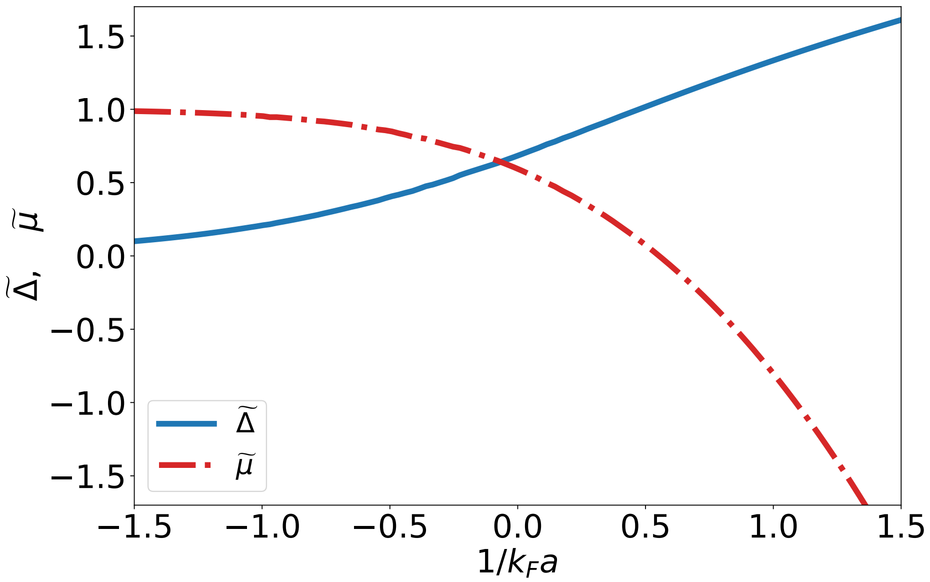

Figure 1.1: Gap and chemical potential (in units of ε_F) throughout the BCS–BEC crossover using the BCS gap equation and number equation in Eq. (1.43).

There is no reason to trust the accuracy of these results since they were derived in the weak coupling limit and are being applied across a wide range of scattering lengths. However, as Eagles[63] and Leggett[126] pointed out, there is reason to trust them qualitatively. After accounting for the Cooper instability, the fermionic ground state does not change dramatically as one changes the coupling strength. So the phase diagram throughout the entire range of coupling strengths should consist of a low temperature superfluid phase and a high temperature normal phase, as depicted in Fig. 1.2

On the far left side of Fig. 1.2, as $1/k_F a \to -\infty$ (hereafter "the BCS side"), T_c obeys the BCS prediction of Eqs. (1.33) and (1.34). If we (rashly) continue the BCS prediction of T_c to the right of Fig. 1.2, then T_c increases to infinity. But the temperature at which bosonic the Cooper pairs can condense (as in Eq. (1.6)) will be lower, tending to the ideal Bose gas $T_c^{(\mathrm{BEC})}$ as $1/k_F a \to \infty$ (hereafter "the BEC side"). As we decrease $1/k_F a$ from the BEC side, the interactions increase T_c linearly in $k_F a$[16]

$$T_c^{(BEC)} = T_c^{(BEC)}\big|_{1/k_F a=\infty}\left(1 + \frac{c}{(3\pi^2)^{1/3}} k_F a + \dots\right), \tag{1.44}$$

where $c \approx 1.32$[8, 110]. These T_c curves for weakly interacting Fermi and Bose gases are plotted in Fig. 1.2. The fading out of the T_c curves, along with the question marks and the shaded vertical span indicate the strongly interacting regime, where the assumptions behind Eqs. (1.6), (1.33), (1.34) and (1.44) precise behavior of T_c is unknown.

The illustrations under the T_c line in Fig. 1.2 highlight the difference between the two regimes. On the BCS side, below T_c, the Cooper pair size is much larger than the interparticle spacing. Overlapping pairs give rise to long range order and the ground state is a superfluid of loosely bound Cooper pairs. Conversely, on the BEC side, the pairs form a two-body bound state where the size of these dimers is much smaller than the interparticle spacing. Below $T_c^{(\mathrm{BEC})}$ the dimers will Bose-Einstein condense, forming a superfluid where the pairing gap is the binding energy of the dimers, $\Delta = E_b = \hbar^2/ma^2$. There is no phase transition between the two regimes. The size of the pairs simply evolves continuously from the BCS to the BEC side. To quote an excellent review[167]: "There is now a clear recognition that the BCS and BEC paradigms are not as distinct as they were once thought to be, but rather are

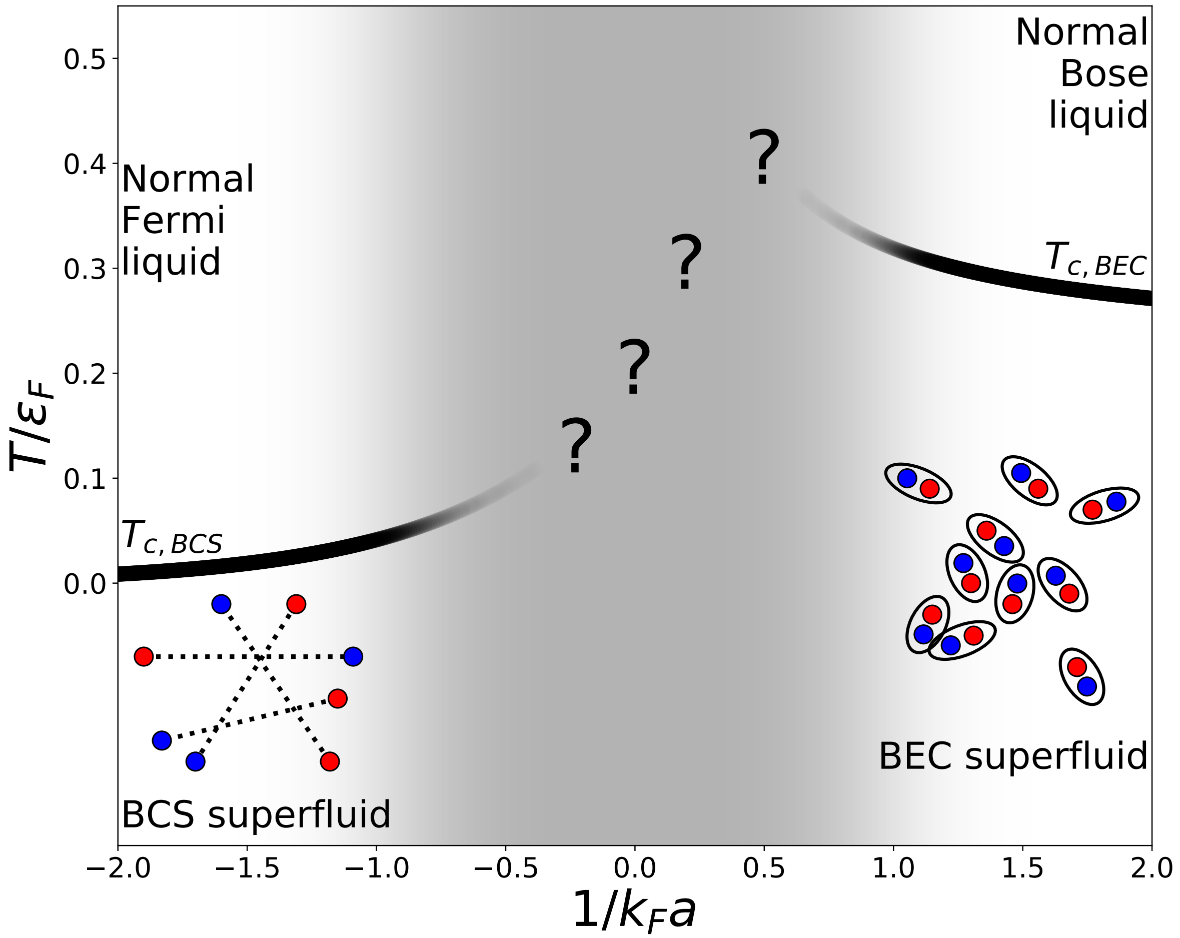

Figure 1.2: Artist's conception of the phase diagram in the BCS–BEC crossover. The T_c line separates the normal state from the superfluid state and is calculated assuming weak interactions (see text). The shaded area represents the strong coupling regime where these assumptions break down.

the two extrema of a continuum."

1.2.4 Unitarity

The point in the phase diagram at $1/k_F a = 0$ is interesting. It corresponds to the formation of a two-body bound state. Formally, it is the dilute limit in which the range of the interactions tends to zero while the scattering length tends to infinity:

$$nr_0^3 \ll 1 \ll n|a|^3, \tag{1.45}$$

where $n = N/V$ is the density, a is the s-wave scattering length as before, and r_0 is the range of the interaction. On paper, one can consider a finite square well interaction with depth V and range r_0, where we take $r_0 \to 0$ while tuning V such that there is a bound state with zero energy[2].

In this limit, because the scattering length is so large compared to the interparticle distance, the only relevant length scale is the Fermi wavelength and the only relevant energy scale is the Fermi energy, which depend only on the density (or interparticle distance, if you like). Quantities such as μ or Δ are therefore some universal fraction of ε_F. The energy is usually measured in units of E_{FFG} as given in Eq. (1.10). Length scales are given in units of the inverse Fermi momentum, which we have been hinting at all along by parameterizing the scattering length using $1/k_F a$. These fractions are universal in the sense that they do not depend on the microscopic features of the potential. Specifically, the total energy of the unitary gas is

$$E(\widetilde{T}) = \xi(\widetilde{T})E_{FFG}, \tag{1.46}$$

where $\widetilde{T} = T/\varepsilon_F$ is the so-called reduced temperature and $\xi(\widetilde{T})$ is a universal dimensionless function that depends on the reduced temperature. The parameter $\xi(0)$ is known as the Bertsch parameter and determining its value has been a major research challenge. The field's current best estimates range between $\xi(0) \approx 0.37$–0.40. See [67] for a review of historical estimates for $\xi(0)$.

The unitary regime was first considered as a model for dilute neutron matter and proposed formally as a challenge by G. F. Bertsch[20, 11] during the 10th Conference on Advances in Many-Body Theory, in Seattle in 1999. Since neutron matter has densities much smaller than the nuclear saturation density of 10^{14}g/cm^3, an effective range of ~ 3 fm and a scattering

---

[2] Further details are provided in Appendix A.1.1

length of about -18 fm [85], it lies just on the BCS side of the unitary regime as defined in Eq. (1.45).

Experimentally, the unitary Fermi gas has been realized in systems of trapped, neutral, cold atoms tuned to through Feshbach resonance[71] with an external magnetic field so that the bound-state energy is brought to zero. See Ref. [54] for a review. Perhaps the most rigorous experimental finite-temperature studies of the unitary Fermi gas are from Ku *et al.*[114]

1.3 Pseudogaps

In § 1.2.1, we discussed that the superconducting gap leads to a complete cancellation of the DoS near the Fermi surface. After the discovery of high T_c superconductors, researchers found that in underdoped cuprate superconductors, there was a suppression in the DoS near the Fermi surface even above T_c [202, 6, 124, 123, 193]. Whereas the "true" gap is identified with complete cancellation of the DoS, this pseudogap leads to only partial depletion of the DoS. The pseudogap is a phenomenological concept and awaits a formal definition, but most often, the pseudogap is defined by this partial suppression of the DoS near the Fermi surface.

To introduce the pseudogap in the context of the BCS–BEC crossover, let us consider the excitation gap in the BEC limit, where Δ is the energy required to break up pairs as discussed in § 1.2.3 and is much larger than the energy associated with $T_c^{(\mathrm{BEC})}$ given in Eq. (1.6). The single particle dispersion is given by

$$E_{\mathbf{k}} = \sqrt{(\epsilon_{\mathbf{k}} - \mu)^2 + |\Delta|^2} \tag{1.47}$$

and we see that when $\mu < 0$, the spectral gap $\sqrt{|\mu|^2 + |\Delta|^2}$ remains finite even for $T > T_c$ where Δ vanishes. This finite spectral gap above T_c is the "pseudogap" in the BEC context. In the BCS limit, there is no such pseudogap. We will use T^* to refer to the temperature at which pairs form and continue to use T_c to refer to the critical temperature at which these pairs condense. In the BCS regime, we have $T_c = T^*$, whereas in the BEC regime, we have $T^* \gg T_c$.

Noting the similarity between Eq. (1.47) and Eq. (1.23c), we should differentiate between the excitation gap Δ in Eq. (1.47) and the superconducting order parameter defined in Eq. (1.15). Hereafter, we will use Δ_{sc} to refer to the superconducting order parameter. While Δ_{sc} goes to zero at T_c, Δ goes to zero at T^*. So it is possible to have $\Delta \neq 0$ while $\Delta_{sc} = 0$, which is simply a restatement of the pseudogap regime using Δ's instead of T's[3]. This behavior is illustrated in Fig. 1.3, adapted from Chen *et al.*[50]. In the BCS regime, the lack of pseudogap is equivalent to the following statements: $T^* = T_c$, $\Delta = \Delta_{sc}$, there are no uncondensed pairs, and the area of the orange shaded region is zero. In the BEC regime, Δ is essentially temperature independent, with the orange region extending very far to the right since $T^* \gg T_c$ is off the scale of the temperature axis. As we vary the scattering length

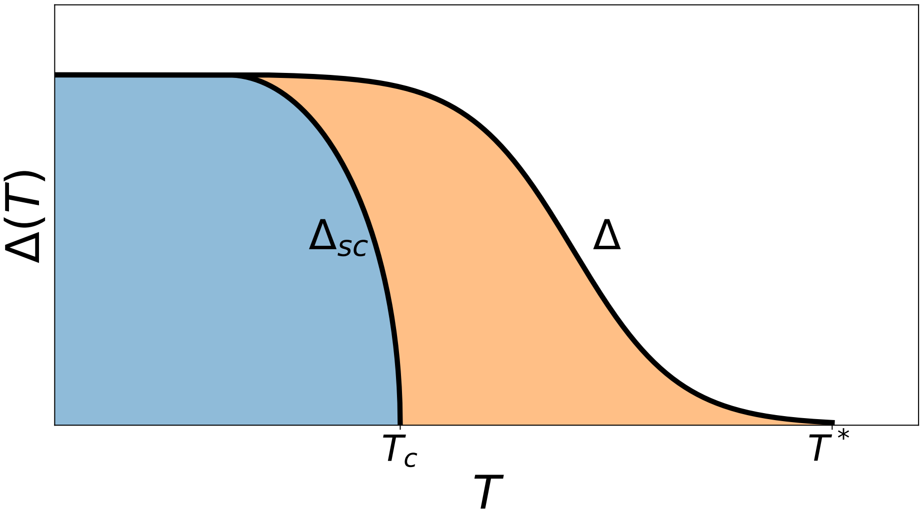

Figure 1.3: Artist's interpretation of the excitation gap versus the superconducting gap in the pseudogap regime of the BCS–BEC crossover. The blue region represents the density of condensed pairs while the orange region represents the density of uncondensed pairs. Adapted from Chen *et al.*[50].

---

[3] It is even possible to have $\Delta_{sc} \neq 0$ with $\Delta = 0$ in superconductors with magnetic impurities[3, 212], but this is beyond the scope of this thesis.

from the BCS side to the BEC side, the excitation gap Δ must evolve smoothly between these two limiting cases.

A natural question to ask is how far can we go toward the BCS regime and still find a pseudogap. At some point, even before the unitary regime, the chemical potential becomes positive, $\mu > 0$, so the naive analysis from the BEC limit suggests that the pseudogap should disappear. Surprisingly, early calculations of the spectral function of the unitary Fermi gas revealed a gap in the single-particle dispersion even above the critical temperature $T > T_c$[137]. However, given the difficulty to calculating or measuring Fermi gases near unitarity, different studies have given different answers to the question of whether the pseudogap survives at unitarity[53, 127, 100, 101, 102, 184, 50, 51, 144]. We address this problem in Chapter 3.

Chapter 2

QUANTUM MONTE CARLO

Throughout Chapter 1 we emphasized the non-perturbative nature of Fermi gases near unitarity and the resultant difficulty in theoretical calculations of BCS-BEC crossover. In this chapter, we will introduce the quantum Monte Carlo techniques required to accurately simulate Fermi gases near unitarity. The literature on quantum Monte Carlo methods is vast and variegated and it is beyond the scope of this thesis to review all of it. The interested reader should consult the relevant textbooks and review articles[150, 149, 115]. Instead, this chapter is limited to introducing the Monte Carlo integration; importance sampling; the auxiliary-field quantum Monte Carlo (AFQMC) method, which is the workhorse algorithm for most of the calculations in this thesis; and the projection and reweighting methods required to estimate some observables.

2.1 Monte Carlo methods

Broadly speaking, Monte Carlo methods are any computational algorithm that rely on random sampling to estimate solutions to deterministic problems. Arguably the first example of a Monte Carlo method is the experiment imagined by the Comte de Buffon[56], in which one estimates the value of π by dropping needles across parallel strips of wood. The first modern version of a Monte Carlo method was developed by Stanislaw Ulam to study neutron diffusion[140] through various materials. Since their invention, Monte Carlo methods have been applied to solve optimization and inverse problems. This section focuses on the most common application of Monte Carlo methods: integration.

Consider a one-dimensional integral

$$I = \int_a^b f(x)\, dx. \tag{2.1}$$

This integral can be approximated using numerical quadrature

$$I \approx I_S = \frac{b-a}{N} \frac{\sum_{i=1}^{N} w_i f(x_i)}{\sum_{i=1}^{N} w_i}. \tag{2.2}$$

The choice of the points, x_i, the weights, w_i, distinguish the various quadrature methods, such as Simpson's rule or Gaussian quadrature[91]. These techniques work well for low-dimensional integrals, but the computational cost required to estimate the integral of dimension d to some fixed accuracy grows exponentially as N^d, leading to the so-called "curse of dimensionality."

Rather than selecting the points x_i according to some quadrature scheme, one could randomly select points over the domain of integration $[a, b]$. The Monte Carlo estimate of the integral is

$$I \approx I_{MC} = (b-a) \langle f \rangle = \frac{b-a}{N} \sum_{i=1}^{N} f(x_i), \tag{2.3}$$

where $\langle f \rangle$ is the average of the value of $f(x_i)$ over the sampled points, x_i. By the central limit theorem, the set of averages over all possible choices for $\{x_i\}$ will have a Gaussian distribution. Given the sample variance of the function evaluations,

$$\mathrm{Var}\left[f\right] = \frac{1}{N-1} \sum_{i=1}^{N} \left(f(x_i) - \langle f \rangle\right)^2, \tag{2.4}$$

one can calculate the variance of the estimate of the integral I_{MC},

$$\mathrm{Var}\left[I_{MC}\right] = \frac{(b-a)^2}{N} \sigma_f^2. \tag{2.5}$$

Thus, the standard deviation of the Monte Carlo estimate of the integral decreases asymptotically to zero as $1/\sqrt{N}$ and is *independent* of the dimensionality of the integral.

However, in this case, and in all of the more advanced techniques described below, if the function of interest $f(x)$ suffers from large variations over the domain of integration, then these sampling methods will converge very slowly. This is related to the infamous "sign problem," where highly varying positive and negative values tend to cancel each other out in the discrete sum in Eq. (2.3). This problem pervades many areas of physics to which we would like to apply Monte Carlo techniques, including Fermi gases and nuclear interactions [196, 198, 111].

2.1.1 Importance Sampling

The Monte Carlo integration method described by Eq. (2.3) contains no prescription for how the points x_i are generated. The naive approach to this is to sample from a uniform distribution of points in the range $[a, b]$. However, not all points will contribute equally to the value of the integral I so uniform random sampling may be inefficient for interesting integrals. It is preferable to sample more frequently in the regions which contribute most to the integral. This type of sampling is known as "importance sampling."

Let $p(x)$ be the anticipated importance of $f(x)$ at point x to the integral. For the moment, ignore the question of how one comes up with $p(x)$ and suppose it is provided by an oracle. Once one knows $p(x)$, then one can select the points $\{x_i\}$ with probability $p(x)$ and then weight the contribution of each function evaluation by the inverse of that probability. The estimate of the integral is then

$$I = \int_a^b \frac{f(x)}{p(x)} p(x)\, dx \approx \frac{1}{N} \sum_{i=1}^{N} \frac{f(x_i)}{p(x_i)}. \tag{2.6}$$

Comparing the right-hand-side of Eq. (2.6) with Eq. (2.3), one can view importance sampling as a uniform sampling of some new function $g(x) \equiv \frac{f(x)}{p(x)}$. Choosing $p(x)$ such that it approximates $f(x)$, then $g(x)$ will be close to one over the entire domain of integration, $\text{Var}[g]$ will be small, and the error in our estimate of the integral given by Eq. (2.5) will be improved.

2.1.2 The Metropolis Algorithm

The Monte Carlo estimate in Eq. (2.6) motivated the need for sequences of points that are not drawn from the uniform distribution, but rather from some distribution that approximates the integrand. The Metropolis-Hastings (MH) algorithm[141, 93] generates a random walk of points approximately drawn from this probability distribution. Starting from some initial position or "state", one proposes a "move" in a random direction. This move is either accepted or rejected depending on the energy difference between the current and proposed states. Because the samples drawn depend on the previous state, the sequences of samples are called "chains" or, more specifically, Markov chains, named after the broader class of sampling methods to which the MH algorithm belongs: Markov chain Monte Carlo (MCMC) methods.

Formally, the MH algorithm constructs a set of states according to a probability distribution $\pi(x)$ that is designed to approximate $p(x)$. Let the conditional probability of transitioning from the current state, x, to the proposed state, x', be $P(x' \mid x)$. The MH algorithm is uniquely defined by these conditional probabilities, $P(x' \mid x)$, and will reach a unique stationary distribution $\pi(x)$ so long as the following two conditions are met[115]:

1. The stationary distribution, $\pi(x)$ exists. One way to guarantee that the stationary distribution exists is to require that the transition probabilities $P(x' \mid x)$ satisfy the "detailed balance" condition. That is, the probability of being in state x and moving to state x' must be the same as the probability of being in x' and moving to state x:

$$\pi(x)P(x' \mid x) = \pi(x')P(x \mid x')\,. \tag{2.7}$$

2. The stationary distribution, $\pi(x)$ is unique. One way to guarantee uniqueness is to require the transitions to be ergodic, meaning that all the possible configurations of the system should be reachable from any starting position in a finite number of moves.

The goal of the MH algorithm is to have the stationary distribution $\pi(x)$ reach the desired probability distribution $p(x)$ that approximates the importance of $f(x)$. One can derive the transition probabilities by setting $\pi(x) = p(x)$ so that the detailed balance condition can be written as

$$\frac{P(x' \mid x)}{P(x \mid x')} = \frac{p(x')}{p(x)}. \tag{2.8}$$

The transition probability $P\left(x' \mid x\right)$ can be further decomposed into a proposal probability, $\nu\left(x' \mid x\right)$, and an acceptance probability, $A\left(x' \mid x\right)$,

$$P\left(x' \mid x\right) = \nu\left(x' \mid x\right) A\left(x' \mid x\right). \tag{2.9}$$

The detailed balance condition is then

$$\frac{A\left(x' \mid x\right)}{A\left(x \mid x'\right)} = \frac{p(x')}{p(x)} \frac{\nu\left(x \mid x'\right)}{\nu\left(x' \mid x\right)}. \tag{2.10}$$

In this thesis, as in many other MH-based methods, we assume that the proposal probabilities are equal, $\frac{\nu(x \mid x')}{\nu(x' \mid x)} = 1$ so that a good choice for the acceptance probability of a proposed move from x to x' is

$$A\left(x' \mid x\right) = \min\left(1, \frac{p(x')}{p(x)}\right). \tag{2.11}$$

To summarize, the MH algorithm is given by

1. Start from an initial state $x_i = x_0$.
2. Generate a candidate state x'.
3. Calculate the acceptance probability in Eq. (2.11).
4. Generate a uniform random number $r \in [0, 1]$.
5. If $r \leq A(x', x_i)$, accept the candidate state, $x_{i+1} = x'$.
6. If $r > A(x', x_i)$, reject the candidate state and set $x_{i+1} = x_i$.
7. Repeat from Item 2 until desired convergence is attained.

2.2 Quantum Monte Carlo methods

Quantum Monte Carlo (QMC) methods encompass all approaches that use classical Monte Carlo methods to estimate multi-dimensional integrals that arise while solving many-body quantum mechanics problems.

2.2.1 Projector-based QMC

When our interest is restricted to the ground-state properties of a system at zero-temperature, projector-based QMC methods are the dominant method. Here, one starts with a trial wavefunction, ψ_T, and projects out the ground state by imaginary time evolution,

$$\psi_0 = \lim_{t\to\infty} \exp\left(-Ht\right)\psi_T. \tag{2.12}$$

In practice, the approximation

$$\psi_0 \approx \exp\left(-Ht\right)\psi_T, \tag{2.13}$$

is valid so long as the projection time, t, is sufficiently long and the trial wavefunction, ψ_T has some overlap with the true ground state, $\langle\psi_0|\psi_T\rangle \neq 0$. The numerical implementation of the projection operator, $\exp\{-Ht\}$ is what distinguishes one projector-based QMC method from another. We will return to one such method after briefly discussing another QMC context, the grand canonical ensemble, and we will see that both contexts are amenable to study using the same method.

2.2.2 Finite-temperature QMC

When our interest is on thermal properties, one typically chooses to simulate systems in the grand canonical ensemble (GCE), where the thermodynamic variables are the temperature T, the chemical potential μ, and the volume V. The GCE assigns a probability $p = \exp\{-\beta(E-\mu N)\}$ to each microstate, where $\beta = 1/T$ is the inverse temperature, N is the particle number, and E is the total energy of the system (in units where Boltzmann's constant $k_B = 1$).

The partition function, Z, which measures the degree to which the particles are spread out over the system's energy levels at a certain temperature, is given by a trace over Fock space of the aforesaid probabilities,

$$Z(\beta,\mu,V) = \mathrm{Tr}\left\{\exp\left[-\beta\left(\hat{H}-\mu\hat{N}\right)\right]\right\}, \tag{2.14}$$

while the expectation value of some observable, $\mathcal{O}$, is

$$\langle \mathcal{O}(\beta, \mu, V) \rangle = \frac{1}{Z(\beta, \mu, V)} \operatorname{Tr} \left\{ \hat{\mathcal{O}} \exp \left[-\beta \left(\hat{H} - \mu \hat{N} \right) \right] \right\}. \tag{2.15}$$

Note the similarity between the statistical weight $\exp\left[-\beta\left(\hat{H} - \mu\hat{N}\right)\right]$ in Eq. (2.15) and the projection operator $\exp[-Ht]$ in Eq. (2.13). In the projector-based QMC methods, the projection time, t, plays the same role as the inverse temperature, β, in the grand canonical ensemble. In the following sections, we will use the context of the grand canonical ensemble to explain QMC methods, but they will apply equally as well to the zero-temperature projector-based QMC methods by making the notational substitutions $\beta \leftrightarrow t$ and $\exp\left[-\beta\left(\hat{H} - \mu\hat{N}\right)\right] \leftrightarrow \exp\left[-\hat{H}t\right]$. Likewise, discussion of the statistical weight in the GCE context will also apply to the projection operator in the zero-temperature context.

2.2.3 Discretization of the statistical weight

Numerical calculation of the statistical weight begins first by discretizing the inverse temperature using a Trotter expansion, [195]

$$\exp\left[-\beta\left(\hat{H} - \mu\hat{N}\right)\right] = \prod_{j=1}^{N_\tau} \exp\left[-\tau\left(\hat{H} - \mu\hat{N}\right)\right], \tag{2.16}$$

where $\beta = N_\tau \tau$. We further decompose the exponentials into exponentials that depend separately on the kinetic and potential energy operators. Writing $\hat{H} = \hat{K} + \hat{V}$, one applies the Suzuki decomposition,[186]

$$\exp\left[-\tau\left(\hat{H} - \mu\hat{N}\right)\right] = \exp\left[-\frac{1}{2}\tau\left(\hat{K} - \mu\hat{N}\right)\right] \exp\left[-\tau\hat{V}\right] \exp\left[-\frac{1}{2}\tau\left(\hat{K} - \mu\hat{N}\right)\right] + \mathcal{O}(\tau^3). \tag{2.17}$$

These two decompositions are so often chained together that the combined approach is often called the Suzuki-Trotter decomposition,

$$\begin{aligned}\exp\left[-\beta\left(\hat{H}-\mu\hat{N}\right)\right] = &\exp\left[-\frac{1}{2}\tau\left(\hat{K}-\mu\hat{N}\right)\right] \\ &\times\left(\prod_{j=1}^{N_\tau}\exp\left[-\tau\hat{V}\right]\exp\left[-\tau\left(\hat{K}-\mu\hat{N}\right)\right]\right) \\ &\times\exp\left[+\frac{1}{2}\tau\left(\hat{K}-\mu\hat{N}\right)\right]+\mathcal{O}(\tau^2). \end{aligned} \tag{2.18}$$

2.2.4 The Hubbard-Stratonovich Transformation

The kinetic energy operators in Eq. (2.18) are one-body operators, diagonal in momentum space, and are therefore easy to evaluate numerically. On the other hand, the interaction factor $\exp\left[-\tau\hat{V}\right]$ is a many-body term. For example, for a two-body spin-independent interaction that depends only on the interparticle spatial separation, we have

$$\hat{V} = \sum_{\substack{r,r' \\ \lambda,\lambda'}} V\left(r-r'\right)\hat{a}^\dagger_\lambda(r)\hat{a}^\dagger_{\lambda'}(r')\hat{a}_{\lambda'}(r')\hat{a}_\lambda(r) \tag{2.19}$$

$$= \sum_{\substack{r,r' \\ \lambda,\lambda'}} V\left(r-r'\right)\hat{n}_\lambda(r)\hat{n}_{\lambda'}(r') - V(0)\sum_{r,\lambda}\hat{n}_\lambda(r), \tag{2.20}$$

where $\hat{a}^\dagger_\lambda(r)$ and $\hat{a}_\lambda(r)$ are creation and annihilation operators for fermions with spin quantum number λ and position r, $V(r-r')$ is the scalar potential as a function of the interparticle spatial separation, $\hat{n}_\lambda(r) = \hat{a}^\dagger_\lambda(r)\hat{a}_\lambda(r)$ is the number operator, and we have used the fermionic commutation relation $\left[\hat{a}_\lambda(r), \hat{a}^\dagger_{\lambda'}(r')\right] = \delta_{\lambda,\lambda'}\delta(r-r')$.

The last term in Eq. (2.20) is a scalar proportional to the particle number and can be dropped from the calculation. Its contribution will be cancelled out by the normalization from the partition function in the denominator of Eq. (2.15).

For spin-1/2 fermions, the spin variables are constrained to $\lambda \in [\uparrow, \downarrow]$. Let $\hat{n}(r) \equiv \hat{n}_\uparrow(r) + \hat{n}_\downarrow(r)$ so that

$$\hat{V} = \sum_{r,r'} V(r-r')\hat{n}(r)\hat{n}(r'). \tag{2.21}$$

In momentum space, this interaction operator reads

$$\hat{V} = \sum_{q} V(q)\hat{n}(q)\hat{n}(-q), \tag{2.22}$$

where the number operator in momentum space has time reversal symmetry, $T\left[\hat{n}(q)\right] = n(-q)$.

The Hubbard-Stratonovich (HS) transformation is a family of transformations that linearize the density operator in a many-body interaction term like Eq. (2.22) by introducing an auxiliary field.[183, 103] This reformulates the system of interacting particles as a system of independent particles interacting with a "fictitious" fluctuating field. HS transformations rely on the integral identity

$$\exp\left[\beta A^2\right] = \sqrt{\frac{1}{2\pi}} \int_{-\infty}^{\infty} \mathrm{d}\sigma \exp\left[-\frac{\sigma^2}{2}\right] \exp\left[\sigma\sqrt{2\beta}A\right], \tag{2.23}$$

On the left-hand-side, we have a two body operator A^2 that is difficult to evaluate numerically, whereas the integrand on the right-hand-side contains a one body operator A that can be easily evaluated. Unfortunately, we have acquired the complexity of evaluating an integral over σ, a potentially highly-dimensional, potentially highly oscillatory, auxiliary field.

Continuous HS Transformation

When our interaction term is a spin-independent two-body interaction as in Eq. (2.22), and if we further restrict $V(q) < 0$, then Lang *et al.* [119] showed that one can use an HS transformation of the form

$$\exp\left[-\tau\hat{V}\right] = \int_{-\infty}^{\infty} \mathrm{d}\sigma\, \mathrm{d}\sigma^* \,\frac{\tau|V(q)|}{2\pi} \exp\left[-\tau|V(q)||\sigma|^2\right] \exp\left[-\tau\hat{v}\right], \tag{2.24}$$

where $\hat{V}$ is the potential operator in Eq. (2.22), $V(q)$ is the scalar potential as a function of the two-body momentum transfer q, and $\hat{v} \equiv V(q)\sigma\hat{n}(-q) + V(q)\sigma^*\hat{n}(q)$ is the fluctuating one-body auxiliary potential operator. The auxiliary field σ is now a continuous complex-valued field, hence the integration over both real and imaginary parts.

The HS transformation is exact but in practice we express this integral using Gaussian quadrature,

$$\int_{-\infty}^{\infty} \mathrm{d}x\, e^{-x^2} f(x) \approx \sum_{i=1}^{n} w_i f(x_i), \tag{2.25}$$

where x takes the place of $\sqrt{\tau |V(q)|}\sigma$ in Eq. (2.24). If $n = 5$, this five-point formula has an error of $\mathcal{O}(\tau^5)$, so the error is dominated by the Suzuki-Trotter decomposition of Eq. (2.18).

Discrete HS Transformation

If our interaction term is restricted to a two-body contact interaction of the form

$$\hat{V} = \sum_{r} g \hat{n}_{\uparrow}(r) \hat{n}_{\downarrow}(r), \tag{2.26}$$

where g is a bare coupling constant quantifying the strength of the contact interaction, then we can use an HS transformation that depends on discrete auxiliary fields[96]:

$$\exp\left[g\tau \hat{n}_{\uparrow}(\mathbf{r}) \hat{n}_{\downarrow}(\mathbf{r})\right] = \frac{1}{2} \sum_{\sigma(\mathbf{r},\tau_j)=\pm 1} \left[1 + A\sigma(\mathbf{r},\tau_j)\hat{n}_{\uparrow}(\mathbf{r})\right] \times \left[1 + A\sigma(\mathbf{r},\tau_j)\hat{n}_{\downarrow}(\mathbf{r})\right], \tag{2.27}$$

where $A = \sqrt{\exp(g\tau) - 1}$, and $\sigma(\mathbf{r}, \tau_j)$ is an auxiliary field that can take the value ±1 at each point on the spacetime lattice given by the vectors $\mathbf{r}_i$ and time slices τ_j.

2.3 Auxiliary-Field Quantum Monte Carlo

Auxiliary-field quantum Monte Carlo (AFQMC) methods use Monte Carlo methods to evaluate the integral in Eq. (2.23). The random walks of § 2.1.2 are over a state space of single particle Slater determinants subject to a fluctuating external potential.

Whether we use the continuous HS transformation of Eq. (2.24) or the discrete transformation of Eq. (2.27), the partition function can now be represented as an integral over the auxiliary fields

$$Z = \int \mathcal{D}\sigma\left(\mathbf{r}, \tau_j\right) \mathrm{Tr}\, \hat{\mathcal{U}}[\sigma] \tag{2.28}$$

where $\hat{\mathcal{U}}$ is the decomposed statistical weight in Eq. (2.18). The statistical weight can be expressed as a product of spin-up and spin-down operators

$$\hat{\mathcal{U}}[\sigma] = \hat{\mathcal{U}}_{\uparrow}[\sigma]\hat{\mathcal{U}}_{\downarrow}[\sigma], \quad \text{where} \quad \hat{\mathcal{U}}_{\uparrow}[\sigma] = \hat{\mathcal{U}}_{\downarrow}[\sigma] \quad \text{if} \quad \mu_{\uparrow} = \mu_{\downarrow}. \tag{2.29}$$

The expectation value of an observable is

$$\langle \mathcal{O} \rangle = \frac{\operatorname{Tr} \hat{\mathcal{O}}\hat{\mathcal{U}}}{\operatorname{Tr} \hat{\mathcal{U}}} = \int \mathcal{D}\sigma \frac{\operatorname{Tr} \hat{\mathcal{U}}[\sigma]}{Z} \frac{\operatorname{Tr} \hat{\mathcal{O}}\hat{\mathcal{U}}[\sigma]}{\operatorname{Tr} \hat{\mathcal{U}}[\sigma]}. \tag{2.30}$$

When we use $\mathcal{U}[\sigma]$ to represent $\hat{\mathcal{U}}[\sigma]$ in the single particle Hilbert space using a plane-wave basis, we get

$$\operatorname{Tr} \hat{\mathcal{U}}[\sigma] = \det\left[1 + \mathcal{U}[\sigma]\right] = \det\left[1 + \mathcal{U}_{\uparrow}[\sigma]\right] \det\left[1 + \mathcal{U}_{\downarrow}[\sigma]\right] = \det{}^2\left[1 + \mathcal{U}_{\uparrow}[\sigma]\right], \tag{2.31a}$$

with the last equality holding when $\mu_{\uparrow} = \mu_{\downarrow}$, in which case $\operatorname{Tr} \hat{\mathcal{U}}$ becomes a positive definite probability measure for our AFQMC calculations:

$$P[\sigma] = \frac{\det^2\left[1 + \mathcal{U}_{\uparrow}[\sigma]\right]}{Z} \tag{2.32a}$$

$$= \frac{1}{Z} \exp\left(2 \operatorname{Tr} \log\left[1 + \mathcal{U}_{\uparrow}[\sigma]\right]\right) \tag{2.32b}$$

and

$$\langle \mathcal{O} \rangle = \sum_{\sigma} P[\sigma] \frac{\operatorname{Tr} \hat{\mathcal{O}}\hat{\mathcal{U}}[\sigma]}{\det\left[1 + \mathcal{U}[\sigma]\right].} \tag{2.32c}$$

The one-body density matrix is represented in position space

$$n(\mathbf{r}_1, \mathbf{r}_2, \sigma) = \left[\frac{\mathcal{U}[\sigma]}{1 + \mathcal{U}[\sigma]}\right]_{\mathbf{r}_1, \mathbf{r}_2}, \tag{2.33}$$

with an analogous representation calculated in momentum space by Fourier transform.

As suggested in Eq. (2.32c), because the auxiliary fields σ are discrete (or discretized through Gaussian quadrature in the case of a continuous HS transformation), the integration over auxiliary fields is actually a summation over all $2^{N_x N_y N_z N_\tau}$ possible field configurations, necessitating the use of Monte Carlo integration with the standard Metropolis algorithm[141, 93].

2.3.1 Stabilization

When the number of imaginary time slices N_τ grows large, the matrix product $\mathcal{U}$ becomes numerically unstable. Our AFQMC method is based on a previous approach that used singular value decomposition to stabilize the matrix product $\mathcal{U}$. Departing from this previous calculation, we stabilize $\mathcal{U}$ using QDR decomposition. The differences and advantages of these approaches are described in more detail by Gilbreth and Alhassid [81].

Let the statistical weight be represented by a product of weights in the Trotter decomposition

$$\mathcal{U} = \prod_{j=1}^{N_\tau} \mathcal{W}_j, \tag{2.34}$$

where $\mathcal{W}_j$ is defined by the equivalence between Eq. (2.18) and Eq. (2.34). As we propagate through imaginary time, the running product of $\mathcal{W}_j$ matrices becomes unstable. It is therefore desirable to "pause" this propagation every so often and recondition the running product before resuming the propagation in imaginary time. Suppose we want to perform this stabilization procedure every M imaginary time steps, leading to a total of $N_{QDR} = N_\tau/M$ stabilization steps. Let us define $\mathcal{U}_i$ (with a subscript) be the product of the weights $\mathcal{W}_j$ in each of these N_{QDR} chunks of imaginary time,

$$\mathcal{U}_i = \prod_{j=(i-1)M+1}^{iM} \mathcal{W}_j \tag{2.35}$$

so that

$$\mathcal{U} = \mathcal{U}_{N_{QDR}} \, \mathcal{U}_{N_{QDR}-1} \, \ldots \, \mathcal{U}_3 \, \mathcal{U}_2 \, \mathcal{U}_1 \tag{2.36}$$

To stably compute the entire product $\mathcal{U}$, we decompose each time evolution operator using a QDR decomposition,

$$\begin{aligned}
\mathcal{U}_1 &= \mathcal{Q}_1\mathcal{D}_1\mathcal{R}_1, \\
\mathcal{U}_2\,\mathcal{U}_1 &= (\mathcal{U}_2\mathcal{Q}_1\mathcal{D}_1)\,\mathcal{R}_1 = \mathcal{Q}_2\mathcal{D}_2R_2R_1 \\
\mathcal{U}_3\,\mathcal{U}_2\,\mathcal{U}_1 &= (\mathcal{U}_3\mathcal{Q}_2\mathcal{D}_2)\,\mathcal{R}_2\mathcal{R}_1 = \mathcal{Q}_3\mathcal{D}_3\mathcal{R}_3\mathcal{R}_2\mathcal{R}_1 \\
&\vdots \\
\mathcal{U} &= \left(\mathcal{U}_{N_{QDR}}\mathcal{Q}_{N_{QDR}-1}\mathcal{D}_{N_{QDR}-1}\right)\mathcal{R}_{N_{QDR}-1}\mathcal{R}_{N_{QDR}-2}\ldots\mathcal{R}_3\mathcal{R}_2\mathcal{R}_1 \\
&= \mathcal{Q}_{N_{QDR}}\mathcal{D}_{N_{QDR}}\mathcal{R}_{N_{QDR}}\mathcal{R}_{N_{QDR}-1}\ldots\mathcal{R}_3\mathcal{R}_2\mathcal{R}_1 = \mathcal{Q}\mathcal{D}\mathcal{R} \qquad (2.37)
\end{aligned}$$

where the $\mathcal{Q}$ matrices are unitary, the $\mathcal{D}$ matrices are diagonal, and the $\mathcal{R}$ matrices are upper unit-triangular. In order to maintain the stability of the matrix product, the factors in parentheses must first be computed and then decomposed into the $\mathcal{QDR}$ matrices in preparation for multiplication by the next chunk. We perform one final decomposition in the last line to obtain the final $\mathcal{QDR}$ decomposition (without subscripts).

Calculations of functions of the statistical weight become tractable by performing one more $\mathcal{QDR}$ decomposition:

$$1 + \mathcal{U} = \mathcal{Q}\left[\mathcal{Q}^\dagger\mathcal{R}^{-1} + \mathcal{D}\right]\mathcal{R} = \mathcal{Q}\widetilde{\mathcal{Q}}\widetilde{\mathcal{D}}\widetilde{\mathcal{R}}\mathcal{R}, \qquad (2.38)$$

$$\det\left(1 + \mathcal{U}\right) = \det\left(\mathcal{Q}\widetilde{\mathcal{Q}}\right)\det\left(\widetilde{\mathcal{D}}\right)\det\left(\widetilde{\mathcal{R}}\mathcal{R}\right) = e^{i\vartheta}\det\left(\widetilde{\mathcal{D}}\right) \qquad (2.39)$$

$$n = \frac{\mathcal{U}}{1+\mathcal{U}} = 1 - \frac{1}{1+\mathcal{U}} = 1 - \mathcal{R}^{-1}\widetilde{\mathcal{R}}^{-1}\widetilde{\mathcal{D}}^{-1}\widetilde{\mathcal{Q}}^\dagger\mathcal{Q}^\dagger. \qquad (2.40)$$

In Eq. (2.38), we have performed an additional $\mathcal{QDR}$ decomposition of $[\mathcal{Q}^\dagger\mathcal{R}^{-1} + \mathcal{D}]$, represented by $\widetilde{\mathcal{Q}}\widetilde{\mathcal{D}}\widetilde{\mathcal{R}}$. In Eq. (2.39), we have used the fact that the product $\widetilde{\mathcal{R}}\mathcal{R}$ is also has unit diagonal and therefore has a determinant of one. Similarly, the product $\mathcal{Q}\widetilde{\mathcal{Q}}$ is also unitary, and its determinant is therefore some phase factor $e^{i\vartheta}$. For the symmetric case, when $\mu_\uparrow = \mu_\downarrow$, the phases for $\mathcal{U}_\uparrow$ and $\mathcal{U}_\downarrow$ will cancel each other out, so that the the probability measure can be written

$$P[\sigma] = \exp\left(\sum_i \ln\tilde{d}_i\right), \qquad (2.41)$$

where the summation is over the dimension of the single-particle Hilbert space.

2.3.2 Reweighting

The auxiliary field configurations generated using the methods described in § 2.3 can be computationally expensive to obtain. It is therefore desirable to expand the results of one simulated system to other "nearby" systems. For example, one may wish to apply the results of a simulation performed at inverse temperature β_0 to some other inverse temperature β, eliminating the need to perform an entirely separate simulation. Or one could use the results of a simulation with N_0 particles to estimate the properties of a system with $N = N_0 - 1$ particles. Reweighting is one such method that allows us to probe the properties of "nearby" systems using the configurations of an original simulation.[70]

To explain reweighting, suppose that we have conducted our "original" simulation for some particle number N_0. The expectation value of some operator $\mathcal{O}(\sigma)$, sampled over many different configurations σ and at a new fixed particle number of N' is

$$\begin{aligned}\left\langle \mathcal{O} \right\rangle_{N'} &\equiv \frac{1}{Z_{N'}} \int \mathrm{d}\sigma\, \mathcal{O}(\sigma) p_{N'}(\sigma) && (2.42)\\ &= \frac{Z_{N_0}}{Z_{N'}} \frac{1}{Z_{N_0}} \int \mathrm{d}\sigma\, \mathcal{O}(\sigma) p_{N_0}(\sigma) \frac{p_{N'}(\sigma)}{p_{N_0}(\sigma)} && (2.43)\\ &= \frac{Z_{N_0}}{Z_{N'}} \left\langle \mathcal{O} \frac{p_{N'}}{p_{N_0}} \right\rangle_{N_0}. && (2.44)\end{aligned}$$

The ratio of partition functions is given by

$$\frac{Z_{N_0}}{Z_{N'}} \equiv \frac{\int \mathrm{d}\sigma\, p_{N_0}(\sigma)}{\int \mathrm{d}\sigma\, p_{N'}(\sigma)} = \frac{\int \mathrm{d}\sigma\, p_{N_0}(\sigma)}{\int \mathrm{d}\sigma\, p_{N_0}(\sigma) \frac{p_{N'}(\sigma)}{p_{N_0}(\sigma)}} = \left\langle \frac{p_{N'}}{p_{N_0}} \right\rangle_{N_0}^{-1}. \tag{2.45}$$

So the expectation value of some observable at parameter value $N = N'$ can be obtained in terms of expectation values evaluated at $N = N_0$,

$$\left\langle \mathcal{O} \right\rangle_{N'} = \frac{\left\langle \mathcal{O} \frac{p_{N'}}{p_{N_0}} \right\rangle}{\left\langle \frac{p_{N'}}{p_{N_0}} \right\rangle}. \tag{2.46}$$

This seems to imply that one could obtain the expectation value of an observable at any particle number, N, from only a single simulation at particle number N_0. However, in real simulations, finite statistics limit the particle number difference to a narrower "reweighting range."

Reweighting range

Intuitively, one can view the reweighting method as the approximation of one histogram by sampling over a nearby, shifted histogram. These estimated histograms become increasingly worse approximations as the reweighting distance increases because the limited statistics in the tails of the original distribution contribute more to the bulk of the shifted histogram.

We should therefore restrict our reweighting distance such that it lies within the natural range of fluctuations in the original simulation.

$$|\delta \langle \mathcal{O} \rangle| \equiv \left| \langle \mathcal{O} \rangle_N - \langle \mathcal{O} \rangle_{N_0} \right| \lesssim \left[\mathrm{Var}\left[\mathcal{O}\right]_{N_0} \right]^{1/2} = \left\langle \left(\mathcal{O} - \langle \mathcal{O} \rangle_{N_0} \right)^2 \right\rangle_{N_0}^{1/2}. \tag{2.47}$$

Energy and particle number reweighting range For example, if we calculate the energy, then the difference in energies would be

$$|\delta \langle E \rangle| \equiv \left| \langle E \rangle_N - \langle E \rangle_{N_0} \right| \approx \left| (N - N_0) \left(\frac{\partial \langle E \rangle}{\partial N} \right)_{N=N_0} \right| = |(N - N_0)\mu(N_0)|, \tag{2.48}$$

where μ is the chemical potential, and the limiting deviation of the original distribution would be

$$\left\langle \left(E - \langle E \rangle_{N_0} \right)^2 \right\rangle_{N_0}^{1/2} = \sqrt{\mu(N_0)}, \tag{2.49}$$

by the fluctuation-dissipation theorem. Thus, the particle number reweighting range should be limited to

$$|\delta N| \equiv |N - N_0| \lesssim \mu(N_0)^{-1/2}. \tag{2.50}$$

Scattering length reweighting range When simulating the unitary Fermi gas, we may wish to reuse auxiliary field configurations generated at unitarity (i.e. $(k_F a)^{-1} = 0$) to simulate systems away from unitarity. The reweighting range for the inverse scattering length will be given by

$$|\delta \langle E\rangle| \equiv \left|\langle E\rangle_{1/a} - \langle E\rangle_{1/a=0}\right| \approx \left|\frac{1}{a}\left(\frac{\partial \langle E\rangle}{\partial(1/a)}\right)_{1/a=0}\right|. \tag{2.51}$$

In the limit of large scattering length, the energy of a two-species Fermi gas as a function of the scattering length is given by[34]

$$E(N,a) = \frac{3}{5}N\frac{(\hbar k_F)^2}{2m}\left[\xi - \frac{\zeta}{k_F a} - \frac{5\nu}{3(k_F a)^2} + \mathcal{O}\left(\frac{1}{(k_F a)^3}\right)\right], \tag{2.52}$$

where $\xi = 0.44$, $\zeta \approx 1$, and $\nu \approx 1$. Substituting this into Eq. (2.51) yields

$$|\delta \langle E\rangle| \approx \left|\frac{3}{5}N_0\frac{(\hbar k_{F,0})^2}{2m}\left[\frac{1}{k_F a} + \frac{10}{3(k_F a)^2}\right]\right|, \tag{2.53}$$

where $N_0 = \langle N\rangle_{1/a=0}$ is the average particle number in the unitary limit and $k_{F,0} = (3\pi^2 N_0/V)^{1/3}$ is the Fermi wave number for a system with N_0 particles. So that the scattering length reweighting range must satisfy

$$\left|\frac{1}{k_F a}\left(1 + \frac{10}{3k_F a}\right)\right| \lesssim \frac{10m}{3N_0(\hbar k_{F,0})^2}\left[\mathrm{Var}\left[E\right]_{N_0}\right]^{1/2}. \tag{2.54}$$

Similar reweighting ranges exist for any observable so long as we use the appropriate susceptibility.

2.4 Constrained ensembles

The method described in § 2.3 was described in the context of the grand canonical ensemble (GCE). However, calculations of the observables Δ_E and χ_s require simulation at fixed particle number or fixed particle asymmetry in the canonical ensemble. A similar problem is encountered in nuclear physics when one wants to simulate nuclei with fixed neutron and proton numbers. One approach is to constrain the GCE using particle projection methods [154, 120, 80, 107, 33].

In the following sections, we present the formalism for constraining the GCE, but first we sketch the main idea of particle projection and the novelty of our particle asymmetry projection. Previous studies have constrained the number of spin-up particle, $N_\uparrow$, spin-down

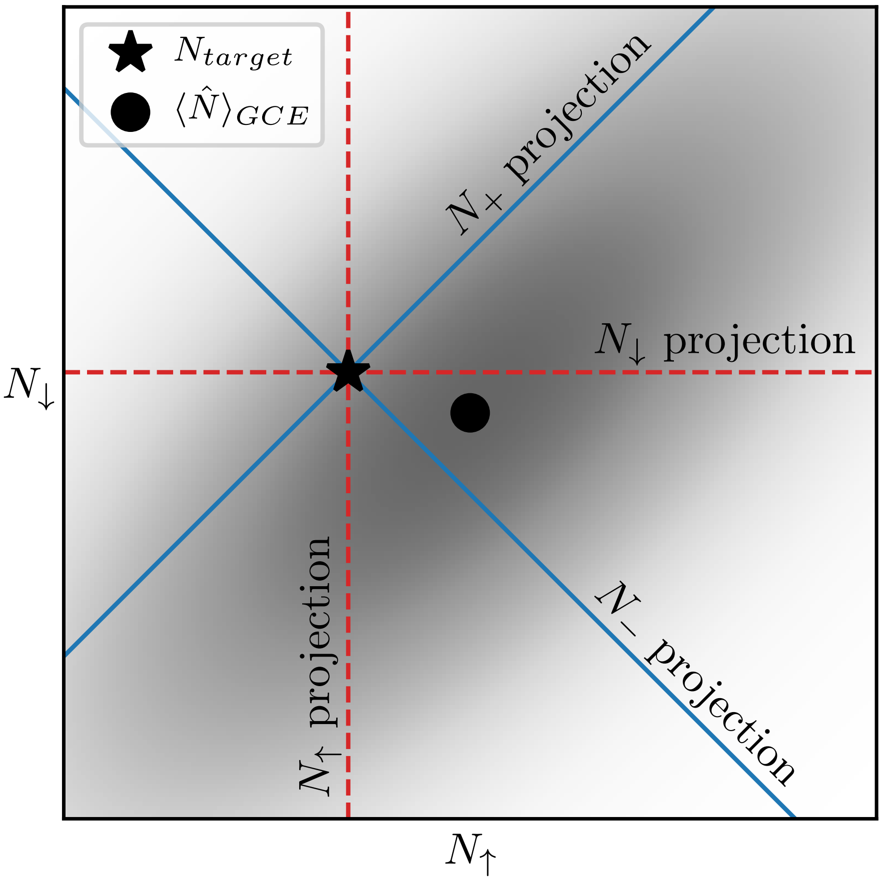

Figure 2.1: Schematic representation of various GCE projection methods. The GCE statistical weight is represented as a shaded blob which is broadly distributed in the N_+ direction and sharply peaked in the N_- direction. Single spin number projection is represented by the red dashed lines parallel to the $N_\uparrow$ and $N_\downarrow$ axes. Total particle number and particle number asymmetry projection are represented by the blue solid lines.

particles, $N_\downarrow$, or the total particle number $N_+ \equiv N_\uparrow + N_\downarrow$, by simultaneous projection of both $N_\uparrow$ and $N_\downarrow$. This is represented schematically in Fig. 2.1, where the shaded blob represents the distribution of some statistical weight in the GCE over particle numbers $N_\uparrow$ and $N_\downarrow$. Constraining the GCE to a single flavor particle number, either $N_\uparrow$ or $N_\downarrow$, can be interpreted as projecting the GCE distribution onto a single slice along either axis. And constraining the GCE to a specific pair $(N_\uparrow, N_\downarrow)$ may be viewed as simultaneous projection along both axes to collapse onto a target point, which may be some distance away from the thermal average in the GCE. If instead, one wishes to constrain the total particle number only, then one projects onto the diagonal line with slope one.

We introduce another constrained ensemble using particle number asymmetry projection, represented in Fig. 2.1 by the diagonal line with negative slope representing a constant value of $N_- \equiv N_\uparrow - N_\downarrow$. If one wishes to constrain the GCE to a specific pair, then one can choose (N_+, N_-) to achieve the equivalent $(N_\uparrow, N_\downarrow)$ pair, rotating the projection axes by $\pi/4$ radians. But this choice of rotation is not arbitrary; it is (a) physically motivated, (b) chosen to minimize variance in one direction, and (c) lacks a sign problem when implemented in AFQMC. Firstly (a), it is appropriate to constrain only the particle number asymmetry to measure some observables, as is the case when measuring spin susceptibility as discussed in § 3.3. Secondly (b), the statistical weights in the GCE are often sharply peaked along the N_- axis, falling off more quickly in the N_- direction than in the N_+ direction. So this specific choice of projection axes minimizes the variance on one of the axes. Lastly (c), as we will show in § 2.4.2, when implemented using AFQMC methods, this asymmetry projection lacks a sign problem. To our knowledge, no other constrained ensemble studies have used the asymmetry projection method.

Lastly, before we formally introduce the projection methods, we should note that in reality, the statistical weights depicted in Fig. 2.1 are not simply concave as shown in the figure. Rather, they have an egg carton shape to account for the impossibility of having even values of N_+ with odd values of N_- and vice versa.

2.4.1 Projecting particle number for single flavor fermions

To constrain the particle number in simulations of single flavor fermions we introduce a slight generalization of the partition function and of the expectation values:

$$\mathcal{Y}(\varphi) = \exp\Big[-\beta\left(\hat{H}-\mu\hat{N}\right) - i\varphi\left(\hat{N}-N\right)\Big], \tag{2.55a}$$

$$\mathcal{Z}(\varphi) = \frac{1}{Z}\operatorname{Tr}\left[\mathcal{Y}(\varphi)\right] = \left\langle \exp\Big[-i\varphi\left(\hat{N}-N\right)\Big]\right\rangle \tag{2.55b}$$

$$\mathcal{E}(\varphi) = \frac{\operatorname{Tr}\left[\hat{H}\mathcal{Y}(\varphi)\right]}{Z} = \left\langle \hat{H}\exp\Big[-i\varphi(\hat{N}-N)\Big]\right\rangle, \tag{2.55c}$$

$$\mathcal{N}(\varphi) = \frac{\operatorname{Tr}\left[\hat{N}\mathcal{Y}(\varphi)\right]}{Z} = \left\langle \hat{N}\exp\Big[-i\varphi(\hat{N}-N)\Big]\right\rangle, \tag{2.55d}$$

where

$$Z = \operatorname{Tr}\exp\Big[-\beta\left(\hat{H}-\mu\hat{N}\right)\Big], \tag{2.55e}$$

as in the GCE and the angle brackets signify the usual GCE expectation value. The additional phase factor $\exp(iN\varphi)$, where N

$$N = \left\langle \hat{N}\right\rangle = \frac{1}{Z}\operatorname{Tr}\left[\hat{N}\exp\Big[-\beta(\hat{H}-\mu\hat{N})\Big]\right], \tag{2.56}$$

cancels the highly oscillatory character of these functions and renders them very smooth. Moreover, as numerical calculations show, the imaginary parts of $\mathcal{Z}(\varphi)$, $\mathcal{E}(\varphi)$, and $\mathcal{N}(\varphi)$ are small[33]. Without the additional phase factor $\exp(iN\varphi)$ these functions are periodic functions of φ, with the period 2π. They also satisfy the relations:

$$\mathcal{Z}(\varphi) = \mathcal{Z}^*(-\varphi), \tag{2.57a}$$

$$\mathcal{E}(\varphi) = \mathcal{E}^*(-\varphi), \tag{2.57b}$$

$$\mathcal{N}(\varphi) = \mathcal{N}^*(-\varphi). \tag{2.57c}$$

Using these relations one can now introduce the projected particle number probability distribution in the grand canonical ensemble and the particle projected expectation values

$$P(\nu) = \int_0^\pi \frac{\mathrm{d}\varphi}{\pi} \mathcal{Z}(\varphi) \exp[i(\nu - N)\varphi], \tag{2.58a}$$

$$E_p(\nu) = \frac{1}{P(\nu)} \int_0^\pi \frac{\mathrm{d}\varphi}{\pi} \exp[i(\nu - N)\varphi] \mathcal{E}(\varphi), \tag{2.58b}$$

$$N_p(\nu) = \frac{1}{P(\nu)} \int_o^\pi \frac{\mathrm{d}\varphi}{\pi} \exp[i(\nu - N)\varphi] \mathcal{N}(\varphi), \tag{2.58c}$$

where ν is an integer argument and

$$P(\nu) = \frac{1}{Z} \operatorname{Tr} \left[\delta_{\nu,\hat{N}} \exp \left[-\beta \left(\hat{H} - \mu \hat{N} \right) \right] \right], \tag{2.59}$$

and where $\delta_{\nu,\hat{N}}$ is a Kronecker δ-operator symbol. $P(\nu)$ satisfies the expected normalization condition

$$\sum_{\nu=0}^{\infty} P(\nu) = 1. \tag{2.60}$$

It is easy to prove that the functions $P(\nu), E_p(\nu), N_p(\nu)$ are real.

With the particle number fixed, the chemical potential μ becomes a stability parameter. One chooses a value of μ that will generate a grand canonical ensemble average particle number close to the range of fixed particle numbers that one wishes to simulate. The accuracy of the evaluated numerical observables can be ascertained by the quality of the relation $N_p(\nu) - \nu \equiv 0$, which appears to satisfied with an accuracy of $\approx 1 \times 10^{-6}$ or better in a particle window of width a fraction of N, for systems with up to $N \approx 10^3$ particles. By changing μ and keeping β constant one can map $E(N, \beta)$ in large particle number N interval.

In the case of interacting particles, after performing an HS transformation one obtains

$$\mathcal{Z}(\varphi) = \operatorname{Tr} \left[e^{-i\varphi(\hat{N} - N)} \int \mathcal{D}\sigma e^{-\tau(\hat{h}(\sigma) - \mu \hat{N})} \right], \tag{2.61a}$$

$$= \int \mathcal{D}\sigma P(\sigma) e^{i\varphi N} \det \left[\frac{1 + e^{-i\varphi} \mathcal{U}}{1 + \mathcal{U}} \right], \tag{2.61b}$$

$$P(\sigma) = \frac{\det[1 + \mathcal{U}]}{Z}, \qquad \int \mathcal{D}\sigma P(\sigma) = 1, \tag{2.61c}$$

where we omit the σ dependence of U for clarity, and otherwise $\mathcal{U}$ is the usual product of imaginary-time evolution operators defined in Eq. (2.36). The "observable" $e^{i\varphi N}$ $\det[(1+e^{-i\varphi}\mathcal{U})/(1+\mathcal{U})]$ has a Gaussian-like behavior as a function of φ. Similar expressions are obtained for other "observables" $\mathcal{E}(\varphi)$ and $\mathcal{N}(\varphi)$. After a QMC trajectory has been accepted we evaluate $P(\nu)$, $E(\nu)$, and $N(\nu)$, and average over the Fourier-transformed "ν-observables" rather than the original "φ-observables."

In a system with two (or more) types of particles at a finite temperature one can make separate particle projections for each type of fermion, by using two (or more) angles, e.g. $\varphi_\uparrow$ and $\varphi_\downarrow$ in the case of two flavors.

2.4.2 Projecting particle number asymmetry in the case of two fermion flavors

In the case of two flavors one can introduce the particle asymmetry constrained ensemble (PACE). Let us consider a spin-1/2 fermion system

$$\hat{N}_+ = \hat{N}_\uparrow + \hat{N}_\downarrow, \tag{2.62a}$$

$$\hat{N}_- = \hat{N}_\uparrow - \hat{N}_\downarrow, \tag{2.62b}$$

$$\hat{N}_\sigma = \sum_k a^\dagger_{k,\sigma} a_{k,\sigma}, \tag{2.62c}$$

where $\sigma = \uparrow, \downarrow$. We now introduce a new type of partition function and the related expectation values

$$\mathcal{W}(\theta) = \exp\Big[-\beta(\hat{H} - \mu\hat{N}) - i\theta(\hat{N}_\uparrow - \hat{N}_\downarrow)\Big], \tag{2.63a}$$

$$W(\theta) = \frac{1}{Z}\,\mathrm{Tr}\,[\mathcal{W}(\theta)] = \Big\langle \exp\Big[-i\theta(\hat{N}_\uparrow - \hat{N}_\downarrow)\Big]\Big\rangle\,, \tag{2.63b}$$

$$E(\theta) = \Big\langle \hat{H}\exp\Big[-i\theta(\hat{N}_\uparrow - \hat{N}_\downarrow)\Big]\Big\rangle\,, \tag{2.63c}$$

$$N_+(\theta) = \Big\langle \hat{N}_+\exp\Big[-i\theta(\hat{N}_\uparrow - \hat{N}_\downarrow)\Big]\Big\rangle\,, \tag{2.63d}$$

$$N_-(\theta) = \Big\langle \hat{N}_-\exp\Big[-i\theta(\hat{N}_\uparrow - \hat{N}_\downarrow)\Big]\Big\rangle\,, \tag{2.63e}$$

The partition function $W(\theta)$ in Eq. (2.63b) is reminiscent of the partition function in studies that use an imaginary chemical potential $ih = i(\mu_\uparrow - \mu_\downarrow)/2$ as an asymmetry parameter[29, 131, 132, 166, 30, 170]. Those studies, however, require analytic continuation to recover a real-valued asymmetry parameter, whereas this method requires no analytic continuation and, as we shall see, is without a sign problem.

The quantities in Eqs. (2.63b) to (2.63e) are functions of θ with period 2π. Using them one can introduce a new type of grand canonical expectation with fixed polarization:

$$P(\eta) = \int_{-\pi}^{\pi} \frac{\mathrm{d}\theta}{2\pi} \exp(i\eta\theta) W(\theta), \tag{2.64a}$$

$$E(\eta) = \frac{1}{P(\eta)} \int_{-\pi}^{\pi} \frac{\mathrm{d}\theta}{2\pi} \exp(i\eta\theta) E(\theta), \tag{2.64b}$$

$$N_\pm(\eta) = \frac{1}{P(\eta)} \int_{-\pi}^{\pi} \frac{\mathrm{d}\theta}{2\pi} \exp(i\eta\theta) N_\pm(\theta). \tag{2.64c}$$

$P(\eta)$, with η an integer argument, is the probability to find an exact spin polarization $\eta = \langle \hat{N}_\uparrow - \hat{N}_\downarrow \rangle$, in the grand canonical ensemble

$$P(\eta) = \frac{1}{Z} \operatorname{Tr}\left[\delta_{\eta, \hat{N}_\uparrow - \hat{N}_\downarrow} \exp\left[-\beta(\hat{H} - \mu \hat{N}) \right] \right]. \tag{2.65}$$

where $\delta_{\eta, \hat{N}_\uparrow - \hat{N}_\downarrow}$ is a Kronecker δ-operator symbol. $P(\eta)$ satisfies the expected normalization condition

$$\sum_{\eta=-\infty}^{\infty} P(\eta) = 1. \tag{2.66}$$

In AFQMC simulations, after an HS transformation, we have

$$W(\theta) = \int \mathcal{D}\sigma P[\sigma] F[\sigma, \theta], \tag{2.67a}$$

$$F[\sigma, \theta] \equiv \left| \det \left[\frac{1 + e^{-i\theta}\mathcal{U}}{1 + \mathcal{U}} \right] \right|^2, \tag{2.67b}$$

$$P[\sigma] \equiv \frac{\det^2[1 + \mathcal{U}]}{Z}, \qquad \int \mathcal{D}\sigma P(\sigma) = 1. \tag{2.67c}$$

Consequently, we have for the expectation values $N_\pm(\theta)$ the following forms

$$N_+(\theta) = \frac{1}{Z} \operatorname{Tr}\left[\hat{N}_+ \mathcal{W}[\theta] \right] = 2 \int \mathcal{D}\sigma P[\sigma] F[\sigma, \theta] \operatorname{Re}\left[\operatorname{Tr} \frac{e^{-i\theta}\mathcal{U}}{1 + e^{-i\theta}\mathcal{U}} \right], \tag{2.68a}$$

$$N_-(\theta) = \frac{1}{Z} \operatorname{Tr}\left[\hat{N}_- \mathcal{W}[\theta] \right] = 2 \int \mathcal{D}\sigma P[\sigma] F[\sigma, \theta] \operatorname{Im}\left[\operatorname{Tr} \frac{e^{-i\theta}\mathcal{U}}{1 + e^{-i\theta}\mathcal{U}} \right], \tag{2.68b}$$

and similar relations for the other quantities $Z(\theta)$, $E(\theta)$, $N_\pm(\theta)$. As with the particle number projection, a good measure of the accuracy of the simulation is to compute the accuracy of the relation $N_-(\eta) - \eta \equiv 0$.

One benefit of constraining only the particle asymmetry as opposed to the total particle number is the positive definiteness of the terms in Eqs. (2.67a) to (2.67c), which avoids the sign problem incurred when projecting total particle number. In Appendix B, we provide further information on thermodynamic relations and fluctuations in the PACE.

2.4.3 Simultaneous projection of total particle number and particle number difference in the case of two fermion flavors

One can combine the projection methods of §§ 2.4.1 and 2.4.2 to project on a specific combination of total particle number and particle difference (equivalent to constraining values for $N_\uparrow$ and $N_\downarrow$). We introduce a new statistical weight, partition function, and related expectation values

$$\mathcal{X}(\varphi,\theta) = \exp\Big[-\beta(\hat{H} - \mu\hat{N}) - i\varphi(\hat{N}_+ - N) - i\theta\hat{N}_-\Big], \tag{2.69a}$$

$$X(\varphi,\theta) = \frac{1}{Z}\,\mathrm{Tr}\left[\mathcal{X}(\varphi,\theta)\right] = \left\langle \exp\Big[-i\varphi(\hat{N}_+ - N) - i\theta\hat{N}_-\Big]\right\rangle, \tag{2.69b}$$

$$E(\varphi,\theta) = \left\langle \hat{H}\exp\Big[-i\varphi(\hat{N}_+ - N) - i\theta\hat{N}_-\Big]\right\rangle, \tag{2.69c}$$

$$N_+(\varphi,\theta) = \left\langle \hat{N}_+\exp\Big[-i\varphi(\hat{N}_+ - N) - i\theta\hat{N}_-\Big]\right\rangle, \tag{2.69d}$$

$$N_-(\varphi,\theta) = \left\langle \hat{N}_-\exp\Big[-i\varphi(\hat{N}_+ - N) - i\theta\hat{N}_-\Big]\right\rangle. \tag{2.69e}$$

As before, we introduced the additional phase factor of $\exp(i\varphi N)$ for numerical stability. Without this phase factor, the "observables" are periodic functions of φ, with a period of 2π and they satisfy similar relations to those in Eq. (2.57c). One then introduces the particle projected expectation values

$$P(\nu,\eta) = \int_{-\pi}^{\pi} \frac{\mathrm{d}\varphi}{2\pi} \int_{-\pi}^{\pi} \frac{\mathrm{d}\theta}{2\pi} e^{i\nu\varphi} e^{i\eta\theta} X(\varphi,\theta), \tag{2.70a}$$

$$E(\nu,\eta) = \frac{1}{P(\nu,\eta)} \int_{-\pi}^{\pi} \frac{\mathrm{d}\varphi}{2\pi} \int_{-\pi}^{\pi} \frac{\mathrm{d}\theta}{2\pi} e^{i\nu\varphi} e^{i\eta\theta} E(\varphi,\theta), \tag{2.70b}$$

$$N_{\pm}(\nu,\eta) = \frac{1}{P(\nu,\eta)} \int_{-\pi}^{\pi} \frac{\mathrm{d}\varphi}{2\pi} \int_{-\pi}^{\pi} \frac{\mathrm{d}\theta}{2\pi} e^{i\nu\varphi} e^{i\eta\theta} N_{\pm}(\varphi,\theta). \tag{2.70c}$$

$P(\nu,\eta)$ is the probability to find states that satisfy both $\langle \hat{N}_+ \rangle - N = \nu$ and $\langle \hat{N}_- \rangle = \eta$ in the grand canonical ensemble and it satisfies the normalization condition

$$\sum_{\nu=-\infty}^{\infty} \sum_{\eta=-\infty}^{\infty} P(\nu,\eta) = 1. \tag{2.71}$$

In our AFQMC simulations, after an HS transformation, we will calculate

$$X(\varphi,\theta) = \int \mathcal{D}\sigma P[\sigma] F[\sigma,\varphi,\theta], \tag{2.72a}$$

$$F[\sigma,\varphi,\theta] \equiv e^{i\varphi N} \frac{1}{\det^2[1+\mathcal{U}]} \det\left[1 + e^{-i(\varphi+\theta)}\mathcal{U}\right] \det\left[1 + e^{-i(\varphi-\theta)}\mathcal{U}\right], \tag{2.72b}$$

$$P[\sigma] \equiv \frac{\det^2[1+\mathcal{U}]}{Z}, \qquad \int \mathcal{D}\sigma P(\sigma) = 1. \tag{2.72c}$$

Appendix D details practical considerations for calculating these observables stably and efficiently.

2.5 Error analysis and the bootstrap

2.5.1 Error propagation for derived observables

One can compute some observables directly from the configurations generated by AFQMC. The expectation values and statistical error estimates of these observables can be computed directly from the AFQMC samples. Let us call these kinds of observables "normal."

Other observables may be represented as a function of "normal" observables. For example, let the derived observable be a function $f(\langle a \rangle, \langle b \rangle)$ of normal observables a and b. To calculate this derived observable, one can directly substitute the expectation values, $\langle a \rangle$ and

$\langle b \rangle$ into the function f. And if the random variables for a and b are statistically independent, then the errors in a and b are added quadratically, so that

$$\mathrm{Var}\left[f\right] = \left[\frac{\partial f}{\partial \langle a \rangle}\right]^2 \mathrm{Var}\left[a\right] + \left[\frac{\partial f}{\partial \langle b \rangle}\right]^2 \mathrm{Var}\left[b\right] \tag{2.73}$$

However, the assumption of statistical independence is often invalid. The "normal" observables a and b are derived from the same auxiliary field configurations. The measurements of a and b are therefore naturally correlated. This is the case with the reweighted observables discussed in § 2.3.2, which depend on the ratio of two "normal" observables. We must therefore rely on other methods to estimate the statistical error of derived observables.

2.5.2 The bootstrap

The bootstrap is one such method of estimating the error of a set of stochastic measurements by constructing many pseudo-independent sets of simulation results [64]. Here we provide a very brief overview of the bootstrap and refer the reader to Ref. [192] for a thorough introduction We follow the notation of Ref. [160], which is specifically aimed at nuclear physicists). Broadly speaking, bootstrapping is any statistical technique that relies on resampling with replacement. Suppose we have a set of n empirical measurements for some observable, $\mathcal{O} = (o_1, o_2, o_3, \ldots, o_n)$. We can create m new distributions $\mathcal{O}^*$, by sampling with replacement from the original empirical distribution,

$$\begin{aligned} \mathcal{O}^*_1 &= (o_1, o_3, o_{24}, \ldots, o_2) \\ \mathcal{O}^*_2 &= (o_{11}, o_5, o_5, \ldots, o_{14}) \\ &\vdots \\ \mathcal{O}^*_m &= (o_4, o_{21}, o_7, o_{16}, \ldots, o_9)\,. \end{aligned} \tag{2.74}$$

We call each of these resampled distributions "bootstrap replicants."

We now wish to relate the empiral distribution $\mathcal{O}$ to the true distribution $\widetilde{\mathcal{O}}$. Bootstrapping is based on the assumption that the empiral distribution is related to the true distribution in the same way that the replicants are related to the original empirical distribution. The mean μ of the true distribution may be estimated using the means of each bootstrap replicant μ_i^*,

$$\mu = \frac{1}{m} \sum_i \mu_i^*, \tag{2.75}$$

and the standard error of the mean can be estimated as

$$\sigma_{\bar{o}} = \frac{\sigma}{\sqrt{m}}, \tag{2.76}$$

where σ is the root-mean-square of the set of bootstrap replicant means $\{\mu_i^*\}$.

Bootstrap resampling assumes that each empirical sample is independent of the others, although extensions of the bootstrap exist for strongly correlated datasets. In our AFQMC method, each successive sample is strongly correlated with the last, but we can obtain independent samples by computing the autocorrelation length for the observations of total energy, which varies depending on the input conditions but is always under 200 Metropolis steps. We therefore downsample all observables by a factor of 200 to achieve independent samples.

Chapter 3

THE PSEUDOGAP IN THE BCS-BEC CROSSOVER

In § 1.3, we introduced the concept of the pseudogap in the context of the BCS–BEC crossover. While it is commonly defined as the suppression in the DoS near the Fermi surface, there are several competing definitions, whose differing signatures have led to debates about their respective existence [144]. In particular, the pseudogap should be identifiable from measurement of the single-particle spectrum, spin-susceptibility, and even-odd energy staggering, among others. Even when researchers agree on the definition and observable signature, there are still subjective judgements regarding the size of the effects. For example, how much suppression of the spin susceptibility, or how much even-odd energy staggering above T_c, is necessary to claim evidence for a pseudogap. As argued by Mueller [144], the main challenge in understanding and even defining the pseudogap is that one is dealing with a strongly correlated system in the normal phase. On one hand, said strong correlations preclude perturbative approaches. On the other hand, the lack of order prevents modeling the low-energy excitations by following the conventional routes of effective field theory around an ordered state. (i.e. mean-field or mean-field-plus-fluctuations approaches). To form a coherent picture of the phenomenology, it is imperative to continue gathering information on the behavior of these kinds of systems, in particular the universal, highly malleable ultracold-atom systems considered here.

In this chapter, we present results measuring pseudogap signatures in the crossover and toward the BEC limit. Namely, using the AFQMC methods of Chapter 2, we will present results for the condensate fraction, critical temperature, spin susceptibility, even-odd energy pairing gap, energy per particle, and Tan contact, for $0.0 \leq 1/(k_F a) \leq 0.3$. Because the pseudogap exists in the BEC limit, one expects to see pseudogap signatures at the highest couplings and then detect either their disappearance or maintenance as one approaches unitarity.

Throughout this chapter, when comparing scattering lengths in a single plot, we use color to consistently encode each scattering length as shown in the upper legend of Fig. 3.3. When comparing different lattice sizes, we will consistently encode each lattice size using marker shapes as shown in the legend of Fig. 3.1. Error bars on individual points represent statistical errors and show the standard error of the mean. Error bands in continuous lines incorporate statistical errors and finite volume effects and represent the standard error of the mean. Figures have been reproduced from Ref. [168]

3.1 Condensate fraction

The condensate fraction can be obtained from the asymptotic behavior of the quantity $h(r)$ [10, 41, 35]:

$$\alpha = \lim_{r\to\infty} h(r), \qquad h(r) = \frac{N}{2}\left(g_2(r) - g_1(r)^2\right), \tag{3.1a}$$

where

$$g_2(r) = \left(\frac{2}{N}\right)^2 \int \mathrm{d}^3\mathbf{r}_1\, \mathrm{d}^3\mathbf{r}_2 \left\langle \psi^\dagger_\uparrow(\mathbf{r}_1+\mathbf{r})\psi^\dagger_\downarrow(\mathbf{r}_2+\mathbf{r})\psi_\downarrow(\mathbf{r}_2)\psi_\uparrow(\mathbf{r}_1)\right\rangle, \tag{3.1b}$$

$$= \left(\frac{2}{N}\right)^2 \int \mathcal{D}\sigma P(\sigma) \int \mathrm{d}^3\mathbf{r}_1\, \mathrm{d}^3\mathbf{r}_2\, n_\uparrow(\mathbf{r}_1+\mathbf{r},\mathbf{r}_1,\sigma) n_\downarrow(\mathbf{r}_2+\mathbf{r},\mathbf{r}_2,\sigma), \tag{3.1c}$$

$$g_1(r) = \frac{2}{N}\int \mathrm{d}^3\mathbf{r}_1 \left\langle \psi^\dagger_\uparrow(\mathbf{r}_1+\mathbf{r})\psi_\uparrow(\mathbf{r}_1)\right\rangle, \tag{3.1d}$$

$$= \frac{2}{N}\int \mathcal{D}\sigma P(\sigma)\int \mathrm{d}^3\mathbf{r}_1\, n_\uparrow(\mathbf{r}_1+\mathbf{r},\mathbf{r}_1,\sigma), \tag{3.1e}$$

which acts as an order parameter, characterizing the extent of off-diagonal long-range order [215]. In Fig. 3.1, we show our results for α at different scattering lengths. An alternative approach is to estimate α as the maximum eigenvalue of g_2 [107]. Comparing our results to those of the eigenvalue method, and to experimental values in the right panel of Fig. 3.1, suggests that the eigenvalue method approaches the experimental α more quickly than our asymptotic value method, most noticeably at higher temperatures.

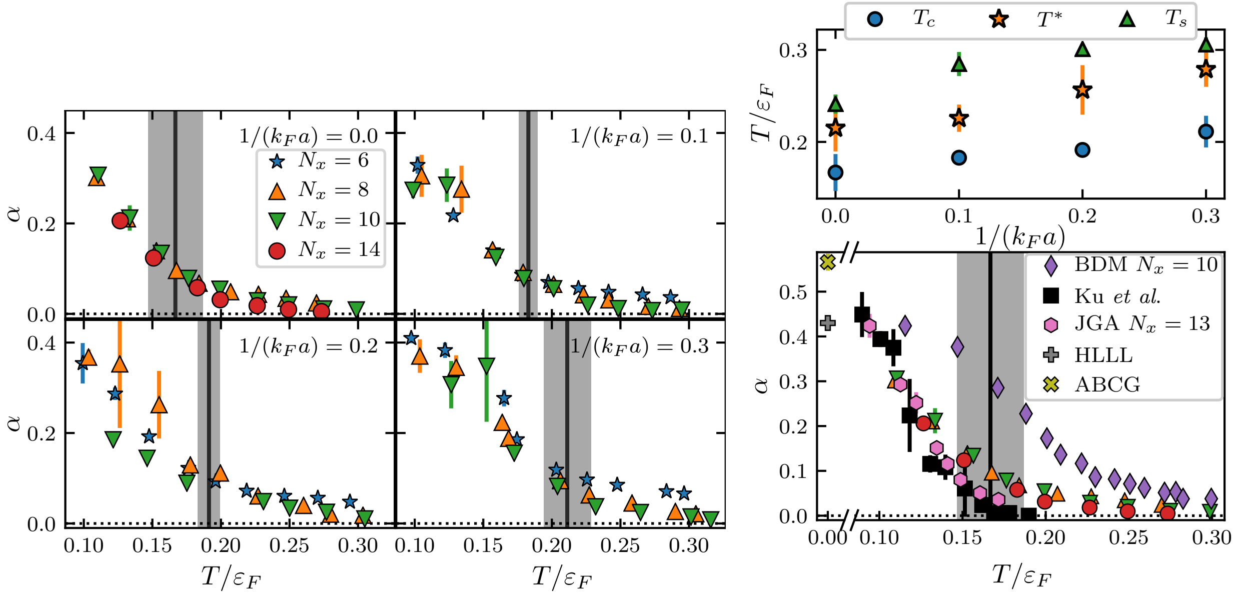

Figure 3.1: Left: The condensate fraction α as a function of temperature at different scattering lengths; at a fixed temperature, α increases toward the BEC limit. At $1/(k_Fa) = 0.2$, Astrakharchik *et al.* [10] estimated the zero-temperature condensate fraction as $\alpha(T = 0) \approx 0.65$. Right (top): characteristic temperatures in the BCS–BEC crossover; T_c is the superfluid critical temperature; T_s is a lower bound on the temperature at which the spin susceptibility peaks; and T^* is the temperature at which the pairing gap disappears. Right (bottom): α at unitarity; our error bars are typically within the marker size. Also shown: the experimental results of Ku *et al.* [114] and the previous AFQMC studies of Bulgac *et al.* [35] (BDM) and Jensen *et al.* [106] (JGA). Also shown are the zero-temperature results by Astrakharchik *et al.* [10] (ABCG) and He *et al.* [94] (HLLL). The JGA estimates, derived from the maximum eigenvalue of the two-body density matrix, are closer to the experimental results especially at high temperature, whereas the finite-size scaling of our results, derived from the asymptotic values of $h(k_Fr)$, yields more accurate estimates of the critical temperature T_c. The discrepancy between our results and BDM, which are also derived from the asymptotic behavior of $h(k_Fr)$, support the argument of Jensen *et al.* [106] that the difference is due to the BDM spherical momentum cutoff.

3.2 Finite size scaling of the condensate fraction

However, we also use the finite-size scaling of α to determine the critical temperature T_c [35, 10, 41]. Near the critical temperature, the condensate fraction α that serves as the order parameter for off-diagonal long range order, has a well-established scaling behavior given by the renormalization group theory [12],

$$R\left(T,L\right) = \alpha(T)L^{1+\eta} = f(x)\left(1 + cL^{-\omega} + \ldots\right), \tag{3.2}$$

where L is the lattice size, $\eta = 0.038$ is a universal critical exponent and $f(x)$ is a universal analytic function of $x \equiv (N_x/\xi_{\text{corr}})^{1/\nu}$, with ξ_{corr} being the correlation length and ν being another universal critical exponent, $\nu = 0.671$. In Eq. (3.2), c is an unknown, non-universal constant, and $\omega \approx 0.8$ is the critical exponent of the leading irrelevant field. The T-dependence in the right-hand-side of Eq. (3.2) is hidden in the correlation length, which diverges near T_c as

$$\xi_{\text{corr}} \propto |1 - T/T_c|^{-\nu}, \tag{3.3}$$

sending x to 0.

For each scattering length, we compute $R(T,L)$ for multiple lattice sizes and multiple temperatures. One then finds "crossing temperatures" T_{ij} at which $R(L_i,T_{ij}) = R(L_j,T_{ij})$. In the left column of Fig. 3.2, we show $R(T,L)$ for each scattering length, indicating the crossing temperatures T_{ij} with multicolored markers.

One then expands the universal function as $f(x) = f(0) + f'(0)L^{1/\nu}b|1 - T/T_c|$, where b is a proportionality constant, yielding

$$|T_c - T_{ij}| = \kappa g\left(L_i, L_j\right) \tag{3.4a}$$

where

$$\kappa = \frac{cT_c f(0)}{bf'(0)} \tag{3.4b}$$

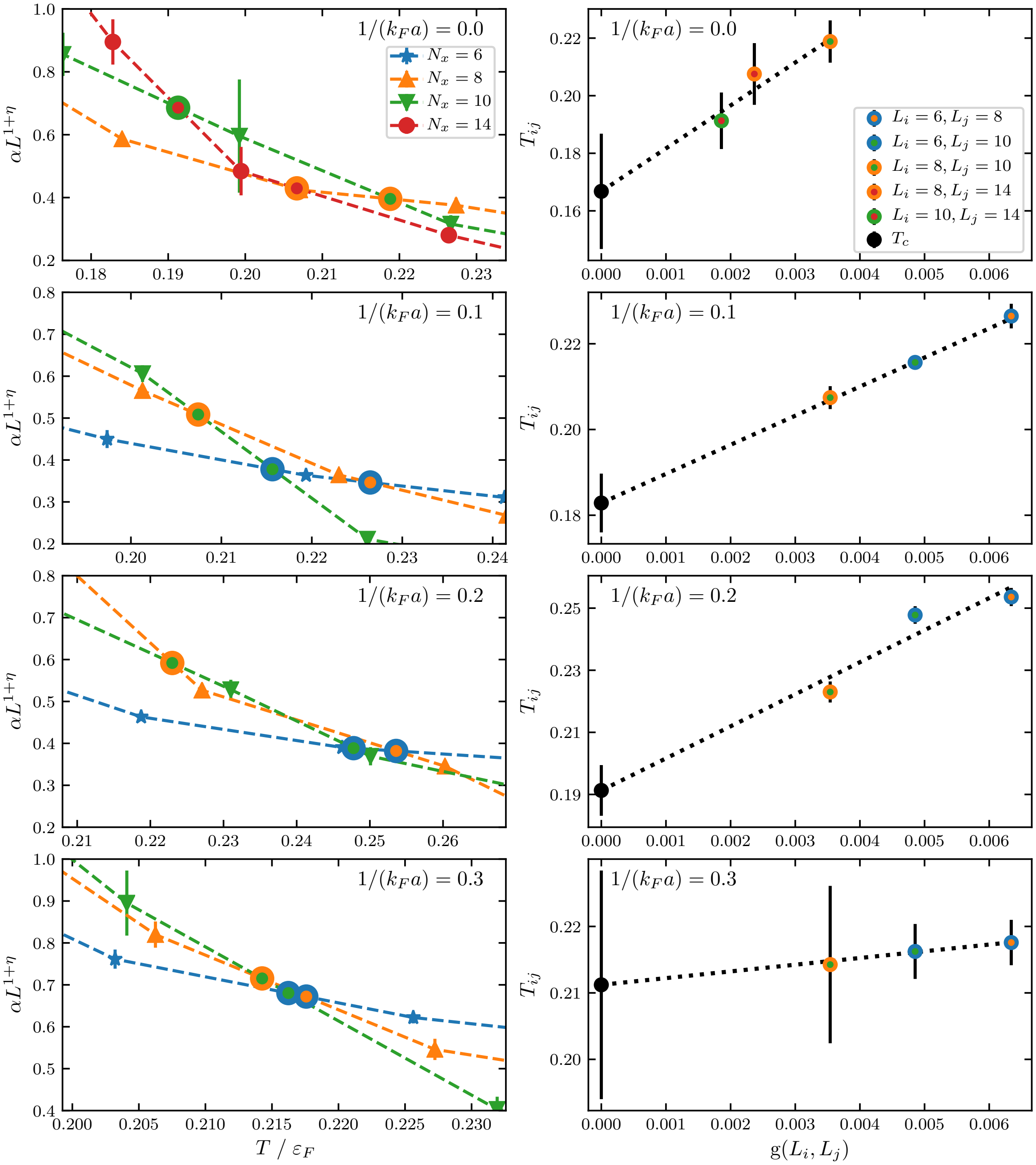

Figure 3.2: (left column) The order parameter $R(T, L)$ from Eq. (3.2) for multiple lattice sizes and scattering lengths. The crossing temperatures are indicated by multicolored markers. (right column) The crossing temperatures T_{ij} from the left are extrapolated to the infinite limit. Black circles at $g(L_i, L_j) = 0$ represent estimates of T_c. Because we used larger lattices at unitarity, the T_{ij} points are closer to the y-axis than other coupling strengths.

and

$$g\left(L_i, L_j\right) = L_j^{-(\omega+1/\nu)} \left[\frac{\left(\frac{L_j}{L_i}\right)^{\omega} - 1}{1 - \left(\frac{L_i}{L_j}\right)^{1/\nu}} \right]. \tag{3.4c}$$

In the thermodynamic limit, $L \to \infty$ and $g(L_i, L_j) \to 0$, one recovers the true critical temperature. One therefore extrapolates the crossing temperatures T_{ij} to the thermodynamic limit, taking care to propagate the errors in α to the crossing temperatures T_{ij} and then to the extrapolated T_c. In the right column of Fig. 3.2, we show the crossing temperatures T_{ij} and extrapolation to the thermodynamic limit. The errors in our estimates of T_c are therefore affected by the errors in α and also by the residuals of the linear fit in Fig. 3.2. This procedure yields critical temperatures as shown in Fig. 3.1, which are consistent with previous studies [41, 35] and in agreement with the experimental result $T_c/\varepsilon_F = 0.167(13)$ at unitarity [114]. The critical temperatures are also listed in Table 3.1 along with other characteristic temperatures described later in this chapter.

$1/(k_F a)$	T_c/ε_F	T^*/ε_F	T_s/ε_F	T_∞/ε_F
0.0	0.16(2)	0.21(3)	$> 0.24(1)$	0.166(5)
0.1	0.183(6)	0.22(2)	$> 0.28(1)$	0.20(1)
0.2	0.191(8)	0.26(3)	> 0.30	0.22(2)
0.3	0.21(2)	0.28(2)	> 0.30	0.23(1)

Table 3.1: Characteristic temperatures in the BCS–BEC crossover. T_c is the superfluid critical temperature. T_s is the temperature at which the spin susceptibility peaks. T^* is the temperature at which the pairing gap disappears. T_∞ is the temperature that separates the low and high temperature behaviors of the Tan contact-derived pairing parameter Δ_∞. T_c estimates are compatible with previous estimates by Burovski *et al.* [41] and Bulgac *et al.* [35]. Estimates for T^* are compatible with previous results by Magierski *et al.* [137].

3.3 Spin susceptibility

Another probe of the normal state character of the pairing is the spin-susceptibility χ_s, which should be suppressed below T^*, as fermions bind into pairs, making the gas strongly diamagnetic [194]. This is also naturally related to the fluctuations in particle asymmetry by

$$\chi_s = \frac{1}{TV}\left\langle \hat{N}_-^2 \right\rangle = \frac{1}{TV}\left\langle \left(\hat{N}_\uparrow - \hat{N}_\downarrow\right)^2 \right\rangle . \tag{3.5}$$

Using the PACE introduced in § 2.4.2, we can calculate the spin susceptibility using only the probability $P(\eta)$ in Eqs. (2.64a) and (2.65),

$$\chi_s = \frac{1}{TV}\frac{\sum_\eta P(\eta)\eta^2}{\sum_\eta P(\eta)} = \frac{1}{TV}\sum_\eta P(\eta)\eta^2, \tag{3.6}$$

where we have used the normalization condition in Eq. (2.66).

In Fig. 3.3, we show our results for χ_s. in units of its zero-temperature, non-interacting counterpart $\chi_0 = 3N/(2V\varepsilon_F)$, and obtained using the PACE, which is completely sign-problem free. These results demonstrate an expected decrease in the maximal value of χ_s as $1/(k_F a)$ increases toward the BEC regime. One also finds a moderate suppression of χ_s above T_c, which increases towards the BEC regime. In the lower panel of Fig. 3.3, we compare our results at unitarity to two previous AFQMC calculations [107, 211], an estimate using strong-coupling Luttinger-Ward theory [68], an experimental result from Sanner *et al.* [175], the prediction from normal Fermi liquid theory (nFLT), and a self-consistent NSR estimate from Pantel *et al.* [158]. The deviation from FLT behavior confirms symmetry based arguments by Rothstein and Shrivastava [172] that 3D unitary Fermi gases cannot be adequately described by nFLT in the range $T_c < T < T_F$. The suppression in χ_s is less severe than in calculations by Wlazłowski *et al.* [211], supporting the argument by Jensen *et al.* [107] that said suppression is affected by the choice of spherical cutoff. However, our results for the spin susceptibility are more suppressed than in both Jensen *et al.* and Enss and Haussmann [68], and, more importantly, the effect seems to grow for larger systems rather than lessen. The comparison with Jensen *et al.*is complicated by their different estimate

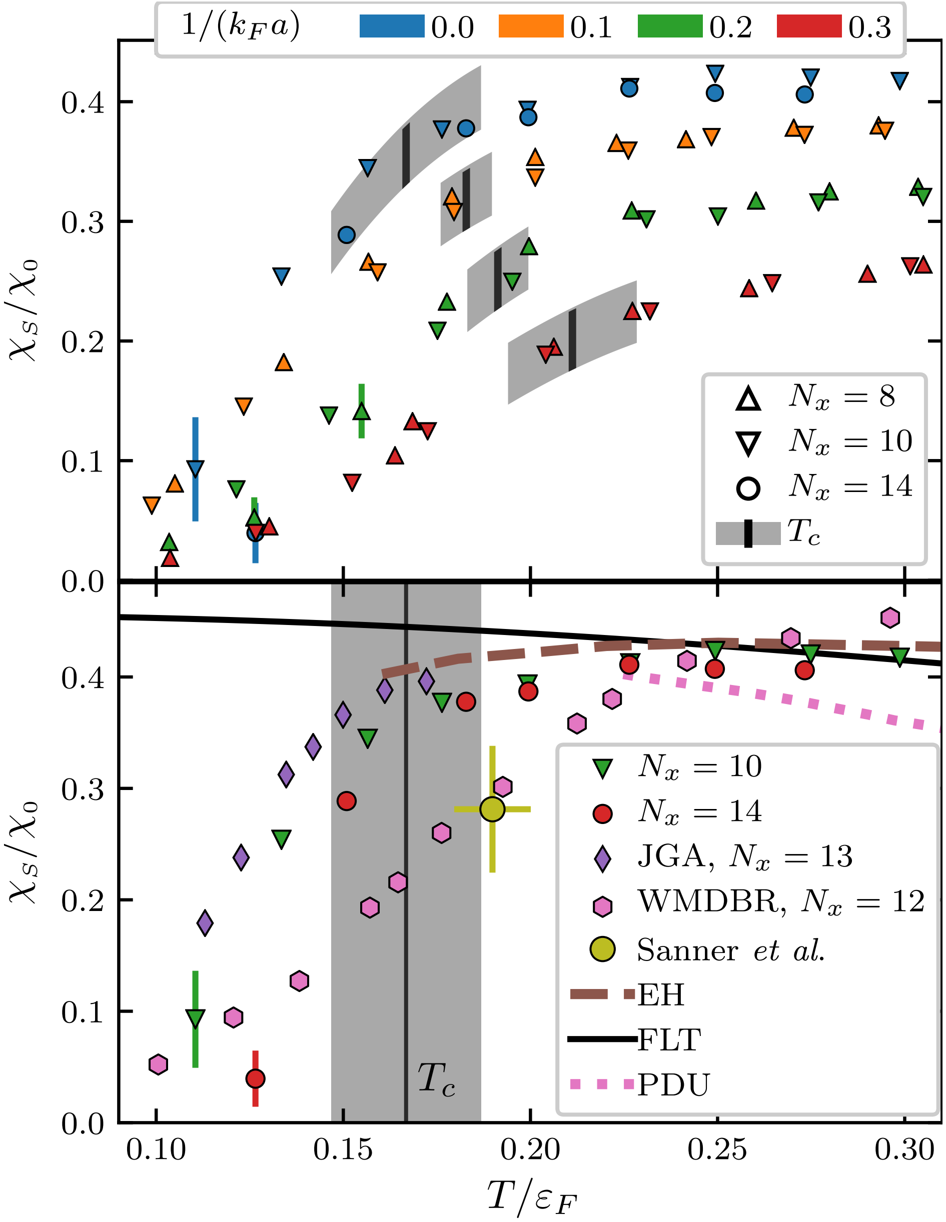

Figure 3.3: Top: AFQMC results for the spin susceptibility χ_s at four different scattering lengths, scaled by its zero-temperature non-interacting counterpart, $\chi_0 = 3N/(2V\varepsilon_F)$. Bottom: At unitarity, we compare our results to two previous AFQMC studies: Jensen *et al.* [107] (JGA) and Wlazłowski *et al.* [211] (WMDBR); the experimental result of Sanner *et al.* [175]; a self-consistent Luttinger-Ward result (EH, [68]); the normal Fermi liquid theory prediction; and a self-consistent NSR result (PDU, [158]).

for the critical temperature $T_c = 0.130(15)\varepsilon_F$. Figure 3.3 also shows our results for the spin susceptibility for $0.1 \leq 1/(k_F a) \leq 0.3$. To our knowledge, these are the first QMC measurements of χ_s away from unitarity.

Tajima *et al.* [188, 187] identified the temperature at which χ_s peaks as T_s, and the temperature range $T_c < T < T_s$ as the "spin-gap" range where there are fewer free spins to contribute to χ_s. Although they find that $T_s \sim T^*$, the exact relationship between these two temperatures requires further study. We present only lower bounds for the temperature T_s in Fig. 3.1 and Table 3.1.

3.4 Even-odd energy staggering gap

The even-odd staggering of systems with fixed particle numbers has been used as a measure of pairing since early studies of nuclear structure [26]. Several finite-difference formulas have been proposed to estimate the energy staggering gap (see Refs [136, 142, 61] for in-depth discussions). The simplest one is the three-point estimate,

$$\Delta_E^{(3)} = \frac{(-1)^N}{2}\left[E(N+1) - 2E(N) + E(N-1)\right], \tag{3.7}$$

where $E(N)$ is the ground state energy of a system with N total particles, which will be achieved when $|N_-| = \mathrm{mod}(N,2)$. The three-point estimate $\Delta_E^{(3)}$ assumes a linear equation of state so that, if the equation of state has positive curvature, $\Delta_E^{(3)}$ will underestimate the pairing gap when N is even and overestimate the pairing gap when N is odd. Instead, we use the five-point expression

$$\Delta_E^{(5)} = \frac{(-1)^N}{8}\sum_{s=\pm 1}\left[4E(N+s) - E(N+2s) - 3E(N)\right], \tag{3.8}$$

In addition to calculating $\Delta_E^{(5)}$, we propose another estimation method, which is to fit the energies calculated for many different values of N and N_- to a two-parameter equation of state,

$$\frac{E}{E_{FG}}(\xi, \Delta_E^{(f)}) = \xi + |N_-|\frac{\Delta_E^{(f)}}{E_{FG}}, \tag{3.9}$$

where $\xi(T/\varepsilon_F, 1/(k_F a))$ is a temperature-dependent generalization of the Bertsch parameter, $\varepsilon_F = (\hbar^2 k_F^2)/(2m)$ is the Fermi energy, $E_{FG} = 3N\varepsilon_F/5$ is the energy of a free Fermi gas at zero-temperature, and we use $|N_-| \in \{0, 1, 2\}$ for the fitting procedure. Regardless of the estimation scheme, we expect Δ_E to become finite below some temperature T^*. If T^* exceeds the critical temperature T_c, this garners support for the existence of a pseudogap.

The pairing gap estimation procedures in Eqs. (3.8) and (3.9) require accurate computation of the ground state energy at fixed particle numbers and reduced temperature T/ε_F. For each grand canonical simulation, we projected fixed, integer-valued particle numbers in the range $\langle N\rangle_{GCE} - 4 \leq N \leq \langle N\rangle_{GCE} + 4$, where $\langle N\rangle_{GCE}$ is the average particle number in the grand canonical ensemble. This range resulted in nine projected particle numbers and was chosen to satisfy $|N - \nu| < 10^{-6}$, where N is the measured particle number and ν is the target particle number. The corresponding energies for these systems were all computed at the same absolute temperature T but had slightly different reduced temperatures T/ε_F due to changes in particle number, thereby spreading the measurements of the pairing gap spread across a range of reduced temperatures centered on the reduced temperature of the grand canonical ensemble. Thus a single GCE simulation constrained to nine different particle numbers, would produce five estimates of $\Delta_E^{(5)}$ at slightly different reduced temperatures. In Appendix C, we discuss these details and further steps involved in correctly calculating these energies.

As the temperature decreases, the grand canonical ensemble becomes more tightly distributed around $\langle\hat{N}\rangle_{GCE}$ and the particle number projection requires sampling farther out into the tails of the GCE, increasing the sampling error. For this reason, errors in the pairing gap estimates become large for low temperatures. Luckily, we are interested in the regime $T_c \leq T \leq T^*$, where the errors are more manageable.

For the five-point difference formula, each fit takes energies from five different particle numbers and $\eta \in \{0, 1\}$. An example stagger plot is shown in Fig. 3.4 for $1/(k_F a) = 0$, $N_x = 8$, and $T/\varepsilon_F = 0.15$, to aid in understanding exactly which points are included in each fit. Each five-point estimate has a different central particle number and therefore

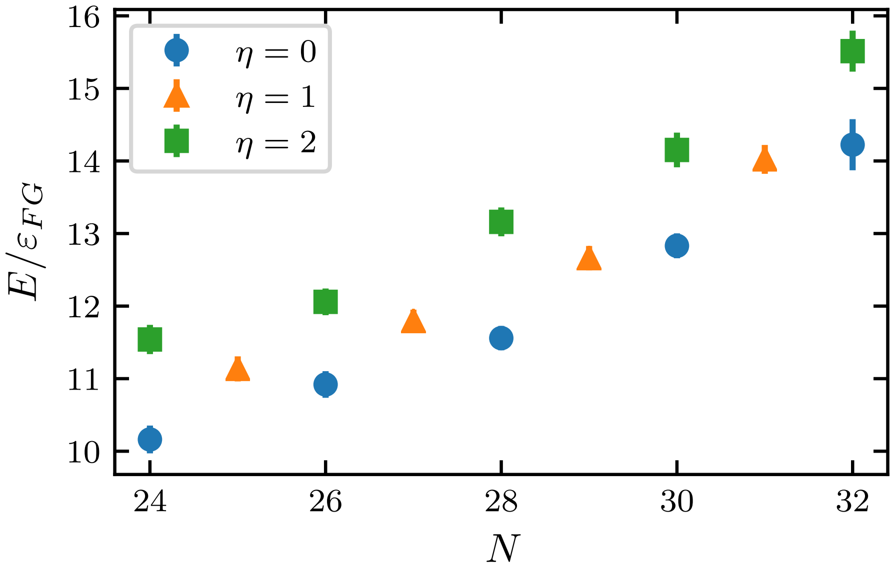

Figure 3.4: An example stagger plot for $1/(k_F a) = 0$, $N_x = 8$, and $T/\varepsilon_F = 0.125$. The energy is normalized to the energy per particle of the free Fermi gas, as in Refs. [43, 49]. We show points for $\eta \in \{0, 1, 2\}$. With nine different particle number values, this stagger plot would yield five estimates of $\Delta_E^{(5)}$ and $\Delta_E^{(f)}$ each.

a different reduced temperature $\widetilde{T} \equiv T/\varepsilon_F$ (further explained in Appendix C.0.3). Each simulation of the GCE therefore generates five different estimates of $\Delta_E^{(5)}$ at five different reduced temperatures centered around the reduced temperature of the GCE. In the left column of Fig. 3.5, we show our results for $\Delta_E^{(5)}$ and compare to previous studies when available.

In addition to estimating Δ_E using the five-point difference, we also estimate Δ_E by fitting the energies to the equation of state in Eq. (3.9) where ξ is a temperature-dependent generalization of the Bertsch parameter (i.e. a dimensionless universal parameter). We show our results for $\Delta_E^{(f)}$ in the right column of Fig. 3.5 and find broad agreement between $\Delta_E^{(f)}$ and $\Delta_E^{(5)}$.

To estimate T^* we fit both $\Delta_E^{(5)}$ and $\Delta_E^{(f)}$ using a univariate cubic spline. This allows

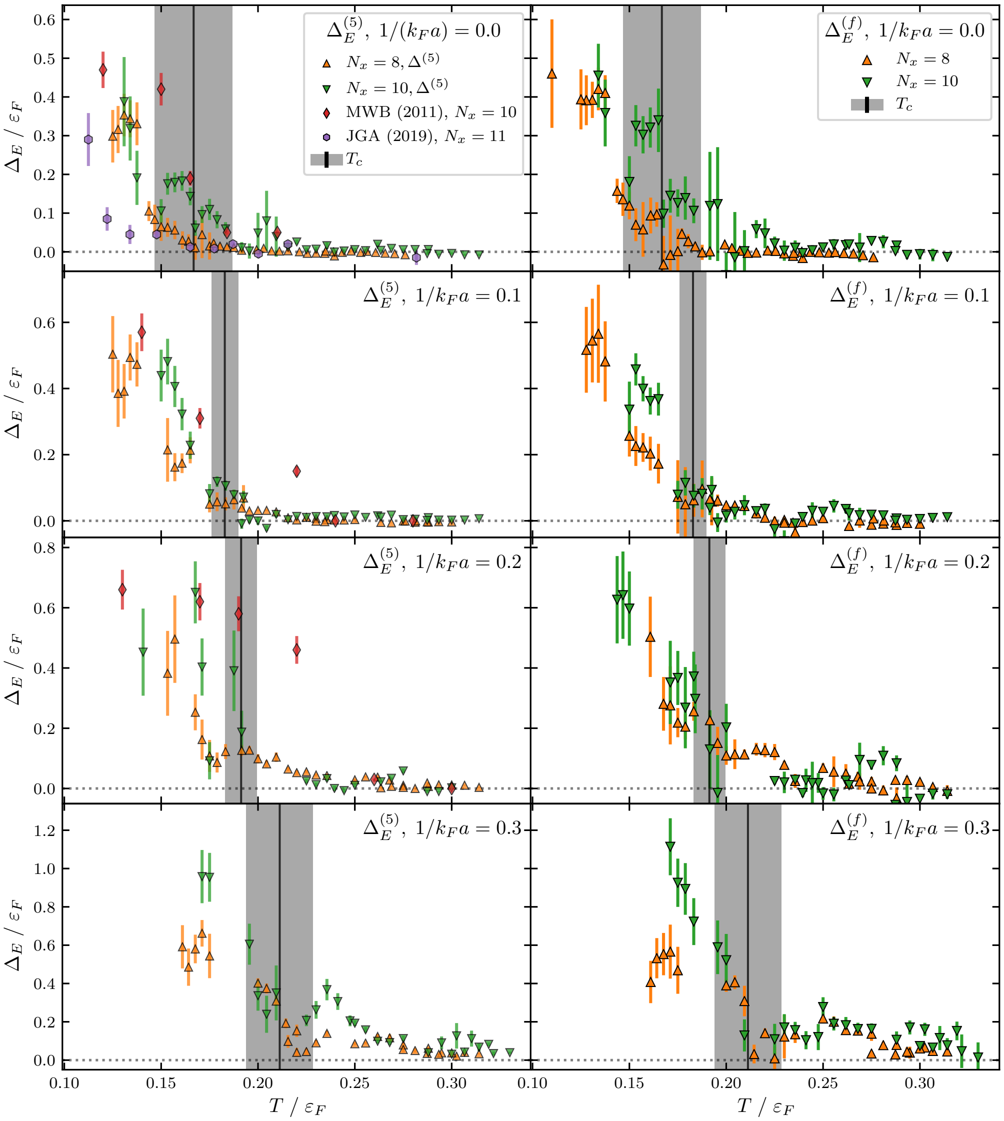

Figure 3.5: (left): The pairing gap Δ_E extracted from even-odd energy staggering using the five-point difference formula, Eq. (3.8). At unitarity, we compare to gap estimates extracted from the spectral weight function (MWB [137]) and to estimates extracted from the three-point even-odd energy staggering (JGA [107]). At $0.1 \leq 1/(k_F a) \leq 0.3$, we compare our results to the MWB values when available. However, the comparison is fraught since they measure the spectral gap, which is *a priori* different from the even-odd energy staggering. (right): AFQMC results for the pairing gap extracted from even-odd energy staggering using Eq. (3.9). The results for $\Delta_E^{(f)}$ are in rough agreement with those for $\Delta_E^{(5)}$.

us to easily compute the roots and derivatives of the interpolant. Denoting the interpolant function by $\widehat{\Delta}$, and the first root of some function f as $\omega[f]$, we then define our estimate for T^* as the minimum of the first root of the interpolant and the first plateau (zero derivative) of the interpolant: $T^* = \min(\omega[\widehat{\Delta}], \omega[\partial_T \widehat{\Delta}])$. Our estimates of T^* are listed in Table 3.1 and depicted in Fig. 3.1.

The temperature "smearing" effect described above combines with the multiple methods for estimating Δ_E to produce a profusion of observations that make it difficult to visualize and compare our results to others. We therefore use a Gaussian process regression model to fit these data and present a predicted distribution for Δ_E. We leave the details of this method to Appendix E and in Fig. 3.6, we present our results for the even-odd pairing gap, derived from both $\Delta_E^{(5)}$ and $\Delta_E^{(f)}$. In the lower panel, we compare our results at unitarity to previous theoretical and experimental studies: an AFQMC measurement of the spectral gap which employed a spherical momentum cutoff (MWB, [137]); a constrained ensemble AFQMC study (JGA, [107]) that estimated $\Delta^{(3)}$ with a cubic cutoff, but without relative temperature corrections, discussed in Appendix C.0.3; two low-temperature experimental results [98, 177]; and a zero-temperature QMC reference result [45]. We can view our results as charting a middle course between the Jensen *et al.* results and the Magierski *et al.* results, all of which can be interpreted as approaching the low-temperature reference results. However, the comparison is fraught since the spectral gap computed by Magierski *et al.* [137] is *a priori* a different quantity than the even-odd pairing gap and the critical temperature computed by Jensen *et al.* is lower than both our estimate and the experimentally determined value.

Despite the large uncertainties at low temperatures, we can appreciate certain features of the pairing gap. It is weaker, compared to the low temperature limit, for temperatures above T_c, however, it cannot be said to vanish immediately above the T_c error band even at unitarity. Our estimates for T^* do not depend on the Gaussian process regression and are derived from spline fits of both $\Delta_E^{(5)}$, see Eq. (3.8), and $\Delta_E^{(f)}$, see Eq. (3.9). They are presented in Fig. 3.1 and Table 3.1 and are comparable with a previous AFQMC study that determined T^* from the spectral gap [137], as opposed to the even-odd energy gap [107].

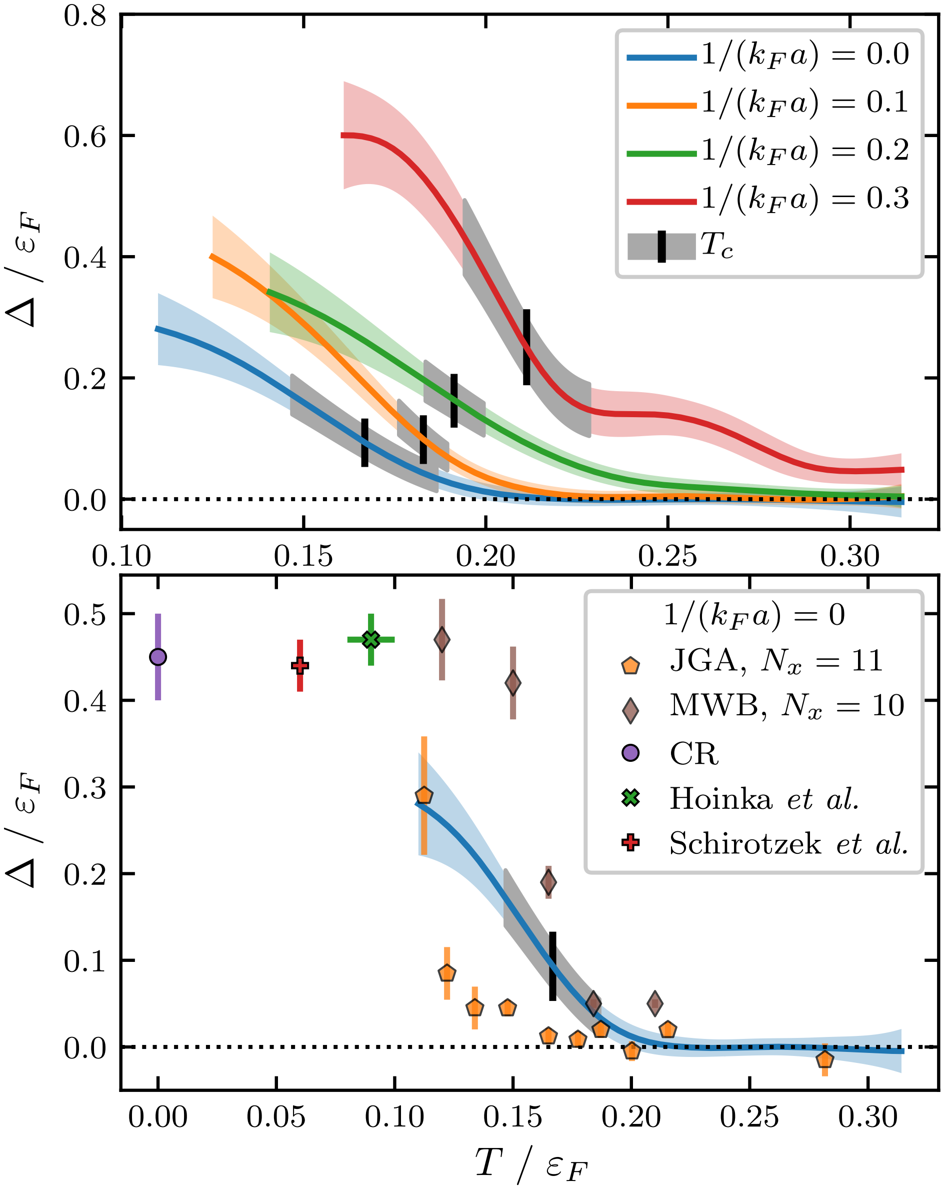

Figure 3.6: Top: AFQMC results for Δ_E at four different scattering lengths, scaled by the Fermi energy ε_F. Bottom: At unitarity, we compare our results to the AFQMC results of Jensen *et al.* [107] (JGA) and Magierski *et al.* [137] (MWB); the zero-temperature QMC prediction of Carlson and Reddy [45] (CR); and the experimental results of Hoinka *et al.* [98] and Schirotzek *et al.* [177].

3.5 Tan Contact, C

In addition to thermodynamic probes measured in the main text, we also calculate the Tan contact C, which parameterizes all short range correlations in the system. It is a central property of systems of fermions with large scattering lengths, with relations concerning the tail of the momentum distribution [189],

$$C \equiv \lim_{k\to\infty} k^4 n_\sigma(k), \tag{3.10}$$

where $n_\sigma(k)$ is the momentum distribution for particles with spin σ and momentum k; the thermodynamic derivative of the free energy with respect to the scattering length [191]

$$\frac{\partial F}{\partial a^{-1}} = -\frac{\hbar^2}{4\pi m}C; \tag{3.11}$$

and the pressure and energy density of a homogeneous system [190]:

$$\mathcal{P} = \frac{2}{3}\mathcal{E} + \frac{\hbar^2}{12\pi m a}C. \tag{3.12}$$

See Braaten [28] for a review of the Tan contact.

Following Jensen *et al.* [105], we calculate C in the lattice formulation as

$$C = \frac{m^2 g \left\langle \hat{V} \right\rangle}{\hbar^4}, \tag{3.13}$$

where $\langle \hat{V} \rangle$ is the expectation value of the potential energy operator. In Fig. 3.7, we show our results for the Tan contact at multiple scattering lengths, with shaded boxes indicating the critical temperature, with error bounds. The Tan contact increases as we increase $1/(k_F a)$ and decreases with decreasing temperature.

To our knowledge, our results for $0.1 \leq 1/(k_F a) \leq 0.3$ are the first published finite-temperature estimates of the Tan contact away from unitarity, thus preventing comparison to previous results. However, at unitarity we compare our results to previous studies in the lower panel of Fig. 3.7.

Positing a link between contact and pairing, Pieri *et al.* [163] have argued that the Tan contact measures local pairing as $C = (m\Delta_\infty)^2$. This parameter was first introduced by

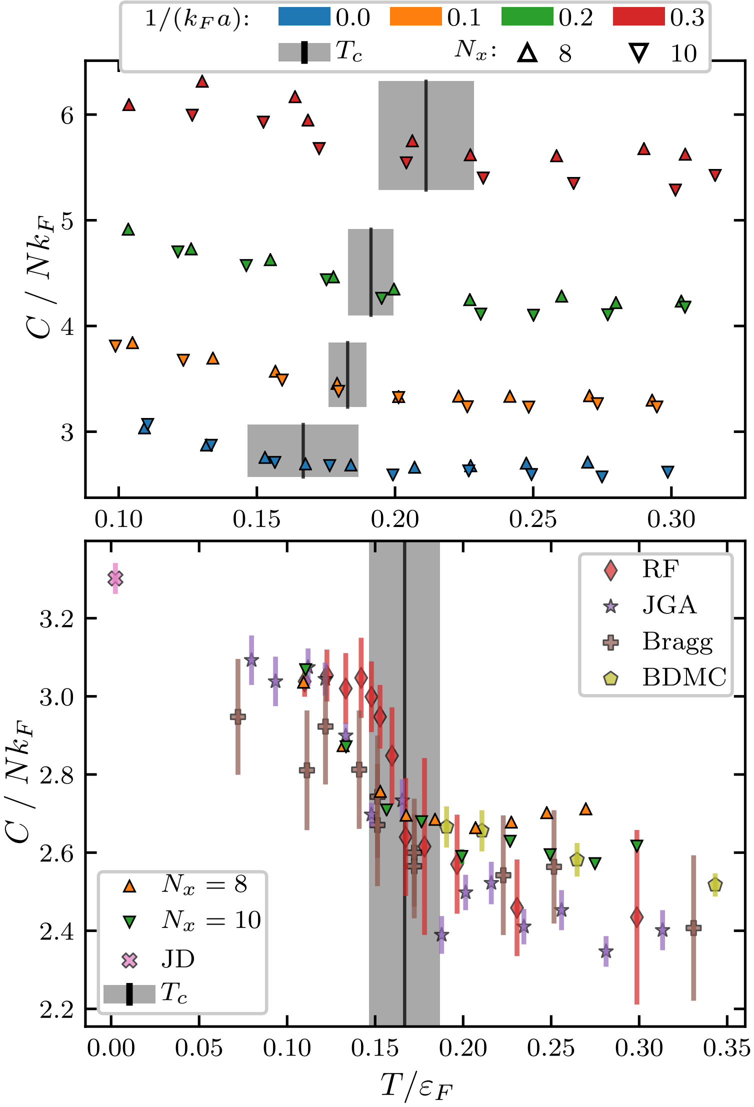

Figure 3.7: The Tan contact derived from Eq. (3.13) for $0.0 \leq 1/(k_Fa) \leq 0.3$. (upper panel) The Tan contact decreases monotonically as temperature increases and increases as $1/(k_Fa)$ increases. Shaded boxes indicate the critical temperature and error bars for the contact estimates are within the marker size. (lower panel) We compare to other studies: experimental results based on radio frequency spectral response [145] (RF); an experimental study using focused beam Bragg spectroscopy [42] (Bragg); a previous QMC study at zero temperature from Drut [59] (JD); a bold diagrammatic Monte Carlo result [171] (BDMC); and a previous constrained ensemble AFQMC study [105] (JGA).

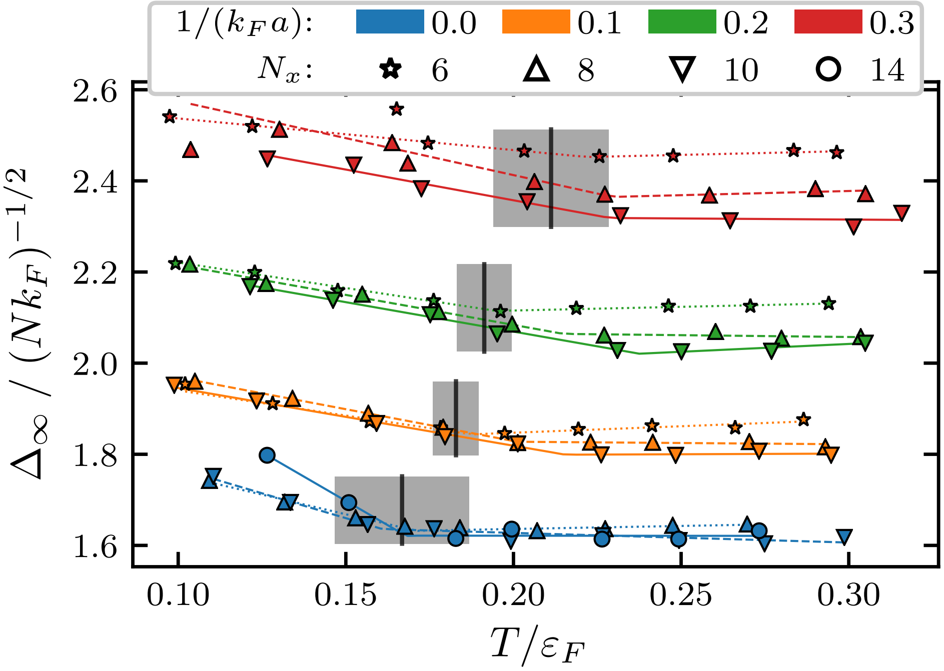

Figure 3.8: AFQMC results for the contact-derived pairing parameter Δ_∞ using Eq. (3.14). Δ_∞ displays clearly different low and high temperature structure. We fit a piece-wise linear function and define the "switching temperature" as a new characteristic temperature, T_∞. We record T_∞ in Table 3.1.

Pieri *et al.* [163] and later generalized by Rossi *et al.* [171]. However, the exact relationship between Δ_∞ and the superconducting order parameter Δ remains elusive. In Fig. 3.8, we show our normalized results for Δ_∞ derived from the Tan contact using

$$\frac{\Delta_\infty}{\sqrt{N k_F}} \equiv \frac{1}{m}\sqrt{\frac{C}{N k_F}}. \tag{3.14}$$

We find no obvious relationship between Δ_∞ and the even-odd staggering pairing gap. However, Δ_∞ has distinct low- and high-temperature behaviors, with an almost linear decrease from a maximum at the lowest temperature to a "switching temperature" where Δ_∞ levels off or, in the case of small lattices, increases gradually. We fit these curves to a piece-wise linear fit and record the "switching" temperature as a new characteristic temperature, T_∞, in Table 3.1.

However, we caution that our identification of T_∞ is a speculative characteristic temperature. We therefore refrain from making inferences about the pseudogap using measurements of Δ_∞ or T_∞ until the relationship between Δ_∞ and the pairing gap Δ is clarified. This issue warrants further study.

3.6 Energy per particle

The fitting function in Eq. (3.9), which parameterizes the energies of system with various numbers of $N_{\uparrow,\downarrow}$ particles, also allows us to estimate the temperature- and coupling constant-dependent Bertsch parameter $\xi(T/\varepsilon, 1/(k_F a))$. We show our estimates for $\xi(T)$ in Fig. 3.9. Because these results are obtained from fitting energies calculated in the constrained ensemble, we do not expect high precision results like those in [60]. However, the estimates of ξ do serve as a consistency check on the constrained ensemble. We can also check the consistency of the Tan contact using Eq. (3.11):

$$\frac{\partial E}{\partial 1/(k_F a)} = \frac{\hbar^2 k_F C}{4\pi m}, \tag{3.15a}$$

$$\Rightarrow \frac{\partial \xi(T)}{\partial\,(k_F a)^{-1}} = \frac{\partial\,(E\,/\,E_{FFG})}{\partial\,(k_F a)^{-1}} = -\frac{5}{6\pi}\frac{C}{N k_F}. \tag{3.15b}$$

In the lower panel of Fig. 3.9, we use Eq. (3.15b) to shift all estimates of $\xi(T)$ for $0.1 \leq 1/(k_F a) \leq 0.3$ up to unitarity. This application of the Tan contact derived from the GCE to an equation of state derived from the doubly constrained (both N_+ and N_-) ensemble serves as a consistency check on our Tan contact results and the constrained ensemble method.

Using the Gaussian process regression procedure described in Appendix E, we combine our measurements of ξ from Eq. (3.9) with our measurements of the energy E/E_{FFG} from the GCE, to produce an expected distribution of $\xi(T/\varepsilon_F, 1/(k_F a))$. In Fig. 3.10 we show these results for each scattering length and compare to previous results. Similar to the results by Drut *et al.* [60] at unitarity, we did not capture the curvature in the equation of state seen by Ku *et al.* [114] below T_c. However, our results at unitarity do approach the reference values at zero temperature. We have a similar level of agreement with the results of Van Houcke *et*

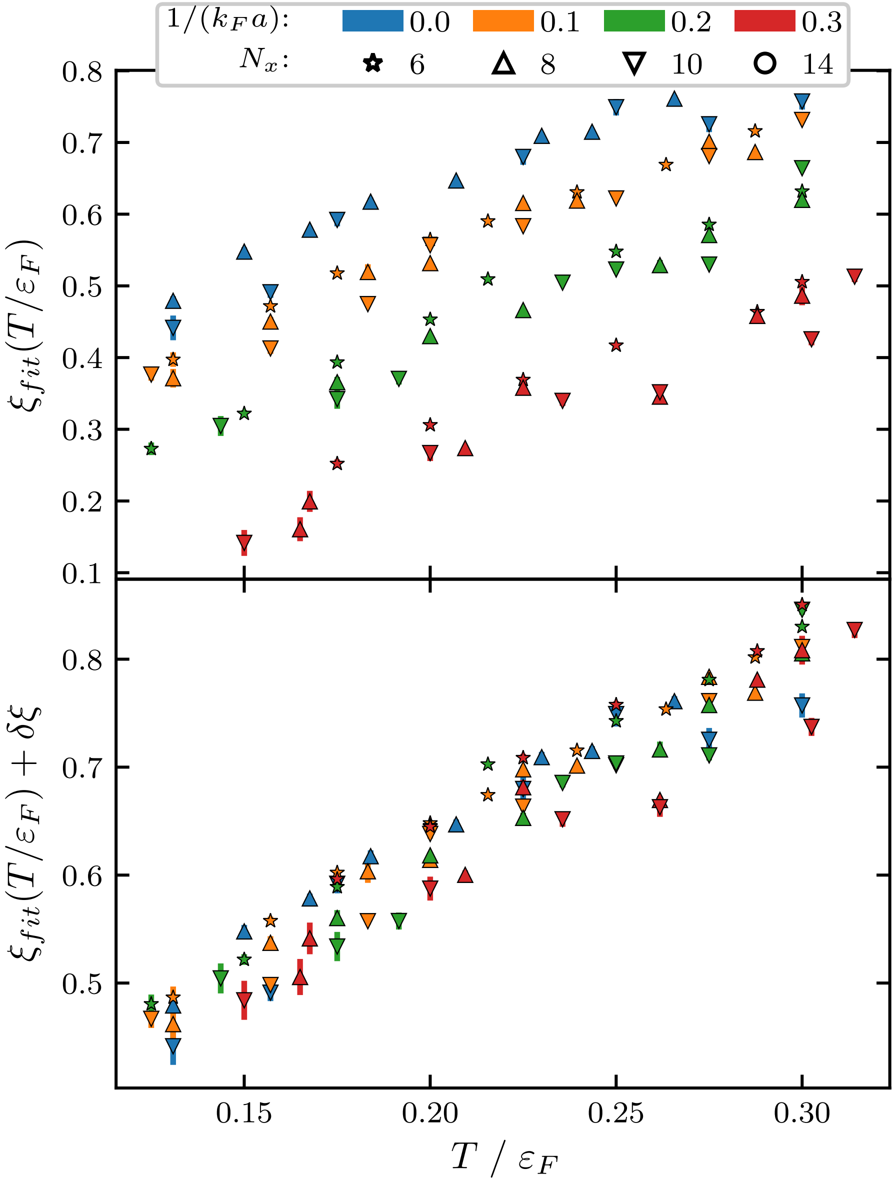

Figure 3.9: AFQMC results for the temperature dependent Bertsch parameter $\xi(T)$ obtained by fitting energies to Eq. (3.9). In the upper panel, we show our results for $\xi(T)$ at $0.0 \leq 1/(k_F a) \leq 0.3$. In the lower panel, we show $\xi(T) + \delta\xi$, where $\delta\xi$ is the energy shift obtained from the Tan contact defined in Eq. (3.15b).

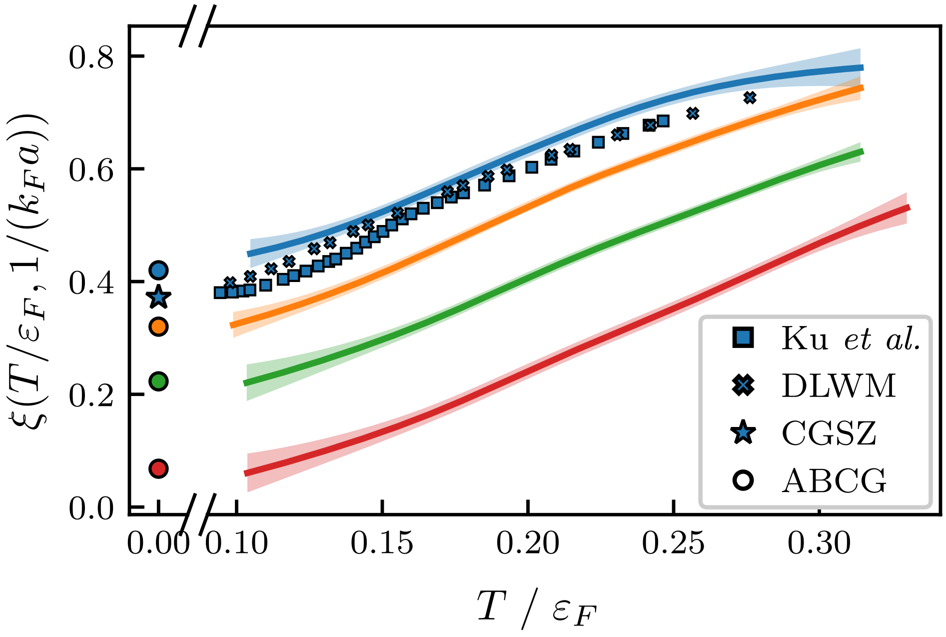

Figure 3.10: AFQMC results for the temperature-dependent Bertsch parameter, $\xi(T/\varepsilon_F, 1/(k_Fa))$ at four different scattering lengths. At unitarity, we compare our results to the experimental measurements of Ku *et al.* [114] and the high-precision AFQMC results of Drut *et al.* [60] (DLWM). We also show the zero temperature predictions of Carlson *et al.* [44] (CGSZ) at unitarity and of Astrakharchik *et al.* [9] (ABCG) at all scattering lengths.

al. [199], which are not shown in Fig. 3.10, but are in excellent agreement with experiment in the normal state. We provide a table of values and errors for both ξ and Δ in Appendix E.

3.7 Summary

In this chapter, we presented results from the first *ab initio* finite-temperature calculations of the spin susceptibility χ_s and Tan contact C away from unitarity, in addition to estimates for the condensate fraction α, the critical temperature T_c, the even-odd pairing gap Δ_E, and the Bertsch parameter ξ. For both the spin susceptibility and the even-odd pairing gap, we found no discontinuities as we reduce the coupling, but rather a smooth reduction in pseudogap signatures.

Since the BCS–BEC crossover is smooth, we should not expect an abrupt and discontinuous emergence of the pseudogap. Questions about where the pseudogap emerges are therefore analogous to long-debated questions about where the Earth's atmosphere ends [84, 139]. Since the field is young, we have not yet developed the pseudogap analog of the Kármán line from space science. We have provided context to this discussion by looking for signatures of the pseudogap between $0.0 \leq 1/(k_F a) \leq 0.3$. At $1/(k_F a) = 0.3$, we see strong pseudogap signatures, which diminish towards unitarity. However, all characteristic temperatures T^* in Fig. 3.1 exceed the critical temperature T_c at all scattering lengths. Based on our results, we conclude it is premature to exclude unitarity from the pseudogap regime. Future work should include more refined extrapolations to the limit of zero-effective range, infinite volume, and zero density.

Chapter 4

NEUTRON MATTER

As noted in the earlier chapters, the unitary Fermi gas is experimentally realized in cold-atom systems. One might reasonably ask why I've spent so much time examining a cold-atom system while working as a graduate student in a *nuclear theory* group. Aside from the sheer intellectual enjoyment of contemplating the crossover, the unitary regime garners attention across many subfields of physics. Since the fermion density is the only dimensionful scale, the properties of the system are expected to be universal, in the sense that they should be independent of the microscopic details of the interparticle interaction. More specifically, the unitary Fermi gas is an idealization of dilute nuclear matter [20], with a neutron-neutron s-wave scattering length of $a_{nn} \approx -18.5$ fm [99, 86], which is much larger than the effective range of $r_0 \approx 2.7$ fm. Therefore, aside from the intrinsic value of studying the unitary regime, one can view it as a "warm-up" problem for the understanding of nuclear matter.

In this chapter, we take a logical next step in this endeavor and apply the techniques of Chapter 2 to study the ground state and quasiparticle properties[1] of infinite neutron matter (INM), which is an idealized system of a large number of neutrons interacting through nuclear forces. At low-densities ($n \ll n_0$, where $n_0 = 0.16$ fm^{-3} is the saturation density of matter inside nuclei), the properties of INM are crucial to understanding neutron-rich nuclei. At intermediate to high densities ($n \sim n_0$), an understanding of INM is critical to understanding the properties of neutron stars [75].

---

[1] We have encountered quasiparticles throughout this dissertation (e.g. Bogoliubov's quasiparticles in § 1.2.1). See Ref. [1] for a pedagogical introduction to Fermi liquid theory and the quasiparticle picture.

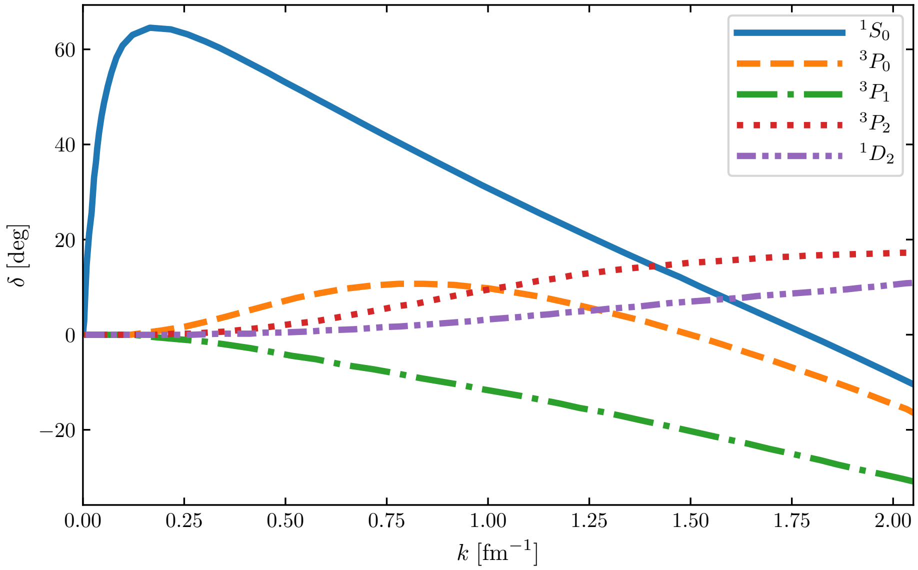

Figure 4.1: Neutron-proton phase shifts δ as a function of wave number k for different partial waves. Modified from Ref. [77].

4.1 Neutron-neutron interactions

At very low densities, the neutron-neutron (nn) interaction can be related to the tunable interactions in the cold-atom systems considered in Chapter 3. However, as the density increases, different partial waves, beyond s-wave scattering, and different spin-states contribute to the nn-interaction and we must modify the AFQMC methods of Chapter 2 to accommodate more complicated, long-range interactions. The different contributions to the interaction can be organized using the spectroscopic notation $^{2S+1}L_J$, where $L \in \{S, P, D, F, \ldots\}$ is the orbital angular momentum, the exponent $2S+1$ is either $2\cdot 0+1 = 1$ for the spin singlet case or $2\cdot 1+1 = 3$ for the spin triplet case, and J is the total angular momentum, which takes values $J \in \{L+S, L+S-1, \ldots |L-S|\}$. In Fig. 4.1, we show the neutron-proton scattering phase shifts (defined in Appendix A) for each partial wave as a function of the nucleon wave number k. At low momentum (i.e. low density) the $^1S_0$ channel dominates and we could very well consider only the s-wave scattering as we did for the Fermi gases in Chapter 3.

However, as we increase the density, the $^1S_0$ phase shift becomes negative, corresponding to a repulsive interaction, and the other partial waves, particularly $^3P_2$, begin to dominate. So in contrast to electrodynamics, where the interaction is spin-independent, the nucleon-nucleon interaction is highly dependent on spin and isospin. An illustrative example of this dependence can be seen when comparing the bound deuteron, with total isospin $T = 0$, with the unbound dineutron, with total isospin $T = 1$.

To account for this, the nuclear physics community has traditionally expressed the nn-potential as a sum of potentials, each tuned to reproduce phase shifts of the kind in Fig. 4.1. The most established of these approaches results in the Argonne family of potentials [209], usually named for the number of spin-isospin-dependent operators in the sum. For example, the Argonne v8' potential is [208]

$$V_{12} = \sum_{p=1}^{8} v_p(r) O_{12,p}, \quad \text{with} \quad O_{12,p} = (1, \sigma_1, \sigma_2, S_{12}, \mathbf{L} \cdot \mathbf{S}) \cdot (1, \tau_1 \cdot \tau_2)\,, \tag{4.1}$$

and $\mathbf{S} = \sigma_1 + \sigma_2$ is the total spin, $\mathbf{L} = -i\mathbf{r} \times (\nabla_1 - \nabla_2)$ is the relative angular momentum, $\tau_1 \cdot \tau_2$ is the isospin state, which can only be one (i.e. triplet) for pure neutron matter. The tensor component $S_{12} = 3(\sigma_1 \cdot \hat{\mathbf{r}})(\sigma_2 \cdot \hat{\mathbf{r}}) - \sigma_1 \cdot \sigma_2$, depends on the interaction between the nucleon spins and angular momentum.

A more modern approach is to employ chiral effective field theory (χ-EFT) to draw connections with the symmetries of the underlying theory of quantum chromodynamics [135].

Generally speaking, effective field theories are modern theoretical tools used to exploit a large hierarchy of scales in physical systems. See Refs. [108, 40] for pedagogical introductions and further references to the vast literature on effective field theories. For the nn-interaction, this separation of scales comes from the difference between the pion mass and the vector meson masses, which establish a hard momentum scale where the χ-EFT is expected to break down. The aim of χ-EFT then is to expand the nn-interaction into a hierarchy of terms involving powers of the ratio between the two masses. One then computes observables to a desired order in this hierarchy, producing calculations at leading order (LO), next-to-leading order (NLO), next-to-next-to-leading order (N^{2}LO), and so on. Three-body interactions do not appear until N^{2}LO.

The de facto χ-EFTs in low energy nuclear theory are provided by Entem and Machleidt [135] and Epelbaum *et al.* [69], though there are certainly other χ-EFT potentials from which to choose [78, 79, 66]. We use the Entem and Machleidt χ-EFT with two-body interactions up to N^{3}LO and three-body interactions up to N^{2}LO.

We refer the reader to Ref. [135] for an extensive review of the interaction terms at each order. In practice, we use the imaginary-time-evolved wavefunctions to compute momentum-space density matrices and then use those density matrices to calculate the chiral interaction terms. Appendix F contains the details of computing the two-body interactions given a set of time-evolved density matrices. For three-body interactions, we compute using a technique involving the traces of $\mathscr{M}d^{-1}$ matrices, which are defined in Appendix G along with further details. This technique reduces computational cost at the expense of more memory consumption for storing the $\mathscr{M}d^{-1}$ matrices.

4.2 *Evolution Hamiltonians*

The treatment of the full chiral Hamiltonian using QMC methods suffers from a severe sign problem. To avoid this problem, we follow Wlazłowski *et al.* [210] and rewrite the Hamiltonian using an evolution potential,

$$\hat{H} = \underbrace{\hat{K} + \hat{V}_{\text{ev}}}_{\hat{H}_{\text{ev}}} + \underbrace{\hat{V} - \hat{V}_{\text{ev}}}_{\delta\hat{V}}, \tag{4.2}$$

so named because it is used in the imaginary time evolution of AFQMC. This rewriting will be useful only if two conditions are satisfied:

1. $\hat{H}_{\text{ev}}$ should be solvable by AFQMC without a sign problem.

2. $\delta\hat{V}$ should be small enough to be treated using first order perturbation theory,

$$E \leq \langle\psi_0|\hat{H}|\psi_0\rangle \approx \langle\psi_0|\hat{H}_{\text{ev}}|\psi_0\rangle + \langle\psi_0|\delta\hat{V}|\psi_0\rangle\,, \tag{4.3}$$

   where ψ_0 is given in Eq. (2.13).

Luckily, Wlazłowski *et al.*did the arduous work of constructing such an evolution Hamiltonian for neutron matter, arriving at a momentum-space attractive evolution potential inspired by the one-boson exchange model,

$$V_{\text{ev}}(q) = \sum_{\alpha \in \{\pi,\sigma,\omega\}} \frac{V_\alpha}{m_\alpha^2 c^2 + q^2} f(q), \tag{4.4}$$

where the regulator function is $f(q) = \exp[-(q/\Lambda)^{30}]$, and $\Lambda = 414$ MeV/c is the chiral symmetry breaking scale. The coupling constants V_α and masses m_α are fitting parameters determined by minimizing

$$\chi^2 = \sum_{i,j} w^{(j)} \left[\delta^{(j)}_{\text{EFT}}(E_i) - \delta^{(j)}_{\text{ev}}(E_i)\right] + \alpha \left[E^{(\text{pert.})}_{\text{EFT}} - E^{(\text{pert.})}_{\text{ev}}\right]^2, \tag{4.5}$$

where $\delta^{(j)}(E_i)$ are the phase shifts for partial waves $j \in w\{{}^1S_0, {}^3P_0, {}^3P_1, {}^3P_2\}$ and the subscripts EFT and ev indicate that the phase shifts were calculated for the chiral N^{3}LO and evolution potential, respectively. The weights $w^{(j)}$ correspond to the degeneracy of the partial waves so that $w^{(j)} \in \{1, \frac{1}{9}, \frac{3}{9}, \frac{5}{9}\}$.

In Fig. 4.2, we show the evolution potentials as a function of the momentum transfer q. As we increase the density the evolution potential become less attractive, corresponding with the presence of repulsive forces at high density that we saw in Fig. 4.1.

Having constructed the evolution potential, we then use the methods of Chapter 2 with the continuous HST of Eq. (2.24). We performed simulations of neutron matter on a cubic lattice of size $N_x = 10$, $\ell = 1.4974$ fm, with particle numbers from 38 to 342, corresponding to densities ranging from 0.01 fm^{-3} to 0.10 fm^{-3}. The particle numbers are chosen to completely fill the Cartesian shells in our reciprocal cubic lattice. We extrapolate energies to the thermodynamic limit using Eq. (C.5) as we did for the BCS–BEC crossover.

4.3 Energy equation of state

In Fig. 4.3 we present our results for the energy equation of state (EoS) of pure neutron matter. We show our results for the chiral Hamiltonian with two-nucleon forces (2NF) only

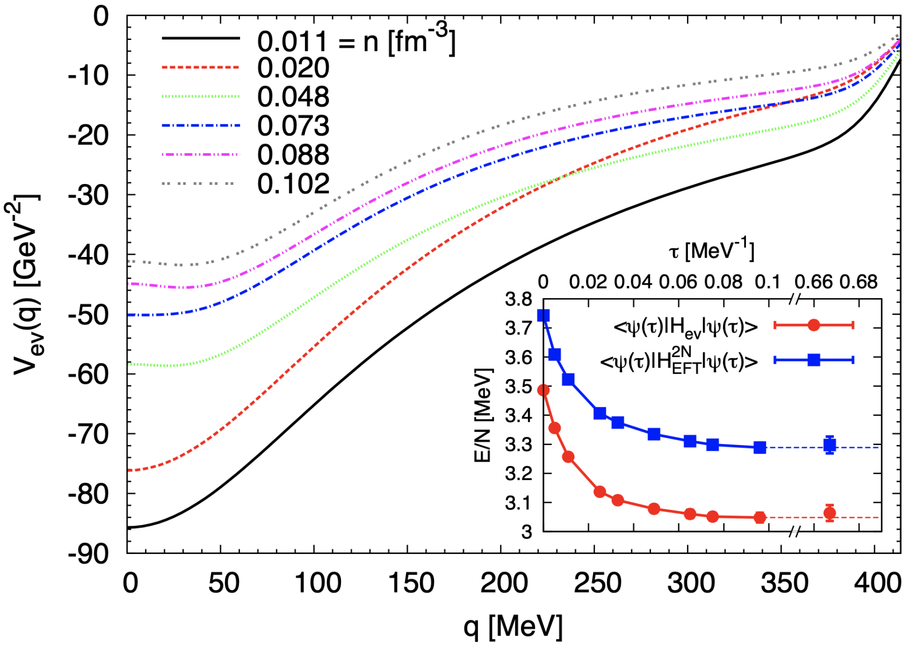

Figure 4.2: Momentum-space evolution potentials for the neutron-neutron interaction. Note that the evolution potential is density dependent. The inset shows the discrepancy between the expectation value of the energy using the evolution potential (red circles) and the two-body chiral potential (blue squares) for the density $n = 0.011\text{fm}^{-3}$. Reproduced with permission from Ref. [210].

and for the full Hamiltonian with both two- and three-body forces (2NF + 3NF). For the 2NF results, we show broad agreement with two previous χ-EFT QMC studies from Roggero *et al.* [169] and Gezerlis *et al.* [79], and of course with the results of Wlazłowski *et al.* [210] on which our method is based. The inclusion of three-nucleon forces increases the energy per particle, making the system more repulsive above $n = 0.02$ fm^{-3}. Where appropriate, we also plot the equation of state fitted using an expansion in powers of the Fermi momentum,

$$\frac{E(n)}{N} = \frac{3}{5}\frac{\hbar^2}{2m_n}\left(3\pi^2 n\right)^{2/3}\left(a + bn^{1/3} + cn^{2/3}\right), \tag{4.6}$$

where $n \equiv N/V$ is the number density of the neutron matter and a, b, and c are fitting parameters. For our 2NF + 3NF results, we find $a = 0.7819(18)$, $b = -1.327(10)$, and $c = 1.471(14)$. A similar fitting procedure is used in [37]. We use this fit to determine the chemical potential as

$$\mu(n) = \left(\frac{\partial E}{\partial N}\right)_V = n\frac{\partial E(n)/N}{\partial n} + \frac{E(n)}{N} = \frac{3}{5}\frac{\hbar^2}{2m_n}\left(3\pi^2 n\right)^{2/3}\left(\frac{5}{3}a + 2bn^{1/3} + \frac{7}{3}cn^{2/3}\right), \tag{4.7}$$

which we use later when extracting the self-energy.

4.4 Quasiparticle excitation (QPE) spectrum

The energy EoS shows good agreement with previous studies but our main goal and novel contribution is to relate the ab-initio calculations of neutron matter to compute the quasiparticle excitation spectrum and fit it to Landau's Fermi liquid theory of quasiparticles. Specifically, we wish to probe the energy dispersion relation

$$\varepsilon(p) = \sqrt{\left(\frac{p^2}{2m^*} - (\mu - U)\right)^2 + \Delta^2}, \tag{4.8}$$

where the fitting parameters m^*, μ, U, and Δ are the quasiparticle effective mass, chemical potential, self-energy, and pairing gap, respectively.

Note that from the fitting procedure alone, we can only solve for the combined parameter $\widetilde{U} \equiv \mu - U$. However, we can estimate the chemical potential from the equation of state using $\mu = \partial E/\partial N$, where E is the total energy and N is the particle number.

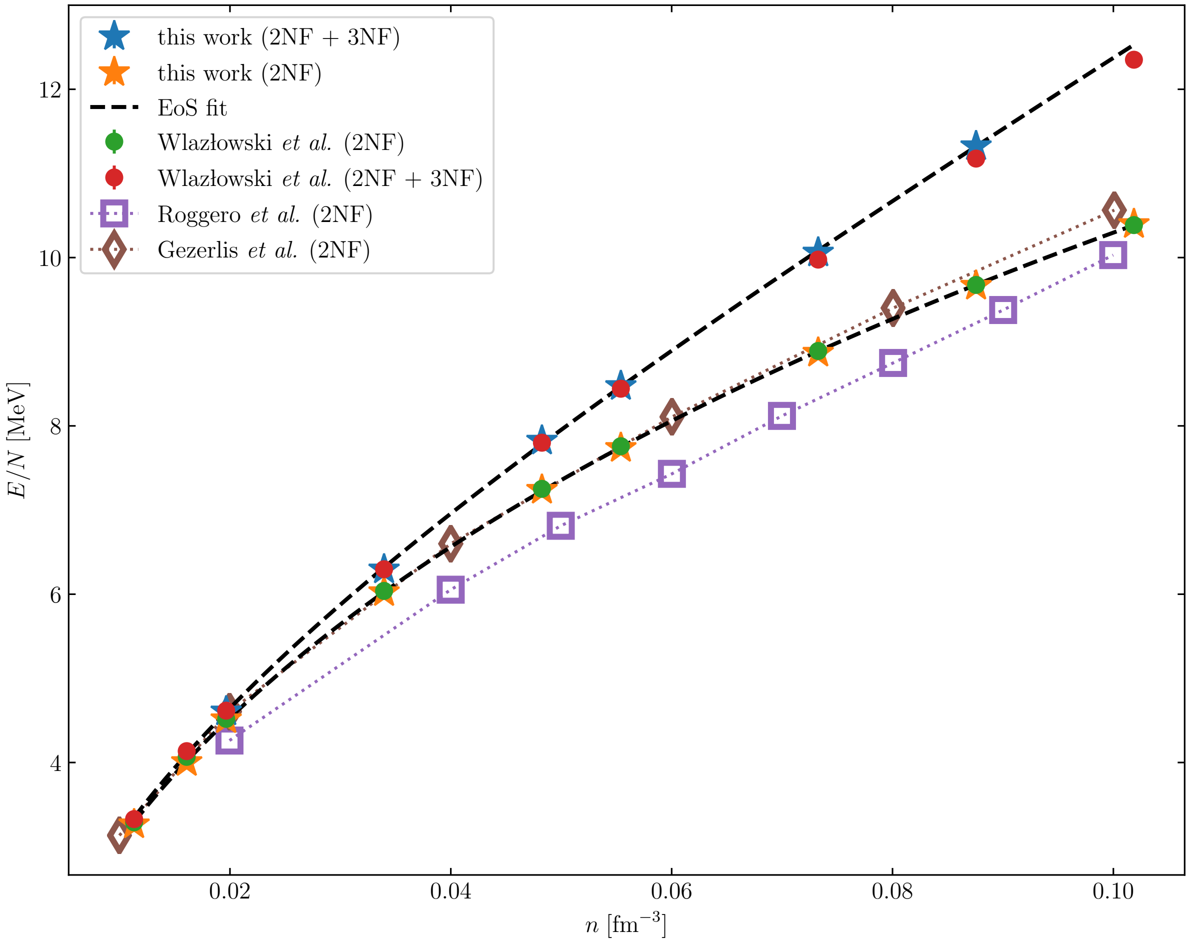

Figure 4.3: AFQMC results for the energy equation of state of pure neutron matter. Blue stars indicate our results, while orange stars denote results using two-body interactions only. Green circles indicate the results of Wlazłowski *et al.* [210], while red circles denote the same reference results for two-body interactions only. We also compare our results to two QMC calculations with two-body forces alone: Gezerlis *et al.* [79] and Roggero *et al.* [169], with which our two-body results are in broad agreement.

To estimate the quasiparticle energy (i.e. the left-hand side of Eq. (4.8), we compute difference between (a) the energy of an odd system with $N-1$ neutrons and total momentum p and (b) the ground state energy of a nearby even system projected onto the same particle number, $N-1$:

$$\varepsilon(p) = E(p, N-1) - E_{\text{even}}(N-1). \tag{4.9}$$

There are several strategies from which to compute $E_{\text{even}}(N-1)$. The most common approach is to use the average of the ground state energies for the systems with N and $N-2$ particles, which leads to a three-point estimation of the quasiparticle energy,

$$\varepsilon(p) = E(p, N-1) - \frac{1}{2}(E_0(N) + E_0(N-2)). \tag{4.10}$$

Alternatively, one can use a higher-order difference formula to estimate the pairing gap [17]. In this study, we calculate $E_{\text{even}}(N-1)$ using

$$E_{\text{even}}(N-1) = E_0(N) - \frac{\partial E_0^{(\text{EoS})}(N)}{\partial N} + \frac{1}{2}\frac{\partial^2 E_0^{(\text{EoS})}(N)}{\partial N^2}, \tag{4.11}$$

where $E_0^{(\text{EoS})}$ is the ground state given by the equation of state of even neutron matter, calculated from the even energies.

The method described in § 4.2 calculates the energies of unpolarized (or "even") systems. However, for the calculation of the quasiparticle spectrum, we require the energies of spin polarized ("odd") systems, for which there is a sign problem. To combat this sign problem, we use the reweighting technique, described in § 2.3.2 and exclude any reweighted observables that fall outside the reweighting range (see Eqs. (2.48) to (2.50)) defined by the variances in our simulations of the even systems.

Specifically, probe momenta below the Fermi momentum we remove a particle with momentum $-p$ below the Fermi level. Since the even system is composed of an equal number of particles with momenta $\pm p$, this induces a net p momentum to the rest of the system. Conversely, to probe momenta above the Fermi level, we must add a particle with momentum p to the system. These two procedures give us the "lower branch" of the quasiparticle spectrum with $p \leq p_F$ and the "upper branch" of the quasiparticle spectrum with $p > p_F$. However, this means that the upper branch energies correspond to a system at a slightly higher density and must be brought back to the same density as the lower branch by a Taylor expansion of the same form as Eq. (4.11).

4.5 *Determining QPE parameters*

Once we have the quasiparticle energies calculated from Eqs. (4.9) and (4.11), we can determine the parameters given in Eq. (4.8).

4.5.1 Effective mass

The scaled quasiparticle spectrum may be approximated by

$$\frac{\varepsilon(p)}{\varepsilon_F} = \sqrt{\left(\frac{m}{m^*}\frac{p^2}{p_F^2} - \frac{\widetilde{U}}{\varepsilon_F}\right)^2 + \left(\frac{\Delta}{\varepsilon_F}\right)^2} \approx \left|\frac{m}{m^*}\frac{p^2}{p_F^2} - \frac{\widetilde{U}}{\varepsilon_F}\right|, \tag{4.12}$$

which is only valid away from the Fermi momentum. Separating the quasiparticle spectrum into upper and lower branches, we have

$$\frac{\varepsilon(p)}{\varepsilon_F} \approx \Theta(p)\left[\frac{m}{m^*}\frac{p^2}{p_F^2} - \frac{\widetilde{U}}{\varepsilon_F}\right], \tag{4.13}$$

where $\Theta = 1$ on the upper branch and $\Theta = -1$ on the lower branch. To estimate the effective mass, we fit the scaled quasiparticle energy using a linear fit, using separate fits for the upper and lower branches and removing the point nearest the Fermi level.

In Fig. 4.4, we show our results for the INM effective mass calculated using only two-body forces, while in Fig. 4.5, we show the same quantities calculated using two- and three-body forces. In the top left panel, we show the scaled quasiparticle energy $\varepsilon(p)/\varepsilon_F$ as a function of the scaled squared momentum $(p/p_F)^2$. In these units, the bare mass, indicated by the dashed lines, has a slope of one. The lower branch values have been multiplied by -1 and shifted up by 1 to ease the comparison with the upper branch. In the top right panel, we show the effective masses extracted from the linear fit in Eq. (4.13), with separate effective masses extracted for the upper and lower branches alongside the average of the two.

For both the 2NF and 2NF + 3NF results, the upper and lower branch estimates are systematically different. Recall that the lower branch energies were created by removing a particle with momentum p while the upper branch energies were calculated by adding a particle with momentum p. The difference in the upper and lower branch effective masses (and self-energies as we will see in the next section) is therefore analogous to the difference between ionization and affinity energies in atomic physics, where the ionization energy is the energy required to remove an electron, while the affinity energy is the energy required to add an electron. However, for infinite matter in the thermodynamic limit, we expect that the two quantities should be identical. We therefore interpret our differing branch estimates as a sign that we have not approached the thermodynamic limit with our 10^3 lattice. This interpretation is supported by the fact that the discrepancy grows with the density. This observation also means that while our statistical errors are quite low (with quasiparticle energy error bars within the marker size in our figures) the systematic errors due to finite lattice size may not be so easily dismissed.

Extrapolating to the thermodynamic limit requires simulations at larger lattice sizes, which are beyond the scope of this dissertation. In the meantime, we take the average of the upper and lower branch values as an estimate of the true value of the effective mass. These estimates, labelled as "branch average" in Figs. 4.4 and 4.5, are in agreement with the estimates from Buraczynski *et al.* [39], who performed the first QMC extractions of the effective mass in INM. At low densities, where the large interparticle spacing causes INM to act more like a non-interacting system, the effective mass approaches the bare mass. As we increase the density, the effective mass decreases. These two observations challenge the validity of some Skyrme energy density functionals like SkP and SkM* [15], which have increasing or constant effective masses, and SLy4 [47], which has an effective mass that decays too quickly with increasing density. Comparing Figs. 4.4 and 4.5, we see that the inclusion of three-body forces tends to increase the effective mass.

4.5.2 Self-energy

The self-energy may also be obtained from the linear fit in Eq. (4.13). In the lower left panel of Figs. 4.4 and 4.5, we show the quantity,

$$\frac{U}{\varepsilon_F} \approx \frac{\varepsilon(p)}{\varepsilon_F} - \frac{m}{m^*}\frac{p}{p_F}^2 + \frac{\mu}{\varepsilon_F} \tag{4.14}$$

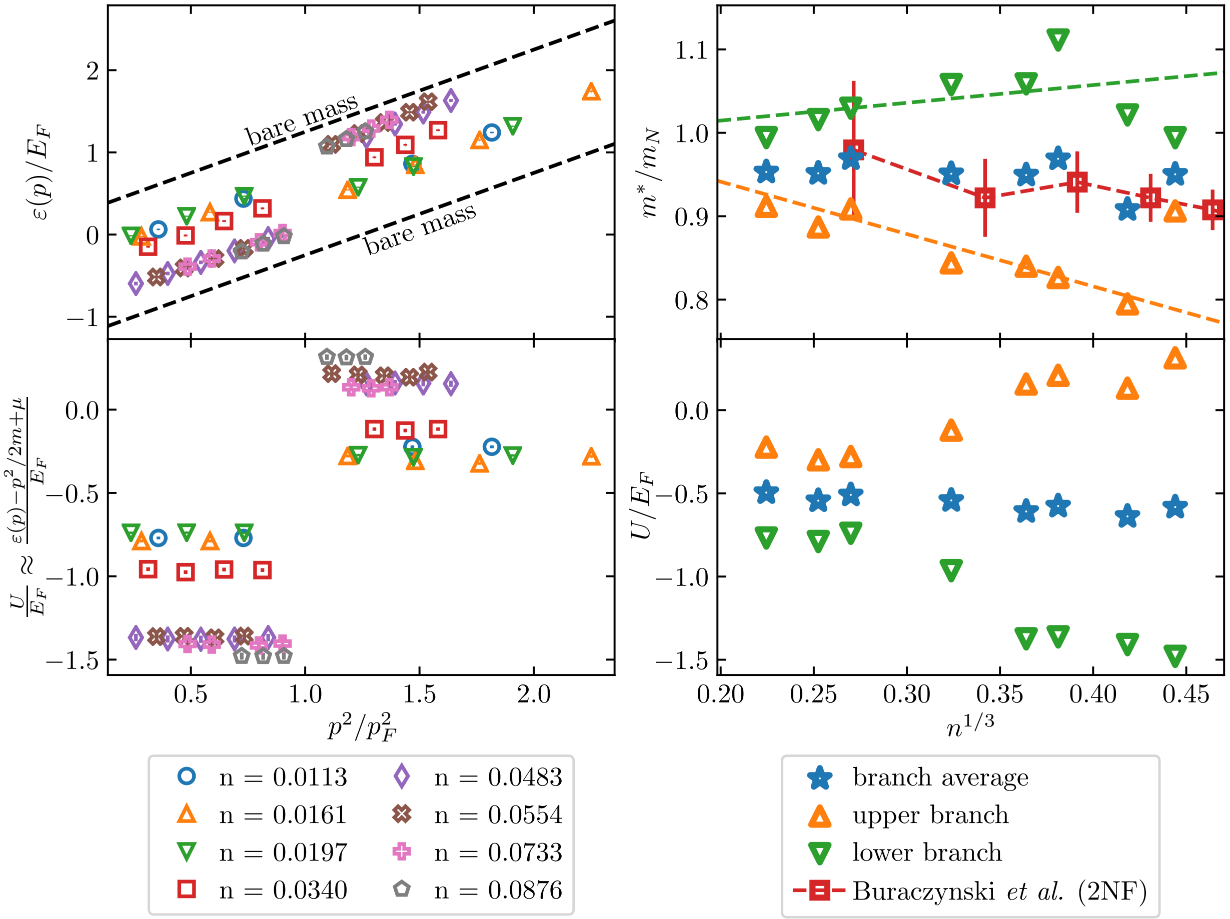

Figure 4.4: (top left) the scaled quasiparticle energy $\varepsilon(p)/\varepsilon_F$ as a function of the scaled squared momentum $(p/p_F)^2$. The bare mass, indicated by the dashed lines, has a slope of one in these units. The lower branch has been multiplied by -1 and shifted up by 1 to ease the comparison with the upper branch. (top right) the effective masses extracted from the linear fit in Eq. (4.13), with separate effective masses extracted for the upper and lower branches alongside the average of the two. We compare our results for the effective mass to those of Buraczynski *et al.* [39] and find good agreement with the branch average results. (bottom left) the self-energy constant as a function of p/p_F, justifying the linear fit in Eq. (4.13). (bottom right) the quasiparticle self-energy, with separate estimates for the upper and lower branch alongside the branch average.

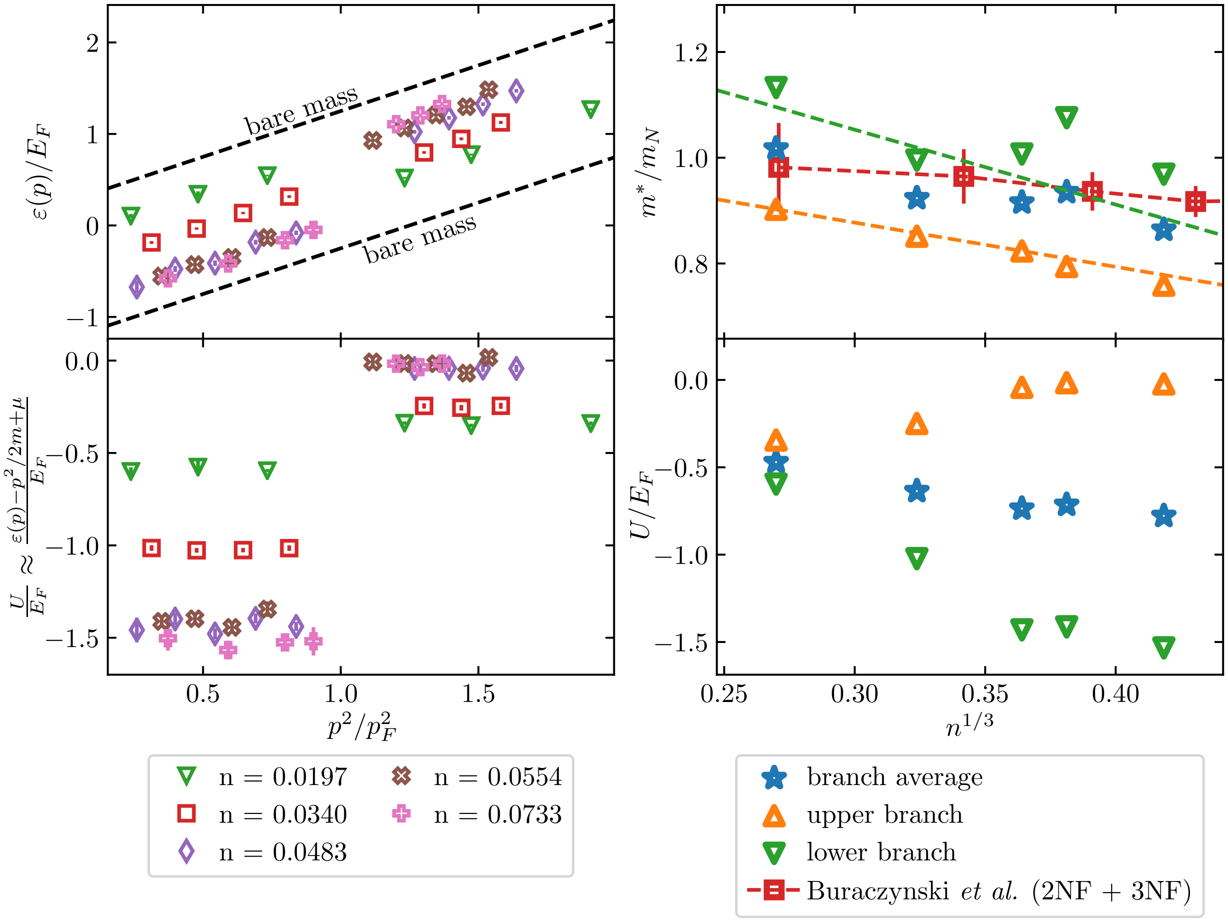

Figure 4.5: Quasiparticle effective mass and self-energy extraction for two- and -three-body forces. See the caption for Fig. 4.4 for further details.

which is independent of the momentum, justifying the linear fit in Eq. (4.13). In the lower right panel, we show our estimates of the self-energy and find the same upper- and lower-branch discrepancy that we found for estimates of the effective mass. We take the branch average to be a rough estimate of the self-energy in the thermodynamic limit and note that it is roughly constant as a function of the density. This mirrors the chemical potential μ that we derived from the energy EoS in Eq. (4.7). To our knowledge, these are the first QMC extractions of the quasiparticle self-energy in INM.

4.5.3 Pairing gap

The superfluid pairing gap is perhaps the most hotly debated and difficult to compute quasiparticle property in neutron matter. Understanding nuclear superfluidity is central to understanding nuclear physics from the range of nuclei to neutron stars [57, 213, 157, 32]. However, the calculation is difficult because it involves large coherence lengths and the detection of small differences in energy by subtracting two large quantities. As such, calculations of the pairing gap have varied widely for the past few decades [57, 133].

Before we present our results for the pairing gap, it is worthwhile to review the role of each quasiparticle parameter on the dispersion relation in Eq. (4.8). The effective mass dictates the slope of the quasiparticle energy far from the Fermi surface. The self-energy and chemical potential dictate the location of the minimum of the quasiparticle energy. The pairing gap Δ has two major effects. First, it sets the value of the excitation gap at its minimum. This is, after all, why we call it a gap. Second, it dictates the curvature of dispersion relation around that minimum. Because the quasiparticle energy is computed from the subtraction of two large numbers, namely the terms in Eq. (4.9), and because the pairing gap is traditionally estimated from the minimum of that difference, it is the quasiparticle parameter that is most sensitive to errors in the energy of the system.

In this study, we use a method of estimating the QPE parameters that is insensitive to global shifts in the quasiparticle energies and separates out the two effects of the pairing gap discussed above. That is, if the calculated quasiparticle energies contain some momentum independent error term, ϵ_2, such that

$$\begin{aligned}\varepsilon(p) &= E(p, N-1) - E_0(N) + \frac{\partial E_0^{(\mathrm{EoS})}(N)}{\partial N} - \frac{1}{2}\frac{\partial^2 E_0^{(\mathrm{EoS})}(N)}{\partial N^2} + \epsilon_2 \qquad (4.15)\\ &= \sqrt{\left(\frac{p^2}{2m^*} - (\mu - U)\right)^2 + \Delta^2} + \epsilon_2, \qquad (4.16)\end{aligned}$$

then, we can estimate the parameters m^*, $\mu - U$, and Δ, while letting the ϵ_2 term absorb any systematic errors that are momentum independent. Thus, we estimate Δ only from the curvature in the quasiparticle dispersion relation around the minimum.

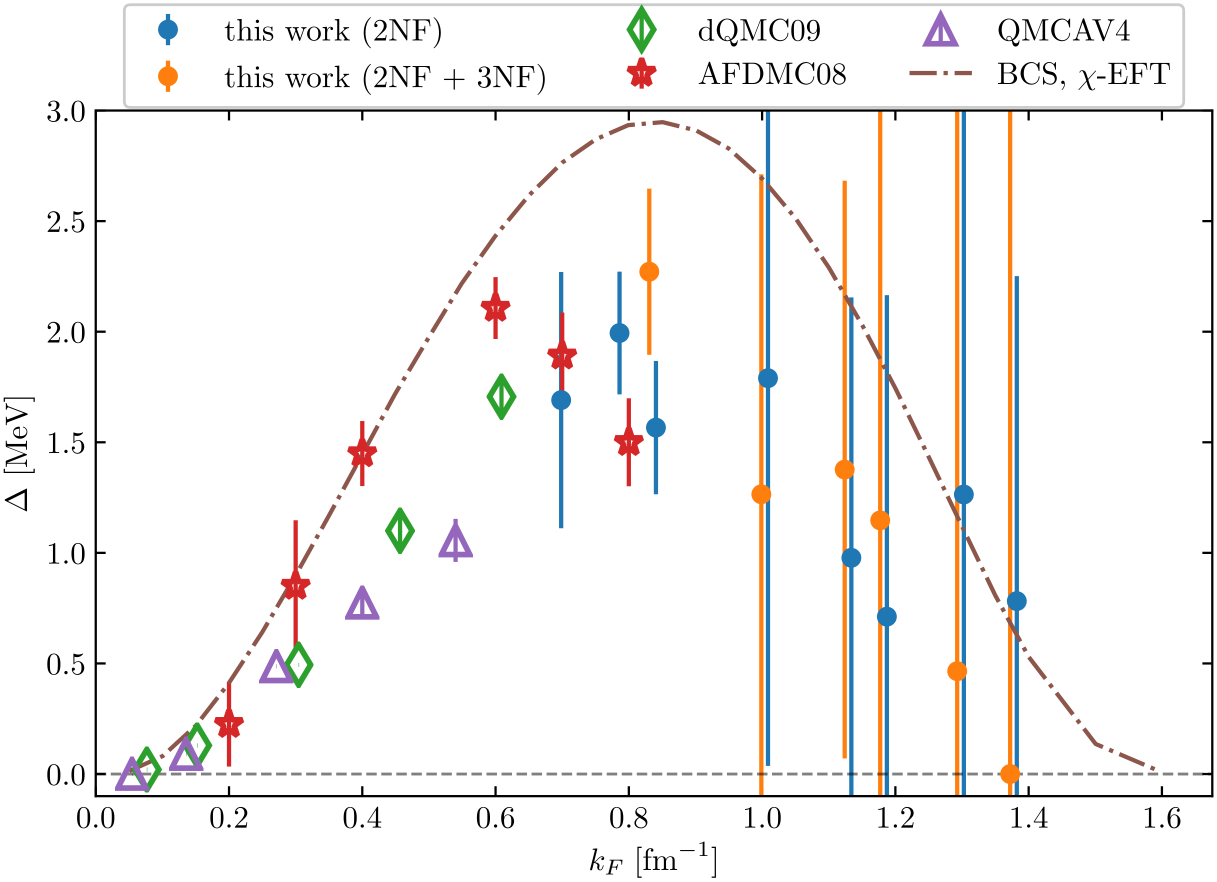

Figure 4.6: Pairing gap in infinite neutron matter using two- and three-body forces. We compare our results at moderate density to the low density results of Gandolfi *et al.* [74] (AFDMC08), Abe and Seki [2] (dQMC09). We also plot the solution to the BCS gap equation using two- and three-body χ-EFT interactions from Drischler *et al.* [58] (dash-dotted line).

The subscript on the parameter ϵ_2 is suggestive, because Eq. (4.16) is exactly the quasiparticle energy in the Lipkin-Nogami pairing model [128, 152, 164, 142], with the substitution $\epsilon_2 \leftrightarrow \lambda_2$. However, in the Lipkin-Nogami model, λ_2 is a number fluctuation constant and the quantity $\Delta + \lambda_2$ is identified with even-odd energy staggering. In our case, ϵ_2 is an error term used to isolate the curvature of the quasiparticle spectrum from global shifts in the energy.

In Fig. 4.6, we show our results for the pairing gap in INM. We show our results alongside low density QMC results from Gandolfi *et al.* [74] (labelled as AFDMC08), Abe and Seki [2] (labelled as dQMC09). We also show BCS results calculated using two- and three-body χ-EFT interactions, which gives us further intuition of the behavior of the gap. However, as valuable as they are, BCS estimates often overestimate the gap because they neglect screening and vertex corrections (see Ref. [77]). The first observation that must be made of our results is that the errors are enormous at higher densities. While the gap averages are in rough qualitative agreement with the BCS gap at high density, the large errors prevent us from drawing conclusions about the density at which the gap disappears or the effect of including three-body forces. At intermediate densities, we predict a pairing gap maximum around $k_F \approx 0.8$ fm^{-1}.

4.6 Summary

In this chapter, we applied the AFQMC methods discussed in Chapter 2 to study infinite neutron matter at zero-temperature. We presented results for the energy equation of state and quasiparticle effective mass. The effective mass estimates confirmed prior results by Buraczynski *et al.* [39] and contradict some Skyrme-based energy density functionals. We also presented the first QMC extraction of the quasiparticle self-energy in INM and showed that it is roughly constant as a function of the density, just as with the chemical potential. Lastly, we presented results for the pairing gap in INM and, despite large errors, proposed a pairing gap maximum at $k_F \approx 0.8$ fm^{-1}.

Chapter 5

CONCLUSIONS AND FUTURE WORK

5.1 Conclusions

In this thesis, we have conducted quantum Monte Carlo studies of the BCS–BEC crossover at finite temperature and of pure neutron matter at zero temperature. We showed that with an appropriate choice of basis, the same AFQMC technique is suitable to study both zero-temperature and finite-temperature systems.

In the case of the BCS–BEC crossover, we introduced a new ensemble, the particle asymmetry constrained ensemble, and used it alongside the grand canonical and canonical ensembles to compute the energy, spin susceptibility, condensate fraction, critical temperature, pairing gap, and Tan contact around the unitary regime. Ours are the first calculations of the Tan contact and spin susceptibility away from unitarity. We used these results to argue for the existence of a pseudogap at unitarity.

In the case of neutron matter, we computed the quasiparticle effective mass, self-energy, and pairing gap. These quantities are crucial to matching Landau's Fermi liquid theory to ab-initio results for neutron matter, and eventually nuclear matter. We found that the effective mass ratio approaches one for low density neutron matter and decreases as we increase the density, confirming earlier ab-initio results and excluding some Skyrme energy density functions. We also reported the first QMC extractions of the self-energy and showed that it was roughly constant as a function of density. Finally, we calculated the pairing gap in INM and proposed a pairing gap maximum at $k_F \approx 0.8\ \mathrm{fm}^{-1}$.

5.2 *Future work*

Much work remains to be done on both the BCS–BEC crossover and pure neutron matter, let alone nuclear matter and nuclei. Most of the work (including mine) on the BCS–BEC crossover has focused on systems with equal mixtures of two spin states[1]. Just as the possibility of pseudogap phenomena discussed in Chapter 3 suggests a link between the BCS–BEC crossover and high-T_c superconductivity [50], the polarized phases in the crossover may hold connections to magnetized superconductivity. Several exotic phases have been suggested to simultaneously maintain both pairing and spin imbalance [176, 129, 179], including the crystalline supersolid Larkin-Ovchinnikov Fulde-Ferrel (LOFF) state [73, 121]. But simulating polarized phases can be difficult because they suffer from the aforementioned sign problem. The PACE provides some hope for modelling asymmetric Fermi gases but it is not yet clear how high the polarization can go before the PACE calculations become impractical. And care must be taken when comparing fluctuations derived from PACE calculations with those in the GCE or canonical ensemble, as discussed in Appendix B.

In the case of neutron matter, we asserted that the discrepancy between the upper and lower branch estimates is due to finite size effects and would disappear in the thermodynamic limit. Future work should seek to verify this claim by simulating on larger lattices and extrapolating to the thermodynamic limit. Furthermore, the large errors in our estimates of the pairing gap must be reduced. This will require more Monte Carlo samples to reduce sampling error and simulation on larger lattices to better understand the extrapolation to the thermodynamic limit. After this issue is resolved, we should move on to simulating symmetric nuclear matter and eventually nuclei.

---

[1] These two "spin" states may well be two hyperfine states in experimental realizations, but we use the language of two spin-1/2 states in this work.

BIBLIOGRAPHY

[1] *Landau Fermi-Liquid Theory.* John Wiley & Sons, Ltd, 2007.

[2] T. Abe and R. Seki. Lattice calculation of thermal properties of low-density neutron matter with pionless *NN* effective field theory. *Phys. Rev. C*, 79:054002, May 2009.

[3] AA Abrikosov and LP Gor'Kov. On the problem of the knight shift in superconductors. *Soviet Physics JETP*, 12(2):337–339, 1961.

[4] Y. Alhassid, D. J. Dean, S. E. Koonin, G. Lang, and W. E. Ormand. Practical solution to the Monte Carlo sign problem: Realistic calculations of ^{54}Fe. *Phys. Rev. Lett.*, 72:613–616, Jan 1994.

[5] Michael P. Allen and Dominic J. Tildesley. *Computer Simulation of Liquids: Second Edition.* Oxford University Press, 2017.

[6] H. Alloul, T. Ohno, and P. Mendels. ^{89}Y nmr evidence for a fermi-liquid behavior in $\mathrm{yba_2cu_3o_{6+x}}$. *Phys. Rev. Lett.*, 63:1700–1703, Oct 1989.

[7] M. H. Anderson, J. R. Ensher, M. R. Matthews, C. E. Wieman, and E. A. Cornell. Observation of bose-einstein condensation in a dilute atomic vapor. *Science*, 269(5221):198–201, 1995.

[8] Peter Arnold and Guy Moore. Bec transition temperature of a dilute homogeneous imperfect bose gas. *Phys. Rev. Lett.*, 87:120401, Aug 2001.

[9] G. E. Astrakharchik, J. Boronat, J. Casulleras, and S. Giorgini. Equation of State of a Fermi Gas in the BEC-BCS Crossover: A Quantum Monte Carlo Study. *Phys. Rev. Lett.*, 93:200404, Nov 2004.

[10] G. E. Astrakharchik, J. Boronat, J. Casulleras, and S. Giorgini. Momentum Distribution and Condensate Fraction of a Fermion Gas in the BCS–BEC Crossover. *Phys. Rev. Lett.*, 95:230405, Dec 2005.

[11] George A. Baker. Neutron matter model. *Phys. Rev. C*, 60:054311, Oct 1999.

[12] M N Barber. Finite-size scaling in phase transitions and critical phenomena. In C Domb and JL Lebowitz, editors, *Phase Transitions and Critical Phenomena*, volume 8, page 146. Academic Press, 1983.

[13] J. Bardeen, L. N. Cooper, and J. R. Schrieffer. Microscopic theory of superconductivity. *Phys. Rev.*, 106:162–164, Apr 1957.

[14] J. Bardeen, L. N. Cooper, and J. R. Schrieffer. Theory of superconductivity. *Phys. Rev.*, 108:1175–1204, Dec 1957.

[15] J. Bartel, P. Quentin, M. Brack, C. Guet, and H.-B. Håkansson. Towards a better parametrisation of Skyrme-like effective forces: A critical study of the SkM force. *Nuclear Physics A*, 386(1):79–100, 1982.

[16] Gordon Baym, Jean-Paul Blaizot, Markus Holzmann, Franck Laloë, and Dominique Vautherin. The transition temperature of the dilute interacting bose gas. *Phys. Rev. Lett.*, 83:1703–1706, Aug 1999.

[17] M. Bender, K. Rutz, P. G. Reinhard, and J. A. Maruhn. Pairing gaps from nuclear mean field models. *Eur. Phys. J.*, A8:59–75, 2000.

[18] Casey E. Berger, Lukas Rammelmüller, Andrew C. Loheac, Florian Ehmann, Jens Braun, and Joaquín E. Drut. Complex Langevin and other approaches to the sign problem in quantum many-body physics, 2019.

[19] G. F. Bertsch. Preface. *International Journal of Modern Physics B*, 15(06n07):iii–iii, 2001.

[20] George F Bertsch. The Many-Body Challenge Problem (MBX) formulated by G. F. Bertsch in 1999.

[21] G Bighin, G Mazzarella, L Dell'Anna, and L Salasnich. Pair condensation of polarized fermions in the BCS–BEC crossover. *Journal of Physics B: Atomic, Molecular and Optical Physics*, 47(19):195302, Sep 2014.

[22] Immanuel Bloch, Jean Dalibard, and Wilhelm Zwerger. Many-body physics with ultracold gases. *Rev. Mod. Phys.*, 80:885–964, Jul 2008.

[23] Immanuel Bloch, Jean Dalibard, and Wilhelm Zwerger. Many-body physics with ultracold gases. *Rev. Mod. Phys.*, 80:885–964, Jul 2008.

[24] N Bogoliubov. On the theory of superfluidity. *J. Phys*, 11(1):23, 1947.

[25] NN Bogoliubov. Zetf 34 (1958) 65. *Sov. Phys.-JETP*, 34:41, 1958.

[26] Aage Bohr and Ben R Mottelson. *Nuclear Structure*, volume 1. World Scientific Publishing Company, 1998.

[27] Satyendra Nath Bose. Planck's law and light quantum hypothesis. *Z. phys*, 26(1):178, 1924.

[28] Eric Braaten. Universal Relations for Fermions with Large Scattering Length. In Wilhelm Zwerger, editor, *The BCS–BEC Crossover and the Unitary Fermi Gas*, pages 193–231. Springer Berlin Heidelberg, Berlin, Heidelberg, 2012.

[29] Jens Braun, Jiunn-Wei Chen, Jian Deng, Joaquín E. Drut, Bengt Friman, Chen-Te Ma, and Yu-Dai Tsai. Imaginary Polarization as a Way to Surmount the Sign Problem in Ab Initio Calculations of Spin-Imbalanced Fermi Gases. *Phys. Rev. Lett.*, 110:130404, Mar 2013.

[30] Jens Braun, Joaquín E. Drut, and Dietrich Roscher. Zero-Temperature Equation of State of Mass-Imbalanced Resonant Fermi Gases. *Phys. Rev. Lett.*, 114:050404, Feb 2015.

[31] J. G. Briano and E. D. Glandt. Statistical thermodynamics of polydisperse fluids. *The Journal of Chemical Physics*, 80(7):3336–3343, 1984.

[32] David M. Brink and Ricardo A. Broglia. *Nuclear Superfluidity: Pairing in Finite Systems*. Cambridge Monographs on Particle Physics, Nuclear Physics and Cosmology. Cambridge University Press, 2005.

[33] Aurel Bulgac. Projection of good quantum numbers for reaction fragments. *Phys. Rev. C*, 100:034612, Sep 2019.

[34] Aurel Bulgac and George F Bertsch. Collective oscillations of a trapped fermi gas near the unitary limit. *Physical review letters*, 94(7):070401, 2005.

[35] Aurel Bulgac, Joaquín E. Drut, and Piotr Magierski. Quantum Monte Carlo simulations of the BCS–BEC crossover at finite temperature. *Phys. Rev. A*, 78:023625, Aug 2008.

[36] Aurel Bulgac and Michael McNeil Forbes. Zero-temperature thermodynamics of asymmetric Fermi gases at unitarity. *Phys. Rev. A*, 75:031605, Mar 2007.

[37] Aurel Bulgac, Michael McNeil Forbes, Shi Jin, Rodrigo Navarro Perez, and Nicolas Schunck. Minimal nuclear energy density functional. *Phys. Rev. C*, 97:044313, Apr 2018.

[38] Aurel Bulgac, Michael McNeil Forbes, and Piotr Magierski. The Unitary Fermi Gas: From Monte Carlo to Density Functionals. In Wilhelm Zwerger, editor, *The BCS–BEC Crossover and the Unitary Fermi Gas*, pages 305–373. Springer Berlin Heidelberg, Berlin, Heidelberg, 2012.

[39] Mateusz Buraczynski, Nawar Ismail, and Alexandros Gezerlis. Neutron matter at the interface(s). *The European Physical Journal A*, 56:112, Apr 2020.

[40] C.P. Burgess. An Introduction to Effective Field Theory. *Annual Review of Nuclear and Particle Science*, 57(1):329–362, 2007.

[41] Evgeni Burovski, Evgeny Kozik, Nikolay Prokof'ev, Boris Svistunov, and Matthias Troyer. Critical Temperature Curve in BEC–BCS Crossover. *Phys. Rev. Lett.*, 101:090402, Aug 2008.

[42] C. Carcy, S. Hoinka, M. G. Lingham, P. Dyke, C. C. N. Kuhn, H. Hu, and C. J. Vale. Contact and Sum Rules in a Near-Uniform Fermi Gas at Unitarity. *Phys. Rev. Lett.*, 122:203401, May 2019.

[43] J. Carlson, S.-Y. Chang, V. R. Pandharipande, and K. E. Schmidt. Superfluid Fermi Gases with Large Scattering Length. *Phys. Rev. Lett.*, 91:050401, Jul 2003.

[44] J. Carlson, Stefano Gandolfi, Kevin E. Schmidt, and Shiwei Zhang. Auxiliary-field quantum Monte Carlo method for strongly paired fermions. *Phys. Rev. A*, 84:061602, Dec 2011.

[45] J. Carlson and Sanjay Reddy. Superfluid Pairing Gap in Strong Coupling. *Phys. Rev. Lett.*, 100:150403, Apr 2008.

[46] Yvan Castin. Basic theory tools for degenerate fermi gases, 2006.

[47] E. Chabanat, P. Bonche, P. Haensel, J. Meyer, and R. Schaeffer. A Skyrme parametrization from subnuclear to neutron star densities. *Nuclear Physics A*, 627(4):710–746, 1997.

[48] S. Y. Chang. Equation of state and phases of a polarized unitary Fermi gas. *Phys. Rev. A*, 77:051602, May 2008.

[49] S. Y. Chang, V. R. Pandharipande, J. Carlson, and K. E. Schmidt. Quantum Monte Carlo studies of superfluid Fermi gases. *Phys. Rev. A*, 70:043602, Oct 2004.

[50] Qijin Chen, Jelena Stajic, Shina Tan, and K. Levin. BCS–BEC crossover: From high temperature superconductors to ultracold superfluids. *Physics Reports*, 412(1):1–88, 2005.

[51] Qijin Chen and Jibiao Wang. Pseudogap phenomena in ultracold atomic Fermi gases. *Frontiers of Physics*, 9(5):539–570, 2014.

[52] Frédéric Chevy and Christophe Mora. Ultra-cold polarized Fermi gases. *Reports on Progress in Physics*, 73(11):112401, oct 2010.

[53] Chih-Chun Chien, Hao Guo, Yan He, and K. Levin. Comparative study of bcs-bec crossover theories above T_c: The nature of the pseudogap in ultracold atomic fermi gases. *Phys. Rev. A*, 81:023622, Feb 2010.

[54] Cheng Chin, Rudolf Grimm, Paul Julienne, and Eite Tiesinga. Feshbach resonances in ultracold gases. *Rev. Mod. Phys.*, 82:1225–1286, Apr 2010.

[55] Cheng Chin, Rudolf Grimm, Paul Julienne, and Eite Tiesinga. Feshbach resonances in ultracold gases. *Rev. Mod. Phys.*, 82:1225–1286, Apr 2010.

[56] Georges-Louis Leclerc Comte de Buffon and Imprimerie Royale. *Histoire naturelle, générale et particulière, contenant les epoques de la nature.* de l'Imprimerie Royale, 1778.

[57] D. J. Dean and M. Hjorth-Jensen. Pairing in nuclear systems: from neutron stars to finite nuclei. *Rev. Mod. Phys.*, 75:607–656, Apr 2003.

[58] C. Drischler, T. Krüger, K. Hebeler, and A. Schwenk. Pairing in neutron matter: New uncertainty estimates and three-body forces. *Phys. Rev. C*, 95:024302, Feb 2017.

[59] Joaquín E. Drut. Improved lattice operators for nonrelativistic fermions. *Phys. Rev. A*, 86:013604, Jul 2012.

[60] Joaquín E. Drut, Timo A. Lähde, Gabriel Wlazłowski, and Piotr Magierski. Equation of state of the unitary Fermi gas: An update on lattice calculations. *Phys. Rev. A*, 85:051601, May 2012.

[61] T. Duguet, P. Bonche, P.-H. Heenen, and J. Meyer. Pairing correlations. II. Microscopic analysis of odd-even mass staggering in nuclei. *Phys. Rev. C*, 65:014311, Dec 2001.

[62] David Duvenaud. *Automatic model construction with Gaussian processes.* PhD thesis, University of Cambridge, 11 2014.

[63] D. M. Eagles. Possible pairing without superconductivity at low carrier concentrations in bulk and thin-film superconducting semiconductors. *Phys. Rev.*, 186:456–463, Oct 1969.

[64] B. Efron. Bootstrap Methods: Another Look at the Jackknife. *Ann. Statist.*, 7(1):1–26, 01 1979.

[65] Albert Einstein. Quantum theory of the monatomic ideal gas. *Sitzungsberichte der Preussischen Akademie der Wissenschaften, Physikalisch-mathematische Klasse*, pages 261–267, 1924.

[66] A. Ekström, G. Baardsen, C. Forssén, G. Hagen, M. Hjorth-Jensen, G. R. Jansen, R. Machleidt, W. Nazarewicz, T. Papenbrock, J. Sarich, and S. M. Wild. Optimized Chiral Nucleon-Nucleon Interaction at Next-to-Next-to-Leading Order. *Phys. Rev. Lett.*, 110:192502, May 2013.

[67] Michael G. Endres, David B. Kaplan, Jong-Wan Lee, and Amy N. Nicholson. Lattice monte carlo calculations for unitary fermions in a finite box. *Phys. Rev. A*, 87:023615, Feb 2013.

[68] Tilman Enss and Rudolf Haussmann. Quantum Mechanical Limitations to Spin Diffusion in the Unitary Fermi Gas. *Phys. Rev. Lett.*, 109:195303, Nov 2012.

[69] E. Epelbaum, W. Glöckle, and U.-G. Meißner. Improving the convergence of the chiral expansion for nuclear forces – I; Peripheral phases. *The European Physical Journal A – Hadrons and Nuclei*, 19(1):125–137, 2004.

[70] Alan M Ferrenberg and Robert H Swendsen. New monte carlo technique for studying phase transitions. *Physical review letters*, 61(23):2635, 1988.

[71] Herman Feshbach. Unified theory of nuclear reactions. *Annals of Physics*, 5(4):357–390, 1958.

[72] R. Franz and G. Wiedemann. Ueber die Wärme-Leitungsfähigkeit der Metalle. *Annalen der Physik*, 165(8):497–531, 1853.

[73] Peter Fulde and Richard A. Ferrell. Superconductivity in a Strong Spin-Exchange Field. *Phys. Rev.*, 135:A550–A563, Aug 1964.

[74] S. Gandolfi, A. Yu. Illarionov, S. Fantoni, F. Pederiva, and K. E. Schmidt. Equation of State of Superfluid Neutron Matter and the Calculation of the ${}^1S_0$ Pairing Gap. *Phys. Rev. Lett.*, 101:132501, Sep 2008.

[75] Stefano Gandolfi, Alexandros Gezerlis, and J. Carlson. Neutron Matter from Low to High Density. *Annual Review of Nuclear and Particle Science*, 65(1):303–328, 2015.

[76] Andrew Gelman and Donald B. Rubin. Inference from Iterative Simulation Using Multiple Sequences. *Statist. Sci.*, 7(4):457–472, 11 1992.

[77] A. Gezerlis, C. J. Pethick, and A. Schwenk. Pairing and superfluidity of nucleons in neutron stars. In Karl-Heinz Bennemann and John B. Ketterson, editors, *Novel Superfluids.* Oxford University Press, Oxford, 2014.

[78] A. Gezerlis, I. Tews, E. Epelbaum, M. Freunek, S. Gandolfi, K. Hebeler, A. Nogga, and A. Schwenk. Local chiral effective field theory interactions and quantum Monte Carlo applications. *Phys. Rev. C*, 90:054323, Nov 2014.

[79] A. Gezerlis, I. Tews, E. Epelbaum, S. Gandolfi, K. Hebeler, A. Nogga, and A. Schwenk. Quantum Monte Carlo Calculations with Chiral Effective Field Theory Interactions. *Phys. Rev. Lett.*, 111:032501, Jul 2013.

[80] C. N. Gilbreth and Y. Alhassid. Pair condensation in a finite trapped Fermi gas. *Phys. Rev. A*, 88:063643, Dec 2013.

[81] C.N. Gilbreth and Y. Alhassid. Stabilizing canonical-ensemble calculations in the auxiliary-field Monte Carlo method. *Computer Physics Communications*, 188:1 – 6, 2015.

[82] Stefano Giorgini, Lev P. Pitaevskii, and Sandro Stringari. Theory of ultracold atomic Fermi gases. *Rev. Mod. Phys.*, 80:1215–1274, Oct 2008.

[83] Stefano Giorgini, Lev P. Pitaevskii, and Sandro Stringari. Theory of ultracold atomic Fermi gases. *Rev. Mod. Phys.*, 80:1215–1274, Oct 2008.

[84] Robert FA Goedhart. *The never ending dispute: delimitation of air space and outer space*, volume 4. Editions Frontieres, 1996.

[85] D. E. Gonzalez Trotter, F. Salinas Meneses, W. Tornow, C. R. Howell, Q. Chen, A. S. Crowell, C. D. Roper, R. L. Walter, D. Schmidt, H. Witała, W. Glöckle, H. Tang, Z. Zhou, and I. Šlaus. Neutron-deuteron breakup experiment at $E_n = 13$ MeV: Determination of the ${}^1S_0$ neutron-neutron scattering length a_{nn}. *Phys. Rev. C*, 73:034001, Mar 2006.

[86] D. E. González Trotter, F. Salinas, Q. Chen, A. S. Crowell, W. Glöckle, C. R. Howell, C. D. Roper, D. Schmidt, I. Šlaus, H. Tang, W. Tornow, R. L. Walter, H. Witała, and

Z. Zhou. New Measurement of the $^1S_0$ Neutron-Neutron Scattering Length Using the Neutron-Proton Scattering Length as a Standard. *Phys. Rev. Lett.*, 83:3788–3791, Nov 1999.

[87] LP Gor'kov and TK Melik-Barkhudarov. Contribution to the theory of superfluidity in an imperfect fermi gas. *Sov. Phys. JETP*, 13(5):1018, 1961.

[88] Markus Greiner, Cindy A. Regal, and Deborah S. Jin. Emergence of a molecular Bose-Einstein condensate from a Fermi gas. *Nature*, 426:537–540, Dec 2003.

[89] X.-W. Guan, X.-G. Yin, A. Foerster, M. T. Batchelor, C.-H. Lee, and H.-Q. Lin. Wilson Ratio of Fermi Gases in One Dimension. *Phys. Rev. Lett.*, 111:130401, Sep 2013.

[90] K.B. Gubbels and H.T.C. Stoof. Imbalanced Fermi gases at unitarity. *Physics Reports*, 525(4):255–313, 2013.

[91] Richard Hamming. *Numerical methods for scientists and engineers.* Courier Corporation, 2012.

[92] Trevor Hastie, Robert Tibshirani, and Jerome Friedman. *Model Assessment and Selection*, pages 219–259. Springer New York, New York, NY, 2009.

[93] W. K. Hastings. Monte Carlo sampling methods using Markov chains and their applications. *Biometrika*, 57(1):97–109, 04 1970.

[94] Rongzheng He, Ning Li, Bing-Nan Lu, and Dean Lee. Superfluid Condensate Fraction and Pairing Wave Function of the Unitary Fermi Gas, 2019.

[95] K. Hebeler and A. Schwenk. Chiral three-nucleon forces and neutron matter. *Phys. Rev. C*, 82:014314, Jul 2010.

[96] J. E. Hirsch. Discrete Hubbard-Stratonovich transformation for fermion lattice models. *Phys. Rev. B*, 28:4059–4061, Oct 1983.

[97] Tin-Lun Ho. Universal thermodynamics of degenerate quantum gases in the unitarity limit. *Phys. Rev. Lett.*, 92:090402, Mar 2004.

[98] Sascha Hoinka, Paul Dyke, Marcus G. Lingham, Jami J. Kinnunen, Georg M. Bruun, and Chris J. Vale. Goldstone mode and pair-breaking excitations in atomic Fermi superfluids. *Nature Physics*, 13(10):943–946, 2017.

[99] C.R Howell, Q Chen, T.S Carman, A Hussein, W.R Gibbs, B.F Gibson, G Mertens, C.F Moore, C Morris, A Obst, E Pasyuk, C.D Roper, F Salinas, I Slaus, S Sterbenz, W Tornow, R.L Walter, C.R Whiteley, and M Whitton. Toward a resolution of the neutron-neutron scattering-length issue. *Physics Letters B*, 444(3):252–259, 1998.

[100] Hui Hu, Xia-Ji Liu, and Peter D. Drummond. Comparative study of strong-coupling theories of a trapped fermi gas at unitarity. *Phys. Rev. A*, 77:061605, Jun 2008.

[101] Hui Hu, Xia-Ji Liu, and Peter D Drummond. Universal thermodynamics of a strongly interacting fermi gas: theory versus experiment. *New Journal of Physics*, 12(6):063038, jun 2010.

[102] Hui Hu, Xia-Ji Liu, Peter D. Drummond, and Hui Dong. Pseudogap pairing in ultracold fermi atoms. *Phys. Rev. Lett.*, 104:240407, Jun 2010.

[103] J. Hubbard. Calculation of Partition Functions. *Phys. Rev. Lett.*, 3:77–78, Jul 1959.

[104] S. Jensen, C. N. Gilbreth, and Y. Alhassid. Pairing correlations across the superfluid phase transition in the unitary fermi gas, 2018.

[105] S. Jensen, C. N. Gilbreth, and Y. Alhassid. The contact in the unitary Fermi gas across the superfluid phase transition, 2019.

[106] S. Jensen, C. N. Gilbreth, and Y. Alhassid. Pairing Correlations across the Superfluid Phase Transition in the Unitary Fermi Gas. *Phys. Rev. Lett.*, 124:090604, Mar 2020.

[107] S Jensen, CN Gilbreth, and Y Alhassid. The pseudogap regime in the unitary Fermi gas. *The European Physical Journal Special Topics*, 227:2241, 2019.

[108] David B. Kaplan. Five lectures on effective field theory, 2005.

[109] Takashi Kashimura, Ryota Watanabe, and Yoji Ohashi. Spin susceptibility and fluctuation corrections in the BCS-BEC crossover regime of an ultracold Fermi gas. *Phys. Rev. A*, 86:043622, Oct 2012.

[110] V. A. Kashurnikov, N. V. Prokof'ev, and B. V. Svistunov. Critical temperature shift in weakly interacting bose gas. *Phys. Rev. Lett.*, 87:120402, Aug 2001.

[111] T. D. Kieu and C. J. Griffin. Monte carlo simulations with indefinite and complex-valued measures. *Phys. Rev. E*, 49:3855–3859, May 1994.

[112] Charles Kittel and Herbert Kroemer. Thermal physics, 1998.

[113] David A. Kofke and Eduardo D. Glandt. Monte Carlo simulation of multicomponent equilibria in a semigrand canonical ensemble. *Molecular Physics*, 64(6):1105–1131, 1988.

[114] Mark J. H. Ku, Ariel T. Sommer, Lawrence W. Cheuk, and Martin W. Zwierlein. Revealing the Superfluid Lambda Transition in the Universal Thermodynamics of a Unitary Fermi Gas. *Science*, 335(6068):563–567, 2012.

[115] David P Landau and Kurt Binder. *A guide to Monte Carlo simulations in statistical physics*. Cambridge university press, 2014.

[116] Lev Davidovich Landau and Evgeny Mikhailovich Lifshitz. *Quantum Mechanics: Non-relativistic Theory. Course of Theoretical Physics*, volume 3. Pergamon Press, 1958.

[117] Lev Davidovich Landau and Evgeny Mikhailovich Lifshitz. *Fluid Mechanics. Course of Theoretical Physics*, volume 6. Pergamon Press, 1987.

[118] Lev Davidovich Landau, Evgeny Mikhailovich Lifshitz, and Lev Petrovich Pitaevskii. *Statistical Physics: Part I. Course of Theoretical Physics*, volume 5. Pergamon Press, 1980.

[119] G. H. Lang, C. W. Johnson, S. E. Koonin, and W. E. Ormand. Monte Carlo evaluation of path integrals for the nuclear shell model. *Phys. Rev. C*, 48:1518–1545, Oct 1993.

[120] K. Langanke, D. J. Dean, P. B. Radha, Y. Alhassid, and S. E. Koonin. Shell-model Monte Carlo studies of *fp*-shell nuclei. *Phys. Rev. C*, 52:718–725, Aug 1995.

[121] AI Larkin and Yu N Ovchinnikov. Nonuniform state of superconductors. *Soviet Physics-JETP*, 20(3):762–762, 1965.

[122] J. L. Lebowitz, J. K. Percus, and L. Verlet. Ensemble Dependence of Fluctuations with Application to Machine Computations. *Phys. Rev.*, 153:250–254, Jan 1967.

[123] Patrick A Lee. From high temperature superconductivity to quantum spin liquid: progress in strong correlation physics. *Reports on Progress in Physics*, 71(1):012501, dec 2007.

[124] Patrick A. Lee, Naoto Nagaosa, and Xiao-Gang Wen. Doping a mott insulator: Physics of high-temperature superconductivity. *Rev. Mod. Phys.*, 78:17–85, Jan 2006.

[125] A. J. Leggett. Cooper pairing in spin-polarized Fermi systems. *J. Phys. Colloques*, 41(C7):C7–19–C7–26, 1980.

[126] AJ Leggett. Modern trends in the theory of condensed matter. *Modern Trends in the Theory of Condensed Matter, Proc. XVI Karpacz Winter School of Theoretical Physics, 1980*, 1980.

[127] Kathryn Levin, Qijin Chen, Chih-Chun Chien, and Yan He. Comparison of different pairing fluctuation approaches to bcs–bec crossover. *Annals of Physics*, 325(2):233 – 264, 2010.

[128] Harry J Lipkin. Collective motion in many-particle systems: Part 1. The violation of conservation laws. *Annals of Physics*, 9(2):272–291, 1960.

[129] W. Vincent Liu and Frank Wilczek. Interior Gap Superfluidity. *Phys. Rev. Lett.*, 90:047002, Jan 2003.

[130] C. Lobo, A. Recati, S. Giorgini, and S. Stringari. Normal State of a Polarized Fermi Gas at Unitarity. *Phys. Rev. Lett.*, 97:200403, Nov 2006.

[131] Andrew C. Loheac, Jens Braun, and Joaquín E. Drut. Polarized fermions in one dimension: Density and polarization from complex Langevin calculations, perturbation theory, and the virial expansion. *Phys. Rev. D*, 98:054507, Sep 2018.

[132] Andrew C. Loheac, Jens Braun, Joaquín E. Drut, and Dietrich Roscher. Thermal equation of state of polarized fermions in one dimension via complex chemical potentials. *Phys. Rev. A*, 92:063609, Dec 2015.

[133] Umberto Lombardo and Hans-Josef Schulze. *Superfluidity in Neutron Star Matter*, pages 30–53. Springer Berlin Heidelberg, Berlin, Heidelberg, 2001.

[134] Per-Olov Löwdin. Quantum Theory of Many-Particle Systems. I. Physical Interpretations by Means of Density Matrices, Natural Spin-Orbitals, and Convergence Problems in the Method of Configurational Interaction. *Phys. Rev.*, 97:1474–1489, Mar 1955.

[135] R. Machleidt and D.R. Entem. Chiral effective field theory and nuclear forces. *Physics Reports*, 503(1):1–75, 2011.

[136] David G. Madland and J.Rayford Nix. New model of the average neutron and proton pairing gaps. *Nuclear Physics A*, 476(1):1–38, 1988.

[137] Piotr Magierski, Gabriel Wlazłowski, and Aurel Bulgac. Onset of a Pseudogap Regime in Ultracold Fermi Gases. *Phys. Rev. Lett.*, 107:145304, Sep 2011.

[138] Piotr Magierski, Gabriel Wlazłowski, Aurel Bulgac, and Joaquín E. Drut. Finite-Temperature Pairing Gap of a Unitary Fermi Gas by Quantum Monte Carlo Calculations. *Phys. Rev. Lett.*, 103:210403, Nov 2009.

[139] Jonathan C. McDowell. The edge of space: Revisiting the Karman Line. *Acta Astronautica*, 151:668–677, 2018.

[140] Nicholas Metropolis et al. The beginning of the monte carlo method. *Los Alamos Science*, 15(584):125–130, 1987.

[141] Nicholas Metropolis, Arianna W. Rosenbluth, Marshall N. Rosenbluth, Augusta H. Teller, and Edward Teller. Equation of State Calculations by Fast Computing Machines. *The Journal of Chemical Physics*, 21(6):1087–1092, 1953.

[142] P. Möller and J.R. Nix. Nuclear pairing models. *Nuclear Physics A*, 536(1):20–60, 1992.

[143] Christophe Mora and Yvan Castin. Extension of Bogoliubov theory to quasicondensates. *Phys. Rev. A*, 67:053615, May 2003.

[144] Erich J Mueller. Review of pseudogaps in strongly interacting Fermi gases. *Reports on Progress in Physics*, 80(10):104401, sep 2017.

[145] Biswaroop Mukherjee, Parth B. Patel, Zhenjie Yan, Richard J. Fletcher, Julian Struck, and Martin W. Zwierlein. Spectral Response and Contact of the Unitary Fermi Gas. *Phys. Rev. Lett.*, 122:203402, May 2019.

[146] Léo Neufcourt, Yuchen Cao, Samuel Giuliani, Witold Nazarewicz, Erik Olsen, and Oleg B. Tarasov. Beyond the proton drip line: Bayesian analysis of proton-emitting nuclei. *Phys. Rev. C*, 101:014319, Jan 2020.

[147] Léo Neufcourt, Yuchen Cao, Samuel A. Giuliani, Witold Nazarewicz, Erik Olsen, and Oleg B. Tarasov. Quantified limits of the nuclear landscape, 2020.

[148] Léo Neufcourt, Yuchen Cao, Witold Nazarewicz, and Frederi Viens. Bayesian approach to model-based extrapolation of nuclear observables. *Phys. Rev. C*, 98:034318, Sep 2018.

[149] M Newman and G Barkema. *Monte carlo methods in statistical physics.* Oxford University Press: New York, USA, 1999.

[150] M Peter Nightingale and Cyrus J Umrigar. *Quantum Monte Carlo methods in physics and chemistry.* Springer Science & Business Media, 1998.

[151] K. Ninios, Tao Hong, T. Manabe, C. Hotta, S. N. Herringer, M. M. Turnbull, C. P. Landee, Y. Takano, and H. B. Chan. Wilson Ratio of a Tomonaga-Luttinger Liquid in a Spin-1/2 Heisenberg Ladder. *Phys. Rev. Lett.*, 108:097201, Feb 2012.

[152] Yukihisa Nogami. On Lipkin's Treatment of Pairing Forces in Nuclei. *Progress of Theoretical Physics*, 29(6):938–940, 06 1963.

[153] P. Nozières and S. Schmitt-Rink. Bose condensation in an attractive fermion gas: From weak to strong coupling superconductivity. *Journal of Low Temperature Physics*, 59:195–211, May 1985.

[154] W. E. Ormand, D. J. Dean, C. W. Johnson, G. H. Lang, and S. E. Koonin. Demonstration of the auxiliary-field Monte Carlo approach for *sd*-shell nuclei. *Phys. Rev. C*, 49:1422–1427, Mar 1994.

[155] G. Ortiz and J. Dukelsky. BCS–to–BEC crossover from the exact BCS solution. *Phys. Rev. A*, 72:043611, Oct 2005.

[156] Stephen P. Brooks and Andrew Gelman. General Methods for Monitoring Convergence of Iterative Simulations. *Journal of Computational and Graphical Statistics*, 7(4):434–455, 1998.

[157] Dany Page, James M. Lattimer, Madappa Prakash, and Andrew W. Steiner. Minimal Cooling of Neutron Stars: A New Paradigm. *The Astrophysical Journal Supplement Series*, 155(2):623–650, dec 2004.

[158] Pierre-Alexandre Pantel, Dany Davesne, and Michael Urban. Polarized Fermi gases at finite temperature in the BCS–BEC crossover. *Phys. Rev. A*, 90:053629, Nov 2014.

[159] Guthrie B. Partridge, Wenhui Li, Ramsey I. Kamar, Yean-an Liao, and Randall G. Hulet. Pairing and Phase Separation in a Polarized Fermi Gas. *Science*, 311(5760):503–505, 2006.

[160] A Pastore. An introduction to bootstrap for nuclear physics. *Journal of Physics G: Nuclear and Particle Physics*, 46(5):052001, Apr 2019.

[161] Fabian Pedregosa, Gaël Varoquaux, Alexandre Gramfort, Vincent Michel, Bertrand Thirion, Olivier Grisel, Mathieu Blondel, Peter Prettenhofer, Ron Weiss, Vincent Dubourg, Jake Vanderplas, Alexandre Passos, David Cournapeau, Matthieu Brucher, Matthieu Perrot, and Édouard Duchesnay. Scikit-learn: Machine Learning in Python. *Journal of Machine Learning Research*, 12:2825–2830, 2011.

[162] A. Perali, P. Pieri, G. C. Strinati, and C. Castellani. Pseudogap and spectral function from superconducting fluctuations to the bosonic limit. *Phys. Rev. B*, 66:024510, Jul 2002.

[163] Pierbiagio Pieri, Andrea Perali, and Giancarlo Calvanese Strinati. Enhanced paraconductivity-like fluctuations in the radiofrequency spectra of ultracold Fermi atoms. *Nature Physics*, 5(10):736–740, 2009.

[164] H.C. Pradhan, Y. Nogami, and J. Law. Study of approximations in the nuclear pairing-force problem. *Nuclear Physics A*, 201(2):357–368, 1973.

[165] Lukas Rammelmüller, Andrew C. Loheac, Joaquín E. Drut, and Jens Braun. Finite-Temperature Equation of State of Polarized Fermions at Unitarity. *Phys. Rev. Lett.*, 121:173001, Oct 2018.

[166] Lukas Rammelmüller, William J. Porter, Joaquín E. Drut, and Jens Braun. Surmounting the sign problem in nonrelativistic calculations: A case study with mass-imbalanced fermions. *Phys. Rev. D*, 96:094506, Nov 2017.

[167] M. Randeria, W. Zwerger, and M. Zwierlein. The BCS–BEC Crossover and the Unitary Fermi Gas. In Wilhelm Zwerger, editor, *The BCS–BEC Crossover and the Unitary Fermi Gas*, pages 1–32. Springer Berlin Heidelberg, Berlin, Heidelberg, 2012.

[168] Adam Richie-Halford, Joaquín E. Drut, and Aurel Bulgac. Emergence of a pseudogap in the BCS–BEC crossover, 2020.

[169] Alessandro Roggero, Abhishek Mukherjee, and Francesco Pederiva. Quantum Monte Carlo Calculations of Neutron Matter with Nonlocal Chiral Interactions. *Phys. Rev. Lett.*, 112:221103, Jun 2014.

[170] Dietrich Roscher, Jens Braun, Jiunn-Wei Chen, and Joaquín E Drut. Fermi gases with imaginary mass imbalance and the sign problem in Monte-Carlo calculations. *Journal of Physics G: Nuclear and Particle Physics*, 41(5):055110, mar 2014.

[171] R. Rossi, T. Ohgoe, E. Kozik, N. Prokof'ev, B. Svistunov, K. Van Houcke, and F. Werner. Contact and Momentum Distribution of the Unitary Fermi Gas. *Phys. Rev. Lett.*, 121:130406, Sep 2018.

[172] Ira Z. Rothstein and Prashant Shrivastava. Symmetry obstruction to Fermi liquid behavior in the unitary limit. *Phys. Rev. B*, 99:035101, Jan 2019.

[173] Jun John Sakurai and Eugene D Commins. Modern quantum mechanics, revised edition, 1995.

[174] Luca Salasnich, Nicola Manini, and Alberto Parola. Condensate fraction of a Fermi gas in the BCS-BEC crossover. *Phys. Rev. A*, 72:023621, Aug 2005.

[175] Christian Sanner, Edward J. Su, Aviv Keshet, Wujie Huang, Jonathon Gillen, Ralf Gommers, and Wolfgang Ketterle. Speckle Imaging of Spin Fluctuations in a Strongly Interacting Fermi Gas. *Phys. Rev. Lett.*, 106:010402, Jan 2011.

[176] G. Sarma. On the influence of a uniform exchange field acting on the spins of the conduction electrons in a superconductor. *Journal of Physics and Chemistry of Solids*, 24(8):1029–1032, 1963.

[177] André Schirotzek, Yong-il Shin, Christian H. Schunck, and Wolfgang Ketterle. Determination of the Superfluid Gap in Atomic Fermi Gases by Quasiparticle Spectroscopy. *Phys. Rev. Lett.*, 101:140403, Oct 2008.

[178] A. J. Schofield. Non-Fermi liquids. *Contemporary Physics*, 40(2):95–115, 1999.

[179] Armen Sedrakian, Jordi Mur-Petit, Artur Polls, and Herbert Müther. Pairing in a two-component ultracold Fermi gas: Phases with broken-space symmetries. *Phys. Rev. A*, 72:013613, Jul 2005.

[180] Daniel E. Sheehy and Leo Radzihovsky. BEC–BCS crossover, phase transitions and phase separation in polarized resonantly-paired superfluids. *Annals of Physics*, 322(8):1790–1924, 2007.

[181] Y. Shin, M. W. Zwierlein, C. H. Schunck, A. Schirotzek, and W. Ketterle. Observation of Phase Separation in a Strongly Interacting Imbalanced Fermi Gas. *Phys. Rev. Lett.*, 97:030401, Jul 2006.

[182] Arnold Sommerfeld. Zur elektronentheorie der metalle auf grund der fermischen statistik. *Zeitschrift für Physik*, 47(1-2):1–32, 1928.

[183] RL Stratonovich. On a Method of Calculating Quantum Distribution Functions. In *Soviet Physics Doklady*, volume 2, page 416, 1957.

[184] G. C. Strinati. Pairing Fluctuations Approach to the BCS–BEC Crossover. In Wilhelm Zwerger, editor, *The BCS–BEC Crossover and the Unitary Fermi Gas*, pages 99–126. Springer Berlin Heidelberg, Berlin, Heidelberg, 2012.

[185] Giancarlo Calvanese Strinati, Pierbiagio Pieri, Gerd Röpke, Peter Schuck, and Michael Urban. The BCS–BEC crossover: From ultra-cold Fermi gases to nuclear systems. *Physics Reports*, 738:1–76, Apr 2018.

[186] Masuo Suzuki. Fractal decomposition of exponential operators with applications to many-body theories and Monte Carlo simulations. *Physics Letters A*, 146(6):319–323, 1990.

[187] Hiroyuki Tajima, Ryo Hanai, and Yoji Ohashi. Strong-coupling corrections to spin susceptibility in the BCS–BEC-crossover regime of a superfluid Fermi gas. *Phys. Rev. A*, 93:013610, Jan 2016.

[188] Hiroyuki Tajima, Takashi Kashimura, Ryo Hanai, Ryota Watanabe, and Yoji Ohashi. Uniform spin susceptibility and spin-gap phenomenon in the BCS–BEC-crossover regime of an ultracold Fermi gas. *Phys. Rev. A*, 89:033617, Mar 2014.

[189] Shina Tan. Energetics of a strongly correlated Fermi gas. *Annals of Physics*, 323(12):2952 – 2970, 2008.

[190] Shina Tan. Generalized virial theorem and pressure relation for a strongly correlated Fermi gas. *Annals of Physics*, 323(12):2987 – 2990, 2008.

[191] Shina Tan. Large momentum part of a strongly correlated Fermi gas. *Annals of Physics*, 323(12):2971 – 2986, 2008.

[192] Robert J Tibshirani and Bradley Efron. An introduction to the bootstrap. *Monographs on statistics and applied probability*, 57:1–436, 1993.

[193] Tom Timusk and Bryan Statt. The pseudogap in high-temperature superconductors: an experimental survey. *Reports on Progress in Physics*, 62(1):61–122, jan 1999.

[194] Nandini Trivedi and Mohit Randeria. Deviations from Fermi-Liquid Behavior above T_c in 2D Short Coherence Length Superconductors. *Phys. Rev. Lett.*, 75:312–315, Jul 1995.

[195] Hale F Trotter. On the product of semi-groups of operators. *Proceedings of the American Mathematical Society*, 10(4):545–551, 1959.

[196] Matthias Troyer and Uwe-Jens Wiese. Computational Complexity and Fundamental Limitations to Fermionic Quantum Monte Carlo Simulations. *Phys. Rev. Lett.*, 94:170201, May 2005.

[197] JG Valatin. Comments on the theory of superconductivity. *Il Nuovo Cimento (1955-1965)*, 7(6):843–857, 1958.

[198] H. J. M. van Bemmel, D. F. B. ten Haaf, W. van Saarloos, J. M. J. van Leeuwen, and G. An. Fixed-node quantum monte carlo method for lattice fermions. *Phys. Rev. Lett.*, 72:2442–2445, Apr 1994.

[199] K. Van Houcke, F. Werner, E. Kozik, N. Prokof'ev, B. Svistunov, M. J. H. Ku, A. T. Sommer, L. W. Cheuk, A. Schirotzek, and M. W. Zwierlein. Feynman diagrams versus Fermi-gas Feynman emulator. *Nature Physics*, 8(5):366–370, 2012.

[200] Pauli Virtanen, Ralf Gommers, Travis E. Oliphant, Matt Haberland, Tyler Reddy, David Cournapeau, Evgeni Burovski, Pearu Peterson, Warren Weckesser, Jonathan Bright, Stéfan J. van der Walt, Matthew Brett, Joshua Wilson, K. Jarrod Millman, Nikolay Mayorov, Andrew R. J. Nelson, Eric Jones, Robert Kern, Eric Larson,

CJ Carey, İlhan Polat, Yu Feng, Eric W. Moore, Jake Vand erPlas, Denis Laxalde, Josef Perktold, Robert Cimrman, Ian Henriksen, E. A. Quintero, Charles R Harris, Anne M. Archibald, Antônio H. Ribeiro, Fabian Pedregosa, Paul van Mulbregt, and SciPy 1. 0 Contributors. SciPy 1.0: Fundamental Algorithms for Scientific Computing in Python. *Nature Methods*, 17:261–272, 2020.

[201] Yupeng Wang. Fermi-Liquid Features of the One-Dimensional Luttinger Liquid. *International Journal of Modern Physics B*, 12(32):3465–3473, 1998.

[202] W. W. Warren, R. E. Walstedt, G. F. Brennert, R. J. Cava, R. Tycko, R. F. Bell, and G. Dabbagh. Cu spin dynamics and superconducting precursor effects in planes above T_c in $\mathrm{yba_2cu_3o_{6.7}}$. *Phys. Rev. Lett.*, 62:1193–1196, Mar 1989.

[203] Steven Weinberg. Four golden lessons. *Nature*, 426(6965):389–389, 2003.

[204] Félix Werner and Yvan Castin. General relations for quantum gases in two and three dimensions: Two-component fermions. *Phys. Rev. A*, 86:013626, Jul 2012.

[205] S Wesolowski, R J Furnstahl, J A Melendez, and D R Phillips. Exploring Bayesian parameter estimation for chiral effective field theory using nucleon–nucleon phase shifts. *Journal of Physics G: Nuclear and Particle Physics*, 46(4):045102, feb 2019.

[206] Christopher KI Williams and Carl Edward Rasmussen. *Gaussian Processes for Machine Learning*, volume 2. MIT press Cambridge, MA, 2006.

[207] Kenneth G. Wilson. The renormalization group: Critical phenomena and the Kondo problem. *Rev. Mod. Phys.*, 47:773–840, Oct 1975.

[208] R. B. Wiringa and Steven C. Pieper. Evolution of Nuclear Spectra with Nuclear Forces. *Phys. Rev. Lett.*, 89:182501, Oct 2002.

[209] R. B. Wiringa, V. G. J. Stoks, and R. Schiavilla. Accurate nucleon-nucleon potential with charge-independence breaking. *Phys. Rev. C*, 51:38–51, Jan 1995.

[210] G. Wlazłowski, J. W. Holt, S. Moroz, A. Bulgac, and K. J. Roche. Auxiliary-Field Quantum Monte Carlo Simulations of Neutron Matter in Chiral Effective Field Theory. *Phys. Rev. Lett.*, 113:182503, Oct 2014.

[211] Gabriel Wlazłowski, Piotr Magierski, Joaquín E. Drut, Aurel Bulgac, and Kenneth J. Roche. Cooper Pairing Above the Critical Temperature in a Unitary Fermi Gas. *Phys. Rev. Lett.*, 110:090401, Feb 2013.

[212] Michael A. Woolf and F. Reif. Effect of magnetic impurities on the density of states of superconductors. *Phys. Rev.*, 137:A557–A564, Jan 1965.

[213] D.G. Yakovlev and C.J. Pethick. Neutron Star Cooling. *Annual Review of Astronomy and Astrophysics*, 42(1):169–210, 2004.

[214] Bing Yang, Yang-Yang Chen, Yong-Guang Zheng, Hui Sun, Han-Ning Dai, Xi-Wen Guan, Zhen-Sheng Yuan, and Jian-Wei Pan. Quantum criticality and the Tomonaga-Luttinger liquid in one-dimensional Bose gases. *Phys. Rev. Lett.*, 119:165701, Oct 2017.

[215] C. N. Yang. Concept of Off-Diagonal Long-Range Order and the Quantum Phases of Liquid He and of Superconductors. *Rev. Mod. Phys.*, 34:694–704, Oct 1962.

[216] Yi-Cong Yu, Yang-Yang Chen, Hai-Qing Lin, Rudolf A. Römer, and Xi-Wen Guan. Dimensionless ratios: Characteristics of quantum liquids and their phase transitions. *Phys. Rev. B*, 94:195129, Nov 2016.

[217] W. Zwerger. *The BCS–BEC Crossover and the Unitary Fermi Gas.* Springer-Verlag, Berlin, 2012.

[218] W. Zwerger. *The BCS–BEC Crossover and the Unitary Fermi Gas.* Springer-Verlag, Berlin, 2012.

[219] M. W. Zwierlein, J. R. Abo-Shaeer, A. Schirotzek, C. H. Schunck, and W. Ketterle. Vortices and superfluidity in a strongly interacting Fermi gas. *Nature*, 435:1047–1051, Jun 2005.

[220] M. W. Zwierlein, C. A. Stan, C. H. Schunck, S. M. F. Raupach, A. J. Kerman, and W. Ketterle. Condensation of Pairs of Fermionic Atoms near a Feshbach Resonance. *Phys. Rev. Lett.*, 92:120403, Mar 2004.

Appendix A

SCATTERING THEORY

Here we review some elements of scattering theory referenced in the main text, following Refs.[116, 173].

A.1 Two-body scattering

When a two-body system is governed by a central potential,

$$V = V(r), \tag{A.1}$$

where $r = |\mathbf{r}_1 - \mathbf{r}_2|$, then the motion of the system separates into the free motion of its center of mass and the relative motion of the two particles, which can be represented by the motion of a single fictitious particle, with reduced mass $m/2$, moving in an external potential. By assuming that the particle is free when far away from the origin, both before and after the collision, one can write the wavefunction as a superposition of an incoming plane wave and an outgoing spherical wave,

$$\psi(\mathbf{r}) \approx e^{ikz} + f(\theta)\frac{e^{ikr}}{r}, \tag{A.2}$$

where $f(\theta)$ is the scattering amplitude. Because the interaction is spherically symmetric, it is also natural to decompose the wavefunction using separation of variables in spherical coordinates,

$$\psi_{k\ell m}(\mathbf{r}) = R_{k\ell}(r) Y_{\ell m}(\theta, \varphi), \tag{A.3}$$

where $Y_{\ell m}(\theta, \varphi)$ are spherical harmonics, known eigenfunctions from the theory of angular momentum. Upon substituting

$$u(r) = rR_{k\ell}(r) \quad \text{and} \quad U(r) = \frac{2m}{\hbar^2}V(r) \tag{A.4}$$

one can state the radial Schrödinger equation as

$$\left(\frac{\partial^2}{\partial r^2} - \frac{\ell(\ell+1)}{r^2} - U(r) + k^2\right) u(r) = 0, \tag{A.5}$$

where $k = \sqrt{2mE}/\hbar$.

In the limit where only the lowest partial wave ($\ell = 0$ or s-wave) contributes, then scattering can be described by

$$\left(\frac{\partial^2}{\partial r^2} - U(r) + k^2\right) u(r) = 0, \tag{A.6}$$

and the asymptotic behavior of the radial function becomes

$$u(r) \sim \sin\left(kr + \delta(k)\right), \tag{A.7}$$

where $\delta(k)$ is the s-wave phase shift that depends on the incident energy. The scattering amplitude is then given by

$$f(k) = \frac{1}{k\cot\delta(k) - ik}, \tag{A.8}$$

and the total scattering cross-section is $\sigma = 8\pi|f(k)|^2$. The phase shift can be expanded as

$$k\cot\delta(k) = -\frac{1}{a} + \frac{r_e}{2}k^2 + \mathcal{O}(k^4), \tag{A.9}$$

which provides a definition of the s-wave scattering length a the effective range r_e of the interaction.

A.1.1 Bound states

The poles of the scattering amplitude in Eq. (A.8) define the bound states and resonances of the two-body problem. Bound states are found on the positive imaginary axis in k-space, $k = i\kappa$, with $\kappa > 0$:

$$i\kappa\cot\delta(i\kappa) + \kappa = 0, \tag{A.10}$$

with dimer binding energy given by

$$E_d = \frac{\hbar^2\kappa^2}{m}. \tag{A.11}$$

If the potential is tuned to the limit $k|a| \gg 1$ and $r_e \ll 1/k$, then the scattering amplitude becomes $f(k) = -1/ik$, the total scattering cross-section achieves its maximum value at $\sigma = 4\pi/k^2$, and the bound state energy goes to zero. This is the unitary limit and its behavior is universal, meaning it depends only on the scattering length a and not on the details of the short-range potential.

Appendix B

PARTICLE ASYMMETRY CONSTRAINED ENSEMBLE THERMODYNAMIC RELATIONS

The particle asymmetry constrained ensemble (PACE) is a blend between the grand canonical ensemble, where the thermodynamic variables are the temperature, volume, and chemical potentials and the characteristic state function is the grand potential $\Omega(T, V, \mu, \mu_-)$, and the canonical ensemble, where the thermodynamic variables are the temperature, volume, and particle numbers and the characteristic state function is the Helmholtz free energy $F(T, V, N, N_-)$. In the study of mixtures and polymers, researchers sometimes use the semi-grand canonical ensemble, where the total number of particles is fixed, but the composition of particles may change [31, 113]. In contrast, because we wish to capitalize upon the sign-problem avoidance of the PACE, we wish to simulate systems where the total number of particles may change, but the mixture of spin-up and spin-down particles is fixed. One may think of these systems as in contact with a heat bath and a particle bath that is constrained to preserve a fixed particle asymmetry.

This can be accomplished by applying a Legendre transform where the extensive quantity is the particle asymmetry N_- and its conjugate variable is $(-\beta\mu_-)$. Transforming from the grand canonical ensemble yields the PACE potential

$$\begin{aligned} \mathcal{W}\left(T, V, \mu, N_-\right) &= \Omega\left(T, V, \mu_\pm\right) - \frac{\partial \Omega}{\partial(\beta\mu_-)}\beta\mu_- \\ &= \Omega\left(T, V, \mu_\pm\right) + N_-\mu_-, \end{aligned} \tag{B.1}$$

whose differential is given by

$$\begin{aligned} \mathrm{d}\mathcal{W} &= \mathrm{d}\Omega + \mu_-\,\mathrm{d}N_- + N_-\,\mathrm{d}\mu_- \\ &= -S\,\mathrm{d}T - \mathcal{P}\,\mathrm{d}V - N\,\mathrm{d}\mu + \mu_-\,\mathrm{d}N_- \,. \end{aligned} \tag{B.2}$$

One gets the same result when transforming from the canonical ensemble, using a Legendre transform where the extensive quantity is N and its conjugate variable is $(-\beta\mu)$,

$$\begin{aligned} \mathcal{W} &= F\left(T, V, N_{\pm}\right) - \frac{\partial \Omega}{\partial N} N \\ &= F\left(T, V, N_{\pm}\right) - N\mu, \\ \mathrm{d}\mathcal{W} &= \mathrm{d}F - \mu\,\mathrm{d}N - N\,\mathrm{d}\mu \\ &= -S\,\mathrm{d}T - \mathcal{P}\,\mathrm{d}V - N\,\mathrm{d}\mu + \mu_{-}\,\mathrm{d}N_{-}\,. \end{aligned} \tag{B.3}$$

The method of transformation between ensembles is standard [118, 5], so here we outline the main results of our transformation. Like the GCE or the canonical ensemble, the PACE is an artificial construct, so it produces averages that are consistent with the other ensembles when they represent the same state of the system:

$$\begin{aligned} \langle N \rangle_{\mathcal{W}} &= -\left(\frac{\partial \mathcal{W}}{\partial \mu},\right)_{T,V,N_{-}}, \\ \langle \mu_{-} \rangle_{\mathcal{W}} &= \left(\frac{\partial \mathcal{W}}{\partial N_{-}}\right)_{T,V,\mu}, \\ \langle \mathcal{P} \rangle_{\mathcal{W}} &= -\left(\frac{\partial \mathcal{W}}{\partial V},\right)_{T,\mu,N_{-}}, \\ \langle S \rangle_{\mathcal{W}} &= -\left(\frac{\partial \mathcal{W}}{\partial T}.\right)_{V,\mu,N_{-}}, \end{aligned} \tag{B.4}$$

where $\langle A \rangle_{\mathcal{W}}$ denotes the average of some observable $\hat{A}$ in the PACE.

Similarly, let $\langle A \rangle_{\Omega}$ denote the average in the GCE and $\langle A \rangle_{F}$ denote the average in the canonical ensemble. The averages in the GCE and PACE are then related by [122]

$$\begin{aligned} \langle A \rangle_{\mathcal{W}} &= \langle A \rangle_{\Omega} - \frac{1}{2}\left\langle \delta N_{-}^{2} \right\rangle_{\Omega} \frac{\partial^{2}}{\partial N_{-}^{2}} \langle A \rangle_{\Omega} \\ &= \langle A \rangle_{\Omega} - \frac{1}{2}\frac{\partial N_{-}}{\partial(\beta\mu_{-})}\frac{\partial^{2}}{\partial N_{-}^{2}} \langle A \rangle_{\Omega} \\ &= \langle A \rangle_{\Omega} - \frac{1}{2}\frac{\partial}{\partial(\beta\mu_{-})}\frac{\partial}{\partial N_{-}} \langle A \rangle_{\Omega} \\ &= \langle A \rangle_{\Omega} - \frac{1}{2}\frac{\partial}{\partial(\beta\mu_{-})}\left(\frac{\partial(\beta\mu_{-})}{\partial N_{-}}\right)\frac{\partial}{\partial(\beta\mu_{-})} \langle A \rangle_{\Omega}\,. \end{aligned} \tag{B.5}$$

The correction term disappears in the thermodynamic limit, decreasing as $\mathcal{O}(N^{-1})$ and leading to an equivalence of ensembles.

Conversely, the fluctuations may vary in different ensembles and care should be taken when comparing these fluctuations. In general, the covariance of two variables A and B in the different ensembles is given by [122]

$$\langle \delta A \delta B \rangle_{\mathcal{W}} = \langle \delta A \delta B \rangle_{\Omega} - \left(\frac{\partial(\beta\mu_-)}{\partial N_-}\right)\left(\frac{\partial \langle A \rangle_\Omega}{\partial(\beta\mu_-)}\right)\left(\frac{\partial \langle B \rangle_\Omega}{\partial(\beta\mu_-)}\right). \tag{B.6}$$

The most obvious example is the fluctuations in N_-, which are zero by definition in the PACE, and nonzero in the GCE, leading to the familiar

$$\left\langle \delta N_-^2 \right\rangle_\Omega = TV\chi_s, \tag{B.7}$$

where we have inserted the volume factor for concordance with the lattice expression Eq. (3.5).

This fact that the GCE-PACE transformation yields the spin susceptibility fluctuation theorem places the PACE on similar footing as the grand canonical, canonical, and micro-canonical ensembles, whose transformations also yield fluctuation theorems for important second-order thermodynamic derivatives. To wit, transforming particle number fluctuations from the canonical ensemble, where they are zero, to the GCE yields the isothermal compressibility and transforming energy fluctuations between the micro-canonical ensemble, where they are zero, and the canonical ensemble yields the specific heat.

The PACE potential is connected to the PACE partition function by

$$\mathcal{W}(\eta) = -k_B T \ln P(\eta), \tag{B.8}$$

where we have added explicit η dependence to agree with $P(\eta)$, which is defined in Eq. (2.64a).

Appendix C

DETERMINING ENERGIES FOR EVEN-ODD STAGGER CALCULATIONS

Measurements of the energy, as well as derived quantities such as the even-odd staggering, are sensitive to lattice effects that must be corrected in order to estimate observables in the continuum limit. In this appendix, we detail the steps required to estimate the energy, and therefore the even-odd energy staggering, in the continuum limit.

Throughout this section, a tilde over a variable will denote that it has been scaled by some other energy scale. We scale energies by the energy of a free Fermi gas at zero temperature, and temperatures and chemical potentials by the Fermi energy. In the text, we will refer to the scaled values as "reduced" and the unscaled values as "absolute."

C.0.1 Extrapolation to the continuum limit

It is instructive to first consider the energy estimation of the free gas of spin-1/2 fermions. In the continuum, one first solves for the reduced chemical potential, $\widetilde{\mu} \equiv \mu/\varepsilon_F$ required to achieve a desired reduced temperature $\widetilde{T} \equiv T/\varepsilon_F$,

$$1 = \frac{3}{2}\widetilde{T}^{3/2} \int_0^\infty \frac{\mathrm{d}z\, z^{1/2}}{1 + \exp\left[z - \widetilde{\mu}/\widetilde{T}\right]}. \tag{C.1}$$

Once this value of $\widetilde{\mu}$ is determined, it can be used to solve for the reduced energy of a system at temperature $\widetilde{T}$,

$$\widetilde{E}_c \equiv \frac{E_c}{\frac{3}{5}N\varepsilon_F} = \frac{5}{2}\widetilde{T}^{5/2} \int_0^\infty \frac{\mathrm{d}z\, z^{3/2}}{1 + \exp\left[z - \widetilde{\mu}/\widetilde{T}\right]}, \tag{C.2}$$

where the subscript c indicates that this energy is computed in the continuum.

One can also solve this system on a cubic lattice of side length $L = N_x = N_y = N_z$. The lattice momenta are given by $\vec{p}_n = 2\pi(i_x\hat{x} + i_y\hat{y} + i_z\hat{z})/L$, where $i_j = -L/2 + 1, \ldots, L/2$,

$j \in \{x, y, z\}$. Then, as before, one finds the value of the chemical potential required to give us a desired particle number N at the reduced temperature $\widetilde{T}$,

$$N = 2 \sum_{\vec{n}} \frac{\alpha \exp\left[-\widetilde{\beta} \frac{\widetilde{p}_{\vec{n}}^2}{2m}\right]}{1 + \alpha \exp\left[-\widetilde{\beta} \frac{\widetilde{p}_{\vec{n}}^2}{2m}\right]}, \tag{C.3}$$

where the tildes indicate that the lattice momenta and inverse temperature is measured in units of the continuum Fermi energy, $\varepsilon_F = \left(3\pi^2 N/V\right)^{2/3}/2$, and $\alpha \equiv \exp(\beta\mu)$. After determining $\widetilde{\mu}$, one can than calculate the energy of the free Fermi gas on the lattice as

$$\frac{E_\ell}{\varepsilon_F} = 2 \sum_{\vec{n}} \frac{\widetilde{p}_{\vec{n}}^2}{2m} \frac{\alpha \exp\left[-\widetilde{\beta} \frac{\widetilde{p}_{\vec{n}}^2}{2m}\right]}{1 + \alpha \exp\left[-\widetilde{\beta} \frac{\widetilde{p}_{\vec{n}}^2}{2m}\right]}, \tag{C.4}$$

where the subscript ℓ indicates that this energy is computed on the lattice.

In Fig. C.1, we compare the energies of the free Fermi gas computed on the lattice and in the continuum. For the temperature range of interest $0.1 \leq \widetilde{T} \leq 0.3$, the residual $\delta = |E_c - E_\ell|$ has two zeros at roughly $N \approx 30$ and $N \approx 60$. In typical QMC simulations, one chooses particle numbers in this range to minimize the residuals. However, we constrain our simulations to a range of particle numbers, for which the residuals may not match. To extrapolate to the continuum limit, we multiply our lattice energies by an extrapolation coefficient

$$E_c = C_\ell E_\ell, \quad \text{where} \quad C_\ell \equiv \frac{E_{FFG,c}}{E_{FFG,\ell}}. \tag{C.5}$$

For the free Fermi gas, Eq. (C.5) is tautologistic. In our calculations of the interacting gas, applying Eq. (C.5) amounts to the assumption that the lattice effects predominantly affect the kinetic energy operator as opposed to the potential energy operator. A similar procedure for extrapolating to the continuum limit was used in an AFQMC study of neutron matter with chiral effective field theory [210].

C.0.2 Finite range correction

In addition to the continuum extrapolation focused on the kinetic energy in Appendix C.0.1, we also use the effective range expansion

$$\frac{E}{E_{FFG}} = \xi + \zeta_e k_F r_e + \ldots, \tag{C.6}$$

where the value of ζ_e has been estimated as $\zeta_e = 0.12(3)$ [204, 44] and the effective range for a cubic cutoff is [204]

$$r_e = \ell \frac{12\sqrt{2}}{\pi^3} \arcsin \frac{1}{\sqrt{3}} \approx 0.337\ell, \tag{C.7}$$

where ℓ is the lattice constant. We are interested in correcting our lattice calculations conducted with finite effective range to continuum energies with zero range interactions. We therefore combine the continuum limit extrapolation of Appendix C.0.1 with Eq. (C.7) by subtracting the finite range correction,

$$\frac{E_c}{E_{FFG}} = C_\ell \frac{E_\ell}{E_{FFG}} - \zeta_e k_F r_e. \tag{C.8}$$

C.0.3 Reduced temperature shift

The methods of Appendices C.0.1 and C.0.2 yield estimates of the energy of a system at some absolute temperature T and particle number N. To remove the explicit dependence on particle number, one often scales the energies by the energy of a free Fermi gas at zero temperature and the temperatures by the Fermi energy, as in Eqs. (C.1) and (C.2). However, it is important to realize that when estimating observables using the methods in § 2.4, the constrained ensemble inherits the absolute temperature of its "parent" GCE simulation. The reduced temperature, $\widetilde{T}$, will be different depending on the projected particle number.

To illustrate this effect, we conducted constrained ensemble simulations of the free Fermi gas. This is computationally inexpensive since, with no interaction term, only one Monte Carlo sample is required to achieve convergence. This allows us to explain the reduced temperature shift inherent in constrained ensemble methods and also serves as a validation step for our simulation software.

Figure C.2 depicts a "stagger plot," similar to Fig. 3.4 for the unitary Fermi gas. The "parent" GCE simulation was conducted at $\widetilde{T}_{GCE} = 0.2$, from which the constrained ensemble energies were calculated. The blue markers indicate energies calculated using Eq. (C.5), which are calculated at the same absolute temperature as the GCE,

$$\widetilde{E}\left(N, \widetilde{T}\right) = \widetilde{E}\left(N, \frac{T_{GCE}}{\varepsilon_F(N)}\right). \tag{C.9}$$

The red markers indicate the energies calculated at the same reduced temperature as in the GCE

$$\widetilde{E}\left(N, \widetilde{T}_{GCE}\right) = \widetilde{E}\left(N, \frac{T_{GCE}}{\varepsilon_F(N)}\right) + f_{\text{shift}}\left(\widetilde{T}_{GCE}, \frac{T_{GCE}}{\varepsilon_F(N)}\right), \tag{C.10a}$$

where

$$f_{\text{shift}} = \widetilde{E}_{eos}\left(\widetilde{T}_{GCE}\right) - \widetilde{E}_{eos}\left(\frac{T_{GCE}}{\varepsilon_F(N)}\right), \tag{C.10b}$$

and $\widetilde{E}_{eos}$ is the equation of state of the system under study. For the validation case of the free Fermi gas $\widetilde{E}_{eos} = \widetilde{E}_c$ from Eq. (C.2). For the interacting gas in our study, the equation of state is derived from a previous study of the unitary Fermi gas [60]. As expected, the reduced temperature shift brings the red markers in Fig. C.2 in line with the continuum value for the same reduced temperature.

Realizing that the constrained ensembles probe different reduced temperatures also allows us to probe many different temperatures from a single GCE simulation. Figure C.3 shows the results of nine GCE simulations of the free Fermi gas. For each "parent" GCE simulation, the constrained ensemble methods produced energy estimates for nine different particle numbers. Since each of these particle numbers yielded a different reduced temperature, the effect of the constrained ensemble method is to spread each GCE simulation into (sometimes overlapping) temperature ranges.

For reference, we also show the importance of the continuum limit extrapolation in Eq. (C.5) by plotting the uncorrected lattice energies (still with reduced temperature shift) in the lower panel of Fig. C.3. The behavior is justified when one considers the negative slope of the lattice energies in Fig. C.1 around $N \approx 30$ where our GCE calculations were performed. Since an increase in particle number N, decreases the reduced temperature $\widetilde{T}$, the residuals in the lower panel of Fig. C.3 have the opposite slope to the ones in Fig. C.1.

While the continuum limit extrapolation of Appendix C.0.1 is widely accounted for in AFQMC literature. However, one finds no mention of the required reduced temperature corrections in the constrained ensemble literature [154, 120, 80, 107, 33]. It is possible that this omission does not affect estimates of the pairing gap since, when evaluating Δ_E using centered difference formulas, the increase in energy below the central particle number will be approximately cancelled out by the decrease in energy above the central particle number. So in the context of the pairing gap, the temperature correction may be formally required but negligible.

The effect on the spin susceptibility may depend on the way in which it is calculated. Our method uses the particle asymmetry constrained ensemble so that the scaled spin susceptibility is

$$\frac{\chi_s}{\chi_0} = \frac{2}{3N\widetilde{T}} \sum_{\eta} \eta^2 P(\eta). \tag{C.11}$$

In this case, each term contributing to the sum comes from a different particle asymmetry projection but the total particle number remains roughly the same so the temperature correction may be safely neglected. Lastly, when directly evaluating energies the temperature correction is plainly required, as demonstrated in Fig. C.2.

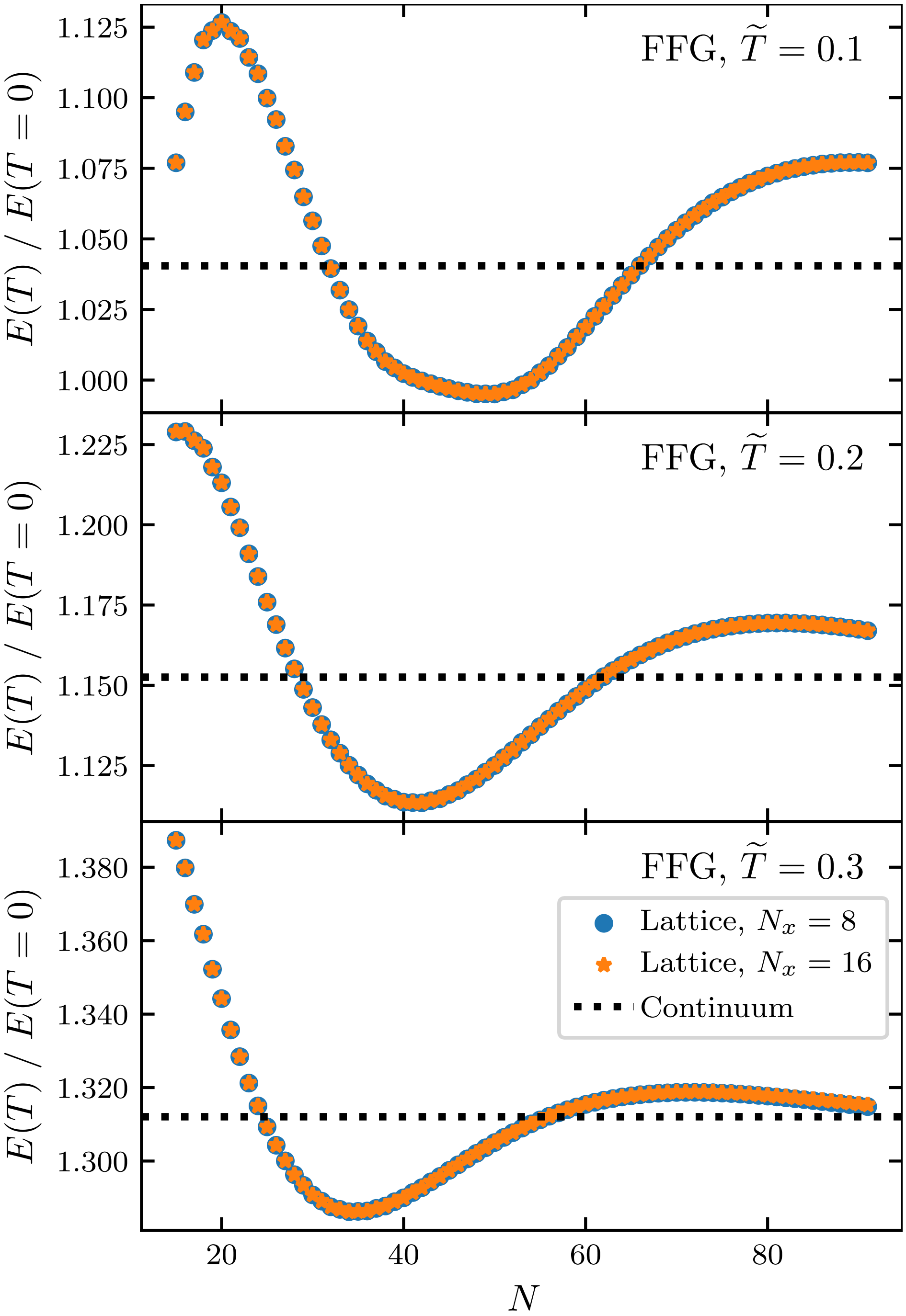

Figure C.1: A comparison of lattice and continuum energies for the free Fermi gas at $\widetilde{T} \in \{0.1, 0.2, 0.3\}$. Dashed lines indicate the continuum value, which is independent of particle number. The circles and stars indicate the identical values for 8^3 and 16^3 lattices, respectively.

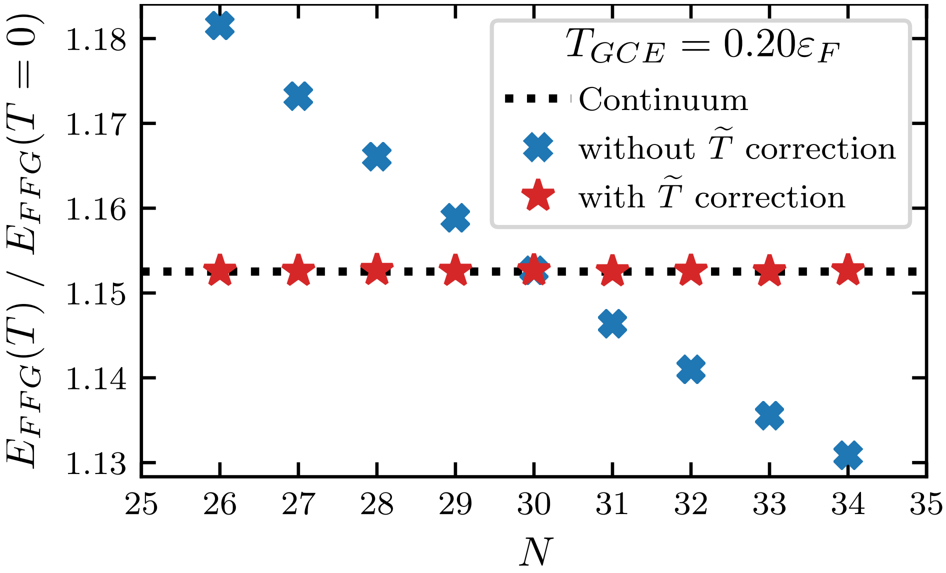

Figure C.2: An energy "stagger" plot for the free Fermi gas, derived using constrained ensembles from a GCE simulation at $\widetilde{T} = T/\varepsilon_F = 0.2$ on a 10^3 lattice. The energy is scaled by the energy of a free Fermi gas at zero temperature. The dashed line indicates the continuum calculation. The blue 'X' symbols indicate energies calculated at the same absolute temperature as in the GCE, see Eq. (C.9) whereas the red star symbols indicate energies calculated at the same reduced temperature as in the GCE, see Eq. (C.10b).

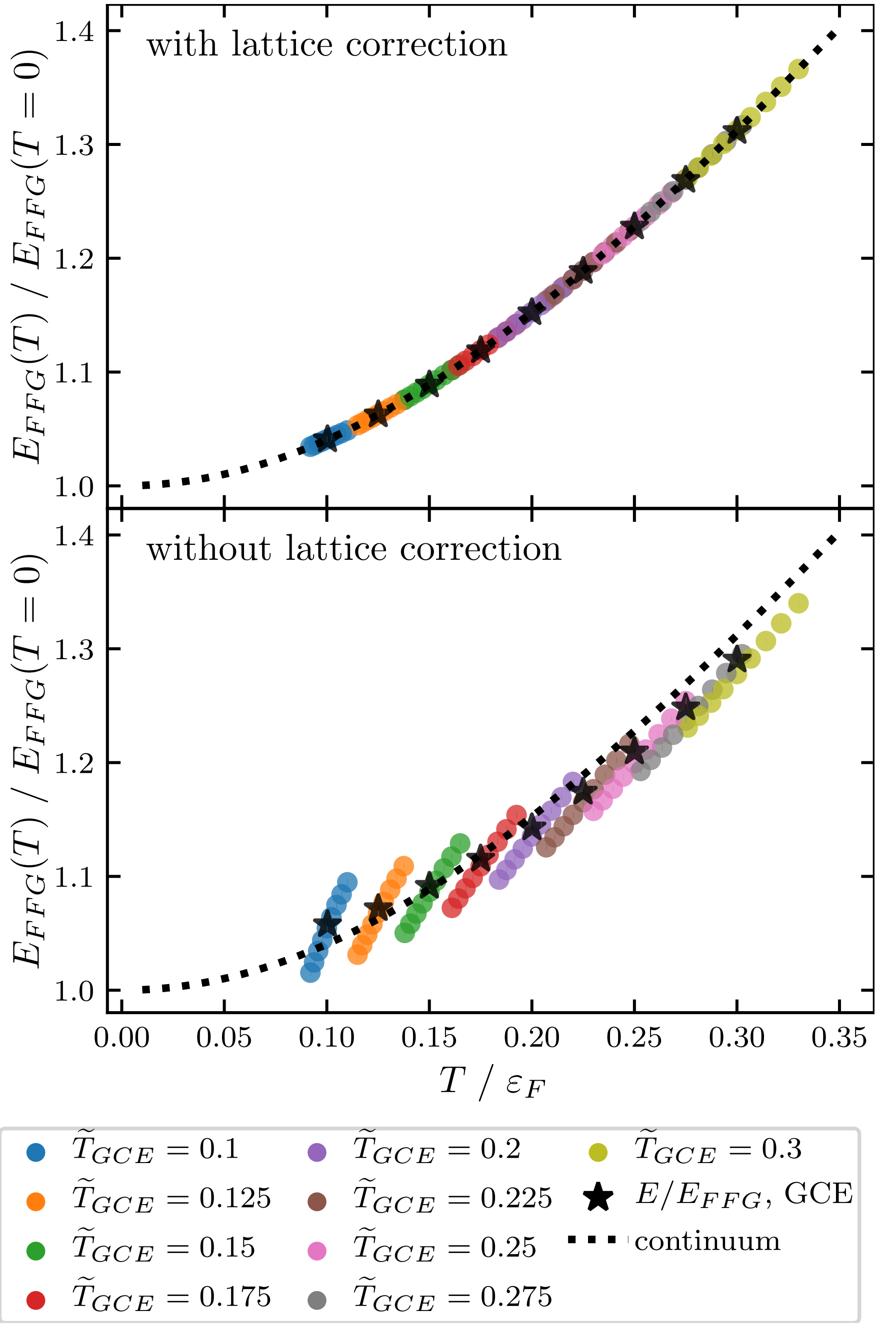

Figure C.3: Constrained ensemble methods spread the temperature of each GCE simulation out into overlapping ranges. Each color represents one “parent” GCE, the results of which are represented by black stars. Each GCE is then constrained to a fixed particle number, resulting in different reduced temperatures that spread out away from $\widetilde{T}_{GCE}$.

Appendix D

CALCULATING CONSTRAINED ENSEMBLE OBSERVABLES IN AFQMC

Here we outline the MCMC formalism to compute the observables $X(\varphi,\theta), E(\varphi,\theta), N_{\pm}(\varphi,\theta)$. In our notation, $\mathcal{U}$ is the single particle basis representation of the usual product of imaginary-time evolution operators $\mathcal{U} = \mathcal{U}_{N_\tau} \ldots \mathcal{U}_2 \mathcal{U}_1$. For the unconstrained grand canonical ensemble, we have $\mathcal{U}_\uparrow = \mathcal{U}_\downarrow$. Thus, when we explicitly include arrow subscripts, it is implied that we are calculating projected observables in the constrained ensemble. And when we omit the arrow subscripts, we are referencing a value calculated in the unconstrained grand canonical ensemble. For simultaneous projection of the total particle number and the particle difference between two flavors, we define $\mathcal{U}_{\uparrow,\downarrow} = e^{-i(\varphi \pm \theta)}\mathcal{U}$.

D.1 *Calculating occupation matrices*

In the unconstrained grand canonical simulation, the imaginary time evolution operator is computed as a QDR decomposition, as described in § 2.3.1. To compute $\mathcal{U}_\sigma$, one might naively expect to update the QDR decomposition at the end of the imaginary time evolution

$$\mathcal{U}_\sigma = e^{-i\alpha_\sigma}\mathcal{Q}\mathcal{D}\mathcal{R}, \tag{D.1}$$

$$1 + \mathcal{U}_\sigma = \mathcal{Q}\left[\mathcal{Q}^\dagger \mathcal{R}^{-1} + e^{-i\alpha_\sigma}\mathcal{D}\right] R = \mathcal{Q}\widetilde{\mathcal{Q}}_\sigma \widetilde{\mathcal{D}}_\sigma \widetilde{\mathcal{R}}_\sigma \mathcal{R}, \tag{D.2}$$

$$n_\sigma = 1 - \frac{1}{1+\mathcal{U}_\sigma} = 1 - \mathcal{R}^{-1}\widetilde{\mathcal{R}}_\sigma^{-1}\widetilde{\mathcal{D}}_\sigma^{-1}\widetilde{\mathcal{Q}}_\sigma^\dagger \mathcal{Q}^\dagger, \tag{D.3}$$

where $\sigma \in \{\uparrow,\downarrow\}$ (not to be confused with the auxiliary field) and $\alpha_\sigma = (\varphi \pm \theta)$. However, we can avoid the cost of these extra QDR decompositions by writing the occupation matrix as

$$n_\sigma = 1 - \frac{1}{1 + e^{-i\alpha_\sigma}\mathcal{U}} = 1 - e^{i\alpha_\sigma}\left[\left(e^{i\alpha_\sigma} - 1\right) + (1 + \mathcal{U})\right]^{-1}, \tag{D.4}$$

and using the Woodbury matrix identity

$$(A + BCD)^{-1} = A^{-1} - A^{-1}B\left[C^{-1} + DA^{-1}B\right]^{-1}DA^{-1}, \tag{D.5}$$

with $B = D = 1$, $C = (e^{i\alpha} - 1)$, and $A = (1 + \mathcal{U})$, $A^{-1} = (1 + \mathcal{U})^{-1} = (1 - n)$. Thus

$$n_\sigma = 1 - e^{i\alpha_\sigma}(1 - n)\left\{1 - \left[\frac{1}{e^{i\alpha_\sigma} - 1} + (1 - n)\right]^{-1}(1 - n)\right\}, \tag{D.6}$$

and we can use batched matrix multiplication, rather than QDR decomposition, to calculate the occupation matrices for each projection angle.

Although we are guaranteed $0 \le n_{i,j} \le 1$, the occupation matrices may still be ill conditioned and one may reasonably worry about the stability of multiplying and inverting matrices like $1 - n$. However, in practice, we find that the Woodbury method achieves an absolute difference of $\sim 10^{-9}$ compared to the brute force QDR decomposition, even at low temperatures. We use these occupation matrices in momentum and position space to calculate observables in the constrained ensemble.

D.2 Calculating the constrained statistical weights

In addition to calculating physical observables from occupation matrices, one must also compute the statistical weights $F[\sigma, \varphi, \theta]$. In Eq. (2.72b), $F[\sigma, \varphi, \theta]$ is expressed as a ratio of determinants that we expect to be large quantities that are not known with great precision. We therefore simplify the statistical weights as

$$\begin{aligned}
F[\sigma, \varphi, \theta] &= e^{i\varphi N}\frac{\det\left[1 + e^{-i(\varphi+\theta)}\mathcal{U}\right]}{\det[1 + \mathcal{U}]}\frac{\det\left[1 + e^{-i(\varphi-\theta)}\mathcal{U}\right]}{\det[1 + \mathcal{U}]} & \text{(D.7)}\\
&= e^{i\varphi N}\frac{\det\left[1 + \mathcal{U} + \left(e^{-i(\varphi+\theta)} - 1\right)\mathcal{U}\right]}{\det[1 + \mathcal{U}]}\frac{\det\left[1 + \mathcal{U} + \left(e^{-i(\varphi-\theta)} - 1\right)\mathcal{U}\right]}{\det[1 + \mathcal{U}]}, & \text{(D.8)}\\
&= e^{i\varphi N}\det\left[1 + \left(e^{-i(\varphi+\theta)} - 1\right)\frac{\mathcal{U}}{1 + \mathcal{U}}\right]\det\left[1 + \left(e^{-i(\varphi-\theta)} - 1\right)\frac{\mathcal{U}}{1 + \mathcal{U}}\right]. & \text{(D.9)}
\end{aligned}$$

D.3 Reducing the number of observable calculations

Appendix D addressed the computation of the φ, θ-observables. We then take the discrete Fourier transform of these values to compute the particle projected observables. Suppose we would like to estimate the Fourier integrals in Eq. (2.70) using n_f points in both φ and θ. Since we compute different observables for the ↑ and ↓ system, one would naively expect to compute $2n_f^2$ observables. However, we can greatly reduce the number of computed observables.

First, suppose $\varphi_i = -\pi + i2\pi/n_f$ for $i = 0, 1, 2, \ldots, n_f$ and similarly $\theta_j = -\pi + j2\pi/n_f$ for $j = 0, 1, 2, \ldots, n_f$. Then we can think of organizing observables in a matrix with rows corresponding to different values of φ and columns corresponding to different values of θ. We must then compute observables for all values in the matrices

$$(\varphi + \theta)_{i,j} = -2\pi + (i + j)\frac{2\pi}{n_f}, \tag{D.10}$$

$$(\varphi - \theta)_{i,j} = (i - j)\frac{2\pi}{n_f}. \tag{D.11}$$

But note that

$$(\varphi + \theta) = (\varphi - \theta)\, J, \tag{D.12}$$

where

$$J_{i,j} = \begin{cases} 1, & j = n_f - i + 1, \\ 0, & j \neq n_f - i + 1 \end{cases}, \tag{D.13}$$

is the exchange matrix. So if we compute the spin-↑ observables, we already have all of the values needed for the spin-↓ observables.

This reduces the number of required calculations by a factor of two, but we can do better. Note that the matrix $(\varphi + \theta)_{i,j}$ is a Hankel matrix and therefore has only $2n_f + 1$ unique values. For example, with $n_f = 4$, $(\varphi + \theta)_{i,j}$ has the structure

$$\begin{bmatrix} a & b & c & d \\ b & c & d & e \\ c & d & e & f \\ d & e & f & g \end{bmatrix}.$$

So instead of computing observables on the matrix $(\varphi + \theta)_{i,j}$, one can instead compute observables in the array $\omega_k = -2\pi + 4\pi k/(2n_f - 1)$ for $k = 0, 1, 2, \ldots, 2n_f - 1$. To map the observables back to the independent φ, θ space, we use

$$(\varphi + \theta)_{i,j} = \omega_{k=i+j}, \tag{D.14}$$

$$(\varphi - \theta)_{i,j} = \omega_{k=n_f-1-j+i}, \tag{D.15}$$

where we assume zero-based indexing in i, j, and k. Thus, we have reduced the number of required observable calculations from $2n_f^2 \rightarrow 2n_f - 1$.

Appendix E

GAUSSIAN PROCESS REGRESSION OF ξ AND Δ

As discussed in § 3.4, the temperature "smearing" effect (described in more detail in Appendix C.0.3), combined with the multiple methods for estimating Δ_E leads to a profusion of observations that make it difficult to visualize and compare our results to others. The same surplus of observations occurs for ξ, with multiple estimates coming from Eq. (3.9) and from measurements of E/E_{FFG} in the GCE.

To resolve this, we use a Gaussian process (GP) regressor to interpolate our data. A similar approach is used in nuclear theory, where an abundance of competing nuclear mass models make different predictions for nuclear separation energies and one wishes to extrapolate far from the valley of stability [148, 147, 146], with one key difference being that we use GP regression to interpolate rather than extrapolate. GPs have also been used for parameter estimation in chiral effective field theories [205].

GP regression is a non-parametric, Bayesian approach to regression, in which we treat our results as a training set for a new statistical model for each scattering length. For Δ_E, the training set includes all measurements of $\Delta_E^{(5)}$ and $\Delta_E^{(f)}$ for all lattice sizes $N_x \geq 8$. For ξ, the training set includes all measurements of ξ from Eq. (3.9) and of E/E_{FFG} from the GCE, for lattice sizes $N_x \geq 8$. Because we use GPs for interpolation and clarity in plotting, and not for estimation of T^*, we do not use cross-validation or split our data into training, testing, and validation sets, which is de rigueur when building a model to predict new results [92].

We briefly introduce the key concepts of GP regression and refer the reader to Williams and Rasmussen [206] for a more thorough, pedagogical introduction. Let $\mathbf{y}$ be the target vector of measurements we wish to interpolate (either Δ_E or ξ) and $\mathbf{x}$ be the input vector of temperatures T/ε_F. We wish to find a real process $f(\mathbf{x}, \theta)$ that will model and predict new target output given arbitrary inputs,

$$\mathbf{y} = f(\mathbf{x}, \theta) + \epsilon, \tag{E.1}$$

where θ encapsulates the parameters of our statistical model and ϵ represents identically distributed Gaussian noise, with zero mean and variance σ^2, which differentiates the observed values from the function values. Following the "function-space view" [206], one can define the mean $m(\mathbf{x})$ and covariance $k(\mathbf{x}, \mathbf{x}')$ of $f(\mathbf{x})$ as

$$\mu(\mathbf{x}) = \mathbb{E}\left[f(\mathbf{x}))\right], \tag{E.2}$$

$$k(\mathbf{x}, \mathbf{x}') = \mathbb{E}\left[(f(\mathbf{x}) - \mu(\mathbf{x}))(f(\mathbf{x}') - \mu(\mathbf{x}'))\right], \tag{E.3}$$

and approximate $f(\mathbf{x})$ by a Gaussian process

$$f(\mathbf{x}) \approx \mathcal{GP}\left(\mu(\mathbf{x}), k_\theta(\mathbf{x}, \mathbf{x}')\right), \tag{E.4}$$

which is completely specified by its mean and covariance functions. We take the covariance function to be the weighted sum of a $\nu = 3/2$ Matérn kernel and a white noise kernel

$$k(d_{ij}) = \underbrace{\eta^2 \left(1 + \frac{\sqrt{3} d_{ij}}{\rho}\right) e^{\left(-\frac{\sqrt{3} d_{ij}}{\rho}\right)}}_{\text{Matérn}} + \underbrace{\delta_{ij} \varepsilon}_{\text{white noise}}, \tag{E.5}$$

where $d_{ij} \equiv |x_i - x_j|$ and δ_{ij} is the Kronecker delta. The Matérn kernel is a generalization of the popular radial-basis function (RBF or "squared exponential") kernel, and is appropriate for learning functions that are at least once differentiable, in contrast to the assumption of infinite differentiability with the RBF kernel [206, 62]. Thus, our statistical model has four parameters $\theta \coloneqq (\mu, \eta, \rho, \varepsilon)$: the mean μ, the correlation strength η, the Matérn coherence length ρ, and the noise level ε.

GP regression estimates the parameters θ by specifying a prior distribution $p(\theta)$ and relocating those probabilities based on Bayes rule

$$p\left(\theta | \mathbf{y}, \mathbf{x}\right) = \frac{p\left(\mathbf{y} | \mathbf{x}, \theta\right) p\left(\theta\right)}{p(\mathbf{y} | \mathbf{x})}, \tag{E.6}$$

where the marginal likelihood $p(\mathbf{y}|\mathbf{x})$ is given by

$$p\left(\mathbf{y}|\mathbf{x}\right) = \int p\left(\mathbf{y}|\mathbf{x}, \theta\right) p(\theta) d\theta. \tag{E.7}$$

For each observable, ξ and Δ, and at each scattering length, we perform this parameter optimization using *scikit-learn*'s `GaussianProcessRegressor` object [161], with the L-BGFS-B minimization algorithm from `scipy.optimize.minimize` [200].

In Table E.1, we present the predictions of our GP models at regularly spaced temperature values, omitting temperatures that fall outside of the range of input data at each scattering length. We used our GP models to plot and compare ξ and Δ_E in the main text, however the spline fits described in § 3.4, from which we computed T^*, were computed on the input Δ_E estimates rather than the GP predictions. The fact that the computed T^* values also describe the disappearance of the GP predictions serves as a preliminary consistency check of our GP models.

T/ε_F	$1/(k_Fa) = 0.0$				$1/(k_Fa) = 0.1$				$1/(k_Fa) = 0.2$				$1/(k_Fa) = 0.3$			
	ξ	$\sigma_{\bar{\xi}}$	Δ	$\sigma_{\bar{\Delta}}$	ξ	$\sigma_{\bar{\xi}}$	Δ	$\sigma_{\bar{\Delta}}$	ξ	$\sigma_{\bar{\xi}}$	Δ	$\sigma_{\bar{\Delta}}$	ξ	$\sigma_{\bar{\xi}}$	Δ	$\sigma_{\bar{\Delta}}$
0.10	0.44	0.03	–	–	0.32	0.02	–	–	0.22	0.03	–	–	0.06	0.04	–	–
0.11	0.46	0.02	0.28	0.06	0.34	0.02	–	–	0.23	0.03	–	–	0.07	0.03	–	–
0.12	0.47	0.02	0.26	0.05	0.36	0.01	0.41	0.08	0.25	0.02	–	–	0.08	0.03	–	–
0.13	0.49	0.01	0.23	0.04	0.37	0.01	0.38	0.06	0.26	0.02	–	–	0.10	0.02	–	–
0.14	0.50	0.01	0.20	0.03	0.39	0.01	0.34	0.05	0.28	0.02	0.34	0.07	0.12	0.02	–	–
0.15	0.52	0.01	0.16	0.03	0.42	0.01	0.29	0.04	0.30	0.01	0.32	0.06	0.13	0.02	–	–
0.16	0.55	0.01	0.12	0.02	0.44	0.01	0.23	0.03	0.32	0.01	0.29	0.04	0.15	0.02	0.60	0.09
0.17	0.57	0.01	0.08	0.02	0.46	0.01	0.17	0.03	0.34	0.01	0.25	0.04	0.17	0.01	0.59	0.07
0.18	0.59	0.01	0.05	0.02	0.49	0.01	0.11	0.02	0.36	0.01	0.21	0.03	0.19	0.01	0.55	0.07
0.19	0.61	0.01	0.03	0.02	0.51	0.01	0.07	0.02	0.38	0.01	0.17	0.02	0.22	0.01	0.47	0.06
0.20	0.63	0.01	0.01	0.01	0.53	0.01	0.04	0.01	0.41	0.01	0.13	0.02	0.24	0.01	0.37	0.05
0.21	0.65	0.01	0.00	0.01	0.56	0.01	0.02	0.01	0.43	0.01	0.10	0.02	0.26	0.01	0.26	0.04
0.22	0.68	0.01	0.00	0.01	0.58	0.01	0.01	0.01	0.45	0.01	0.07	0.02	0.29	0.01	0.18	0.04
0.23	0.69	0.01	0.00	0.01	0.60	0.01	0.00	0.01	0.47	0.01	0.04	0.02	0.31	0.01	0.14	0.04
0.24	0.71	0.01	0.00	0.01	0.62	0.01	0.00	0.01	0.49	0.01	0.03	0.01	0.33	0.01	0.14	0.04
0.25	0.73	0.01	0.00	0.01	0.64	0.01	0.00	0.01	0.51	0.01	0.02	0.01	0.35	0.01	0.14	0.03
0.26	0.74	0.01	0.00	0.01	0.65	0.01	0.00	0.01	0.53	0.01	0.02	0.01	0.37	0.01	0.13	0.03
0.27	0.75	0.01	0.00	0.01	0.67	0.01	0.00	0.01	0.55	0.01	0.02	0.01	0.40	0.01	0.10	0.03
0.28	0.76	0.02	0.00	0.01	0.69	0.01	0.00	0.01	0.57	0.01	0.01	0.01	0.42	0.01	0.07	0.03
0.29	0.77	0.02	0.00	0.01	0.71	0.01	0.00	0.01	0.59	0.01	0.01	0.01	0.45	0.01	0.05	0.02
0.30	0.77	0.03	0.00	0.02	0.72	0.01	0.00	0.01	0.61	0.01	0.01	0.01	0.47	0.01	0.05	0.02

Table E.1: Predictions of the Gaussian process regressors for ξ and Δ. $\sigma_{\bar{x}}$ denotes the standard error of the mean of x.

Appendix F

CHIRAL TWO-BODY INTERACTIONS

In this appendix, we detail some rather tedious calculations of two-body chiral interaction terms used in Chapter 4. These expressions are not integral to understanding the results of this dissertation but would be helpful to a researcher implementing chiral interaction terms in computer simulations. The goal in each case is to obtain expressions that depend on products of the elements of the momentum-space one-body density matrix, which is readily computed in AFQMC methods. Throughout this appendix we use $\mathcal{V}$ to refer to the system volume, to distinguish from any interaction terms like $V(q)$. In general, we consider the diagram in Fig. F.1, with incoming (outgoing) momenta p_1, p_2 (k_1, k_2) and incoming (outgoing) spins λ_1, λ_2 (ρ_1, ρ_2).

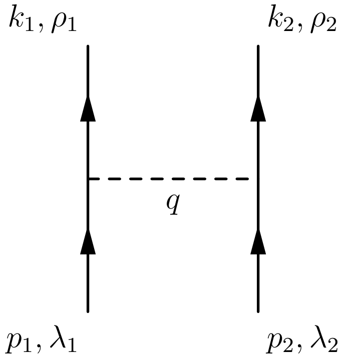

Figure F.1: Feynman diagram for a two-body nucleon-nucleon interaction

Conservation of momentum requires $q = p_1 - k_1$ and $p_1 + p_2 = k_1 + k_2$. In general, given a potential $V_{\lambda_1\lambda_2\rho_1\rho_2}(k_1, k_2, p_1, p_2)$ in a simulation volume $\mathcal{V}$, we have

$$V = \frac{1}{2\mathcal{V}} \sum_{\substack{\lambda_1\lambda_2\\ \rho_1\rho_2}} \sum_{\substack{k_1k_2\\ p_1p_2}} V_{\lambda_1\lambda_2\rho_1\rho_2}(k_1,k_2,p_1,p_2)$$

$$\times \Big[n_{\rho_1\lambda_1}(k_1,p_1)n_{\rho_2\lambda_2}(k_2,p_2) - n_{\rho_2\lambda_1}(k_2,p_1)n_{\rho_1\lambda_2}(k_1,p_2)\Big]. \quad \text{(F.1)}$$

In our case, the density matrix has the form

$$n = \begin{bmatrix} n_\uparrow & 0 \\ 0 & n_\downarrow \end{bmatrix}, \quad \text{(F.2)}$$

so we can write Eq. (F.1) as

$$V = \frac{1}{2\mathcal{V}} \sum_{\substack{\lambda_1\lambda_2\\ \rho_1\rho_2}} \sum_{\substack{k_1k_2\\ p_1p_2}} V_{\lambda_1\lambda_2\rho_1\rho_2}(k_1,k_2,p_1,p_2)$$

$$\times \Big[\delta_{\lambda_1\rho_1}\delta_{\lambda_2\rho_2} n_{\lambda_1}(k_1,p_1)n_{\lambda_2}(k_2,p_2) - \delta_{\lambda_1\rho_2}\delta_{\lambda_2\rho_1} n_{\lambda_1}(k_2,p_1)n_{\lambda_2}(k_1,p_2)\Big], \quad \text{(F.3)}$$

where δ_{ij} is the Kronecker delta.

F.1 General forms of the potential $V_{\lambda_1\lambda_2\rho_1\rho_2}(k_1,k_2,p_1,p_2)$

In the following sections, we will look at the different forms that can be found in $V_{\lambda_1\lambda_2\rho_1\rho_2}(k_1,k_2,p_1,p_2)$.

F.1.1 Constant terms

For terms like $V = C\delta_{\lambda_1\rho_1}\delta_{\lambda_2\rho_2}$, where C is a constant of the momenta and the spins,

$$V = \frac{1}{2\mathcal{V}} C \sum_{\substack{k_1k_2\\ p_1p_2}} \sum_{\lambda_1\lambda_2} \Big[\delta_{\lambda_1\lambda_1}\delta_{\lambda_2\lambda_2} n_{\lambda_1}(k_1,p_1)n_{\lambda_2}(k_2,p_2) - \delta_{\lambda_1\lambda_2}\delta_{\lambda_2\lambda_1} n_{\lambda_1}(k_2,p_1)n_{\lambda_2}(k_1,p_2)\Big] \quad \text{(F.4)}$$

$$= \frac{1}{2\mathcal{V}} C \sum_{\substack{k_1k_2\\ p_1p_2}} \Big[n_\uparrow(k_1,p_1)n_\uparrow(k_2,p_2) + n_\uparrow(k_1,p_1)n_\downarrow(k_2,p_2) + n_\downarrow(k_1,p_1)n_\uparrow(k_2,p_2)$$

$$+ n_\downarrow(k_1,p_1)n_\downarrow(k_2,p_2) - n_\uparrow(k_2,p_1)n_\uparrow(k_1,p_2) - n_\downarrow(k_2,p_1)n_\downarrow(k_1,p_2)\Big]. \quad \text{(F.5)}$$

For the subtracted terms, we can exchange the labels $k_1 \leftrightarrow k_2$. This yields

$$V = \frac{1}{2\mathcal{V}} C \sum_{\substack{k_1 k_2 \\ p_1 p_2}} \Big[n_\uparrow(k_1,p_1) n_\uparrow(k_2,p_2) + n_\uparrow(k_1,p_1) n_\downarrow(k_2,p_2) + n_\downarrow(k_1,p_1) n_\uparrow(k_2,p_2) + n_\downarrow(k_1,p_1) n_\downarrow(k_2,p_2) - n_\uparrow(k_1,p_1) n_\uparrow(k_2,p_2) - n_\downarrow(k_1,p_1) n_\downarrow(k_2,p_2) \Big] \tag{F.6}$$

$$V = \frac{1}{2\mathcal{V}} C \sum_{\substack{k_1 k_2 \\ p_1 p_2}} \Big[n_\uparrow(k_1,p_1) n_\downarrow(k_2,p_2) + n_\downarrow(k_1,p_1) n_\uparrow(k_2,p_2) \Big]. \tag{F.7}$$

F.1.2 Terms like $A(q)$

For terms like $V = A(q)\delta_{\lambda_1\rho_1}\delta_{\lambda_2\rho_2}$ we have

$$V = \frac{1}{2\mathcal{V}} \sum_{\substack{k_1 k_2 \\ p_1 p_2}} A(q) \sum_{\lambda_1 \lambda_2} \Big[\delta_{\lambda_1\lambda_1}\delta_{\lambda_2\lambda_2} n_{\lambda_1}(k_1,p_1) n_{\lambda_2}(k_2,p_2) - \delta_{\lambda_1\lambda_2}\delta_{\lambda_2\lambda_1} n_{\lambda_1}(k_2,p_1) n_{\lambda_2}(k_1,p_2) \Big] \tag{F.8}$$

$$= \frac{1}{2\mathcal{V}} \sum_{\substack{k_1 k_2 \\ p_1 p_2}} A(q) \Big[n_\uparrow(k_1,p_1) n_\uparrow(k_2,p_2) + n_\uparrow(k_1,p_1) n_\downarrow(k_2,p_2) + n_\downarrow(k_1,p_1) n_\uparrow(k_2,p_2) + n_\downarrow(k_1,p_1) n_\downarrow(k_2,p_2) - n_\uparrow(k_2,p_1) n_\uparrow(k_1,p_2) - n_\downarrow(k_2,p_1) n_\downarrow(k_1,p_2) \Big]. \tag{F.9}$$

For the subtracted terms, we can exchange the labels $k_1 \leftrightarrow k_2$. This yields

$$V = \frac{1}{2\mathcal{V}} \sum_{\substack{k_1 k_2 \\ p_1 p_2}} \Big[A(q) - A(\widetilde{q}) \Big] \Big[n_\uparrow(k_1,p_1) n_\uparrow(k_2,p_2) + n_\downarrow(k_1,p_1) n_\downarrow(k_2,p_2) \Big] + A(q) \Big[n_\uparrow(k_1,p_1) n_\downarrow(k_2,p_2) + n_\downarrow(k_1,p_1) n_\uparrow(k_2,p_2) \Big], \tag{F.10}$$

where $\widetilde{q} \equiv p_1 - k_2$.

If $A(q)$ depends only on the magnitude of q, e.g. $A(q^2)$, then we may write

$$V = \frac{1}{2\mathcal{V}} \sum_{\substack{k_1 k_2 \\ p_1 p_2}} \Big[A(q) - A(\widetilde{q}) \Big] \times \Big[n_\uparrow(k_1,p_1) n_\uparrow(k_2,p_2) + 2 n_\uparrow(k_1,p_1) n_\downarrow(k_2,p_2) + n_\downarrow(k_1,p_1) n_\downarrow(k_2,p_2) \Big]. \tag{F.11}$$

F.1.3 Terms like $B(q)(\sigma_1 \cdot q)(\sigma_2 \cdot q)$

For terms like $V = B(q)(\sigma_1 \cdot q)(\sigma_2 \cdot q)$ we have

$$\begin{aligned}
V &= \frac{1}{2\mathcal{V}} \sum_{\substack{k_1 k_2 \\ p_1 p_2}} B(q) \sum_{\substack{\lambda_1 \lambda_2 \\ \rho_1 \rho_2}} (\sigma^a_{\lambda_1 \rho_1} q_a)(\sigma^b_{\lambda_2 \rho_2} q_b) \times \\
&\qquad \Big[\delta_{\lambda_1 \rho_1} \delta_{\lambda_2 \rho_2} n_{\lambda_1}(k_1, p_1) n_{\lambda_2}(k_2, p_2) - \delta_{\lambda_1 \rho_2} \delta_{\lambda_2 \rho_1} n_{\lambda_1}(k_2, p_1) n_{\lambda_2}(k_1, p_2) \Big] \quad \text{(F.12)} \\
V &= \frac{1}{2\mathcal{V}} \sum_{\substack{k_1 k_2 \\ p_1 p_2}} B(q) \underbrace{\sum_{\lambda_1 \lambda_2} (\sigma^a_{\lambda_1 \lambda_1} q_a)(\sigma^b_{\lambda_2 \lambda_2} q_b) \Big[n_{\lambda_1}(k_1, p_1) n_{\lambda_2}(k_2, p_2) \Big]}_{D} \\
&\qquad - \underbrace{\sum_{\lambda_1 \lambda_2} (\sigma^a_{\lambda_1 \lambda_2} q_a)(\sigma^b_{\lambda_2 \lambda_1} q_b) \Big[n_{\lambda_1}(k_2, p_1) n_{\lambda_2}(k_1, p_2) \Big]}_{E} . \quad \text{(F.13)}
\end{aligned}$$

For direct term D, only the diagonal elements of the σ matrices contribute. Thus, only σ_z contributes to the dot product.

$$\begin{aligned}
D &= \sum_{\lambda_1 \lambda_2} (\sigma^{(z)}_{\lambda_1 \lambda_1} q_z)(\sigma^{(z)}_{\lambda_2 \lambda_2} q_z) \Big[n_{\lambda_1}(k_1, p_1) n_{\lambda_2}(k_2, p_2) \Big] \quad \text{(F.14)} \\
&= q_z^2 \Big[n_\uparrow(k_1, p_1) n_\uparrow(k_2, p_2) - n_\uparrow(k_1, p_1) n_\downarrow(k_2, p_2) \\
&\qquad - n_\downarrow(k_1, p_1) n_\uparrow(k_2, p_2) + n_\downarrow(k_1, p_1) n_\downarrow(k_2, p_2) \Big] . \quad \text{(F.15)}
\end{aligned}$$

For the exchange term E, we must consider the contribution from each of σ_x, σ_y, σ_z.

$$\begin{aligned}
E &= \sum_{\lambda_1 \lambda_2} (\sigma^a_{\lambda_1 \lambda_2} q_a)(\sigma^b_{\lambda_2 \lambda_1} q_b) \Big[n_{\lambda_1}(k_2, p_1) n_{\lambda_2}(k_1, p_2) \Big] \quad \text{(F.16)} \\
&= q_z^2 n_\uparrow(k_2, p_1) n_\uparrow(k_1, p_2) + q_z^2 n_\downarrow(k_2, p_1) n_\downarrow(k_1, p_2) \\
&\quad + (q_x + i q_y)(q_x - i q_y) n_\uparrow(k_2, p_1) n_\downarrow(k_1, p_2) \\
&\quad + (q_x - i q_y)(q_x + i q_y) n_\downarrow(k_2, p_1) n_\uparrow(k_1, p_2) \quad \text{(F.17)} \\
&= q_z^2 \left[n_\uparrow(k_2, p_1) n_\uparrow(k_1, p_2) + n_\downarrow(k_2, p_1) n_\downarrow(k_1, p_2) \right] \\
&\quad + \left[q_x^2 + q_y^2 \right] \left[n_\uparrow(k_2, p_1) n_\downarrow(k_1, p_2) + n_\downarrow(k_2, p_1) n_\uparrow(k_1, p_2) \right] . \quad \text{(F.18)}
\end{aligned}$$

For the exchange terms, we can again swap the labels $k_1 \leftrightarrow k_2$ in the sum over momenta.

This yields

$$\frac{1}{2\mathcal{V}}\sum_{\substack{k_1k_2\\p_1p_2}} B(q)\Big[q_z^2\left[n_\uparrow(k_2,p_1)n_\uparrow(k_1,p_2)+n_\downarrow(k_2,p_1)n_\downarrow(k_1,p_2)\right]$$

$$+\left[q_x^2+q_y^2\right]\left[n_\uparrow(k_2,p_1)n_\downarrow(k_1,p_2)+n_\downarrow(k_2,p_1)n_\uparrow(k_1,p_2)\right]\Big] \tag{F.19}$$

$$=\frac{1}{2\mathcal{V}}\sum_{\substack{k_1k_2\\p_1p_2}} B(\widetilde{q})\Big[\widetilde{q}_z^2\left[n_\uparrow(k_1,p_1)n_\uparrow(k_2,p_2)+n_\downarrow(k_1,p_1)n_\downarrow(k_2,p_2)\right]$$

$$+\left[\widetilde{q}_x^2+\widetilde{q}_y^2\right]\left[n_\uparrow(k_1,p_1)n_\downarrow(k_2,p_2)+n_\downarrow(k_1,p_1)n_\uparrow(k_2,p_2)\right]\Big], \tag{F.20}$$

where $\widetilde{q}\equiv p_1-k_2$. We can now combine the direct and exchange terms to get

$$V=\frac{1}{2\mathcal{V}}\sum_{\substack{k_1k_2\\p_1p_2}}\Bigg\{\Big[q_z^2B(q)-\widetilde{q}_z^2B(\widetilde{q})\Big]\Big[n_\uparrow(k_1,p_1)n_\uparrow(k_2,p_2)+n_\downarrow(k_1,p_1)n_\downarrow(k_2,p_2)\Big]$$

$$-\Big[q_z^2B(q)+\left(\widetilde{q}_x^2+\widetilde{q}_y^2\right)B(\widetilde{q})\Big]\Big[n_\uparrow(k_1,p_1)n_\downarrow(k_2,p_2)+n_\downarrow(k_1,p_1)n_\uparrow(k_2,p_2)\Big]\Bigg\}. \tag{F.21}$$

As before, if $B(q)$ depends only on the magnitude of q, e.g. $B(q^2)$, then we may write

$$V=\frac{1}{2\mathcal{V}}\sum_{\substack{k_1k_2\\p_1p_2}}\Bigg\{\Big[q_z^2B(q)-\widetilde{q}_z^2B(\widetilde{q})\Big]\Big[n_\uparrow(k_1,p_1)n_\uparrow(k_2,p_2)+n_\downarrow(k_1,p_1)n_\downarrow(k_2,p_2)\Big]$$

$$-2\Big[q_z^2B(q)+\left(\widetilde{q}_x^2+\widetilde{q}_y^2\right)B(\widetilde{q})\Big]n_\uparrow(k_1,p_1)n_\downarrow(k_2,p_2)\Bigg\}. \tag{F.22}$$

F.1.4 Terms like $D(q)(\sigma_1 \cdot \sigma_2)$

For terms like $V = D(q)(\sigma_1 \cdot \sigma_2)$ we have

$$V = \frac{1}{2\mathcal{V}} \sum_{\substack{k_1 k_2 \\ p_1 p_2}} D(q) \sum_{\substack{\lambda_1\lambda_2 \\ \rho_1\rho_2}} (\sigma^a_{\lambda_1\rho_1} \sigma_{\lambda_2\rho_2 a}) \times \Big[\delta_{\lambda_1\rho_1}\delta_{\lambda_2\rho_2} n_{\lambda_1}(k_1,p_1) n_{\lambda_2}(k_2,p_2) - \delta_{\lambda_1\rho_2}\delta_{\lambda_2\rho_1} n_{\lambda_1}(k_2,p_1) n_{\lambda_2}(k_1,p_2)\Big] \tag{F.23}$$

$$V = \frac{1}{2\mathcal{V}} \sum_{\substack{k_1 k_2 \\ p_1 p_2}} D(q) \underbrace{\sum_{\lambda_1\lambda_2} (\sigma^a_{\lambda_1\lambda_1} \sigma_{\lambda_2\lambda_2 a}) \Big[n_{\lambda_1}(k_1,p_1) n_{\lambda_2}(k_2,p_2)\Big]}_{D} - \underbrace{\sum_{\lambda_1\lambda_2} (\sigma^a_{\lambda_1\lambda_2} \sigma_{\lambda_2\lambda_1 a}) \Big[n_{\lambda_1}(k_2,p_1) n_{\lambda_2}(k_1,p_2)\Big]}_{E} . \tag{F.24}$$

For direct term D, only the diagonal elements of the σ matrices contribute. Thus, only σ_z contributes to the dot product.

$$D = \sum_{\lambda_1\lambda_2} (\sigma^{(z)}_{\lambda_1\lambda_1} \sigma^{(z)}_{\lambda_2\lambda_2}) \Big[n_{\lambda_1}(k_1,p_1) n_{\lambda_2}(k_2,p_2)\Big] \tag{F.25}$$

$$= \Big[n_\uparrow(k_1,p_1)n_\uparrow(k_2,p_2) - n_\uparrow(k_1,p_1)n_\downarrow(k_2,p_2) - n_\downarrow(k_1,p_1)n_\uparrow(k_2,p_2) + n_\downarrow(k_1,p_1)n_\downarrow(k_2,p_2)\Big]. \tag{F.26}$$

For the exchange term E, we must consider the contribution from each of σ_x, σ_y, σ_z.

$$E = \sum_{\lambda_1\lambda_2} (\sigma^a_{\lambda_1\lambda_2} \sigma_{\lambda_2\lambda_1 a}) \Big[n_{\lambda_1}(k_2,p_1) n_{\lambda_2}(k_1,p_2)\Big] \tag{F.27}$$

$$= n_\uparrow(k_2,p_1)n_\uparrow(k_1,p_2) + n_\downarrow(k_2,p_1)n_\downarrow(k_1,p_2) + (1+i)(1-i)\, n_\uparrow(k_2,p_1)n_\downarrow(k_1,p_2) + (1-i)(1+i)\, n_\downarrow(k_2,p_1)n_\uparrow(k_1,p_2) \tag{F.28}$$

$$= [n_\uparrow(k_2,p_1)n_\uparrow(k_1,p_2) + n_\downarrow(k_2,p_1)n_\downarrow(k_1,p_2)] + 2\,[n_\uparrow(k_2,p_1)n_\downarrow(k_1,p_2) + n_\downarrow(k_2,p_1)n_\uparrow(k_1,p_2)] . \tag{F.29}$$

For the exchange terms, we can again swap the labels $k_1 \leftrightarrow k_2$ in the sum over momenta.

This yields

$$\begin{aligned}
&\frac{1}{2\mathcal{V}}\sum_{\substack{k_1k_2\\p_1p_2}} D(q)\Big[\,[n_\uparrow(k_2,p_1)n_\uparrow(k_1,p_2)+n_\downarrow(k_2,p_1)n_\downarrow(k_1,p_2)]\\
&\qquad\qquad+2\,[n_\uparrow(k_2,p_1)n_\downarrow(k_1,p_2)+n_\downarrow(k_2,p_1)n_\uparrow(k_1,p_2)]\,\Big] \qquad \text{(F.30)}\\
&=\frac{1}{2\mathcal{V}}\sum_{\substack{k_1k_2\\p_1p_2}} D(\widetilde{q})\Big[\,[n_\uparrow(k_1,p_1)n_\uparrow(k_2,p_2)+n_\downarrow(k_1,p_1)n_\downarrow(k_2,p_2)]\\
&\qquad\qquad+2\,[n_\uparrow(k_1,p_1)n_\downarrow(k_2,p_2)+n_\downarrow(k_1,p_1)n_\uparrow(k_2,p_2)]\,\Big], \qquad \text{(F.31)}
\end{aligned}$$

where $\widetilde{q} \equiv p_1 - k_2$. We can now combine the direct and exchange terms to get

$$\begin{aligned}
V=\frac{1}{2\mathcal{V}}\sum_{\substack{k_1k_2\\p_1p_2}}\Bigg\{&\Big[D(q)-D(\widetilde{q})\Big]\Big[n_\uparrow(k_1,p_1)n_\uparrow(k_2,p_2)+n_\downarrow(k_1,p_1)n_\downarrow(k_2,p_2)\Big]\\
&-\Big[D(q)+2D(\widetilde{q})\Big]\Big[n_\uparrow(k_1,p_1)n_\downarrow(k_2,p_2)+n_\downarrow(k_1,p_1)n_\uparrow(k_2,p_2)\Big]\Bigg\}. \qquad \text{(F.32)}
\end{aligned}$$

And as usual, if $D(q)$ depends only on the magnitude of q, e.g. $D(q^2)$, then we may write

$$\begin{aligned}
V=\frac{1}{2\mathcal{V}}\sum_{\substack{k_1k_2\\p_1p_2}}\Bigg\{&\Big[D(q)-D(\widetilde{q})\Big]\Big[n_\uparrow(k_1,p_1)n_\uparrow(k_2,p_2)+n_\downarrow(k_1,p_1)n_\downarrow(k_2,p_2)\Big]\\
&-2\Big[D(q)+2D(\widetilde{q})\Big]n_\uparrow(k_1,p_1)n_\downarrow(k_2,p_2)\Bigg\}. \qquad \text{(F.33)}
\end{aligned}$$

F.1.5 Terms like $F(q)\,[-iS\cdot(q\times\widetilde{q})]$

For terms like $V = F(q)\,[-iS\cdot(q\cdot\widetilde{q})]$, where $S \equiv \frac{1}{2}(\sigma_1+\sigma_2)$ we have

$$\begin{aligned} V = \frac{1}{2\mathcal{V}} \sum_{\substack{k_1k_2\\p_1p_2}} F(q) \sum_{\substack{\lambda_1\lambda_2\\\rho_1\rho_2}} \frac{-i}{2}\left(\sigma^i_{\lambda_1\rho_1}\delta_{\lambda_2\rho_2} + \sigma^i_{\lambda_2\rho_2}\delta_{\lambda_1\rho_1}\right) q^j\widetilde{q}^k\epsilon_{ijk}\times \\ \Big[\delta_{\lambda_1\rho_1}\delta_{\lambda_2\rho_2}n_{\lambda_1}(k_1,p_1)n_{\lambda_2}(k_2,p_2) - \delta_{\lambda_1\rho_2}\delta_{\lambda_2\rho_1}n_{\lambda_1}(k_2,p_1)n_{\lambda_2}(k_1,p_2)\Big] \end{aligned} \tag{F.34}$$

$$\begin{aligned} V = \frac{1}{2\mathcal{V}} \sum_{\substack{k_1k_2\\p_1p_2}} F(q) \underbrace{\sum_{\lambda_1\lambda_2} \frac{-i}{2}\left(\sigma^i_{\lambda_1\lambda_1} + \sigma^i_{\lambda_2\lambda_2}\right) q^j\widetilde{q}^k\epsilon_{ijk}\Big[n_{\lambda_1}(k_1,p_1)n_{\lambda_2}(k_2,p_2)\Big]}_{D} \\ - \underbrace{\sum_{\lambda_1\lambda_2} \frac{-i}{2}\left(\sigma^i_{\lambda_1\lambda_2}\delta_{\lambda_1\lambda_2} + \sigma^i_{\lambda_2\lambda_1}\delta_{\lambda_1\lambda_2}\right) q^j\widetilde{q}^k\epsilon_{ijk}\Big[n_{\lambda_1}(k_2,p_1)n_{\lambda_2}(k_1,p_2)\Big]}_{E}\,. \end{aligned} \tag{F.35}$$

For direct term D, only the diagonal elements of the σ matrices contribute. Thus, only σ_z contributes to the scalar triple product.

$$D = \sum_{\lambda_1\lambda_2} \frac{-i}{2}\left(\sigma^{(z)}_{\lambda_1\lambda_1} + \sigma^{(z)}_{\lambda_2\lambda_2}\right)(q_x\widetilde{q}_y - q_y\widetilde{q}_x)\Big[n_{\lambda_1}(k_1,p_1)n_{\lambda_2}(k_2,p_2)\Big] \tag{F.36}$$

$$= -i\,(q_x\widetilde{q}_y - q_y\widetilde{q}_x)\Big[n_\uparrow(k_1,p_1)n_\uparrow(k_2,p_2) - n_\downarrow(k_1,p_1)n_\downarrow(k_2,p_2)\Big]. \tag{F.37}$$

For the exchange term E, the delta function will eliminate contributions from σ_x and σ_y so again we can consider only the contribution from σ_z.

$$E = \sum_{\lambda_1\lambda_2} \frac{-i}{2}\left(\sigma^i_{\lambda_1\lambda_2} + \sigma^i_{\lambda_2\lambda_1}\right)\delta_{\lambda_1\lambda_2} q^j\widetilde{q}^k\epsilon_{ijk}\Big[n_{\lambda_1}(k_2,p_1)n_{\lambda_2}(k_1,p_2)\Big] \tag{F.38}$$

$$= \sum_{\lambda_1\lambda_2}\left\{\frac{-i}{2}\left(\sigma^{(z)}_{\lambda_1\lambda_2} + \sigma^{(z)}_{\lambda_2\lambda_1}\right)(q_x\widetilde{q}_y - q_y\widetilde{q}_x)\Big[n_{\lambda_1}(k_2,p_1)n_{\lambda_2}(k_1,p_2)\Big]\right\} \tag{F.39}$$

$$= -i\,(q_x\widetilde{q}_y - q_y\widetilde{q}_x)\left[n_\uparrow(k_2,p_1)n_\uparrow(k_1,p_2) - n_\downarrow(k_2,p_1)n_\downarrow(k_1,p_2)\right]. \tag{F.40}$$

For the exchange terms, we can again swap the labels $k_1 \leftrightarrow k_2$ in the sum over momenta. This yields

$$\frac{1}{2\mathcal{V}} \sum_{\substack{k_1k_2\\p_1p_2}} F(q)E = \frac{-i}{2\mathcal{V}} \sum_{\substack{k_1k_2\\p_1p_2}} F(\widetilde{q})\Big\{\,(\widetilde{q}_xq_y - \widetilde{q}_yq_x)\left[n_\uparrow(k_1,p_1)n_\uparrow(k_2,p_2) - n_\downarrow(k_1,p_1)n_\downarrow(k_2,p_2)\right]\Big\}, \tag{F.41}$$

where $\widetilde{q} \equiv p_1 - k_2$. We can now combine the direct and exchange terms to get

$$V = \frac{-i}{2\mathcal{V}} \sum_{\substack{k_1 k_2 \\ p_1 p_2}} \left\{ \left[F(q) + F(\widetilde{q})\right] \left(q_x \widetilde{q}_y - q_y \widetilde{q}_x\right) \Big[n_\uparrow(k_1, p_1) n_\uparrow(k_2, p_2) - n_\downarrow(k_1, p_1) n_\downarrow(k_2, p_2) \Big] \right\}. \tag{F.42}$$

If $n \equiv n_\uparrow = n_\downarrow$, then this term vanishes entirely.

F.1.6 Terms like $G(q)\sigma_1 \cdot (q \times \widetilde{q})\, \sigma_2 \cdot (q \times \widetilde{q})$

For terms like $G(q)\sigma_1 \cdot (q \times \widetilde{q})\, \sigma_2 \cdot (q \times \widetilde{q})$, we have

$$V = \frac{1}{2\mathcal{V}} \sum_{\substack{k_1 k_2 \\ p_1 p_2}} G(q) \sum_{\substack{\lambda_1 \lambda_2 \\ \rho_1 \rho_2}} \left(\sigma^i_{\lambda_1 \rho_1} q^j \widetilde{q}^k \epsilon_{ijk} \sigma^\ell_{\lambda_2 \rho_2} q^m \widetilde{q}^n \epsilon_{\ell mn} \right) \times$$
$$\Big[\delta_{\lambda_1 \rho_1} \delta_{\lambda_2 \rho_2} n_{\lambda_1}(k_1, p_1) n_{\lambda_2}(k_2, p_2) - \delta_{\lambda_1 \rho_2} \delta_{\lambda_2 \rho_1} n_{\lambda_1}(k_2, p_1) n_{\lambda_2}(k_1, p_2) \Big] \tag{F.43}$$

$$V = \frac{1}{2\mathcal{V}} \sum_{\substack{k_1 k_2 \\ p_1 p_2}} F(q)\, \underbrace{\sigma^i_{\lambda_1 \lambda_1} q^j \widetilde{q}^k \epsilon_{ijk} \sigma^\ell_{\lambda_2 \lambda_2} q^m \widetilde{q}^n \epsilon_{\ell mn} n_{\lambda_1}(k_1, p_1) n_{\lambda_2}(k_2, p_2)}_{D}$$
$$- \underbrace{\sigma^i_{\lambda_1 \lambda_2} q^j \widetilde{q}^k \epsilon_{ijk} \sigma^\ell_{\lambda_2 \lambda_1} q^m \widetilde{q}^n \epsilon_{\ell mn} n_{\lambda_1}(k_1, p_1) n_{\lambda_2}(k_2, p_2)}_{E}. \tag{F.44}$$

For direct term D, only the diagonal elements of the σ matrices contribute. Thus, only σ_z contributes to the scalar triple product.

$$D = \sum_{\lambda_1 \lambda_2} \left(\sigma^{(z)}_{\lambda_1 \lambda_1} \sigma^{(z)}_{\lambda_2 \lambda_2} \right) \left(q_x \widetilde{q}_y - q_y \widetilde{q}_x\right)^2 \Big[n_{\lambda_1}(k_1, p_1) n_{\lambda_2}(k_2, p_2) \Big] \tag{F.45}$$

$$= \left(q_x \widetilde{q}_y - q_y \widetilde{q}_x\right)^2 \Big[n_\uparrow(k_1, p_1) n_\uparrow(k_2, p_2) - n_\uparrow(k_1, p_1) n_\downarrow(k_2, p_2)$$
$$- n_\downarrow(k_1, p_1) n_\uparrow(k_2, p_2) + n_\downarrow(k_1, p_1) n_\downarrow(k_2, p_2) \Big]. \tag{F.46}$$

For the exchange term E, we have contributions from σ_x, σ_y, and σ_z.

$$E = \sum_{\lambda_1 \lambda_2} \left(\sigma^i_{\lambda_1 \lambda_2} \sigma^j_{\lambda_2 \lambda_1} \right) (q \times \widetilde{q})_i\, (q \times \widetilde{q})_j \Big[n_{\lambda_1}(k_2, p_1) n_{\lambda_2}(k_1, p_2) \Big] \tag{F.47}$$

$$= (q \times \widetilde{q})_z^2 \left[n_\uparrow(k_2, p_1) n_\uparrow(k_1, p_2) + n_\downarrow(k_2, p_1) n_\downarrow(k_1, p_2) \right]$$
$$+ \Big[(q \times \widetilde{q})_x^2 + (q \times \widetilde{q})_y^2 \Big] \left[n_\uparrow(k_2, p_1) n_\downarrow(k_1, p_2) + n_\downarrow(k_2, p_1) n_\uparrow(k_1, p_2) \right]. \tag{F.48}$$

We can again swap the labels $k_1 \leftrightarrow k_2$ in the sum over momenta. This yields

$$\frac{1}{2\mathcal{V}}\sum_{\substack{k_1k_2\\p_1p_2}} G(q)E = \frac{1}{2\mathcal{V}}\sum_{\substack{k_1k_2\\p_1p_2}} G(\widetilde{q})\Bigg\{ (q\times\widetilde{q})_z^2\left[n_\uparrow(k_2,p_1)n_\uparrow(k_1,p_2)+n_\downarrow(k_2,p_1)n_\downarrow(k_1,p_2)\right] \\ + \left[(q\times\widetilde{q})_x^2+(q\times\widetilde{q})_y^2\right]\left[n_\uparrow(k_2,p_1)n_\downarrow(k_1,p_2)+n_\downarrow(k_2,p_1)n_\uparrow(k_1,p_2)\right]\Bigg\}, \tag{F.49}$$

where $\widetilde{q} \equiv p_1 - k_2$. We can now combine the direct and exchange terms to get

$$V = \frac{1}{2\mathcal{V}}\sum_{\substack{k_1k_2\\p_1p_2}} \left[G(q)-G(\widetilde{q})\right](q\times\widetilde{q})_z^2\Big[n_\uparrow(k_1,p_1)n_\uparrow(k_2,p_2)+n_\downarrow(k_1,p_1)n_\downarrow(k_2,p_2)\Big] \\ - \Big[G(q)\,(q\times\widetilde{q})_z^2+G(\widetilde{q})\left((q\times\widetilde{q})_x^2+(q\times\widetilde{q})_y^2\right)\Big] \\ \times\Big[n_\uparrow(k_1,p_1)n_\downarrow(k_2,p_2)+n_\downarrow(k_1,p_1)n_\uparrow(k_2,p_2)\Big]. \tag{F.50}$$

If $G \equiv G(q) = G(\widetilde{q})$, then the direct term vanishes and we have

$$V = \frac{1}{2\mathcal{V}}\sum_{\substack{k_1k_2\\p_1p_2}} -G\,(q\times\widetilde{q})^2\Big[n_\uparrow(k_1,p_1)n_\downarrow(k_2,p_2)+n_\downarrow(k_1,p_1)n_\uparrow(k_2,p_2)\Big]. \tag{F.51}$$

F.2 Chiral contributions

We now apply the general expressions of the previous section to the chiral interaction terms provided in Ref. [135], while referring the reader there for the values of low energy constants like C_S, C_T, etc.

F.2.1 LO Contributions

Contact term

At leading order the contact term in momentum space is [135]

$$V^c_{LO} = \left[C_S + C_T\sigma_1\cdot\sigma_2\right]. \tag{F.52}$$

So the contact term is the sum of a constant term (use Eq. (F.7)) and a term with $\sigma_1 \cdot \sigma_2$ (use Eq. (F.32)). Thus,

$$\begin{aligned} V^c_{LO} = \frac{1}{2\mathcal{V}} \sum_{\substack{k_1k_2\\p_1p_2}} \Bigg\{ & C_S\Big[n_\uparrow(k_1,p_1)n_\downarrow(k_2,p_2) + n_\downarrow(k_1,p_1)n_\uparrow(k_2,p_2)\Big] \\ & + \Big[C_T(q) - C_T(\widetilde{q})\Big]\Big[n_\uparrow(k_1,p_1)n_\uparrow(k_2,p_2) + n_\downarrow(k_1,p_1)n_\downarrow(k_2,p_2)\Big] \\ & - \Big[C_T(q) + 2C_T(\widetilde{q})\Big]\Big[n_\uparrow(k_1,p_1)n_\downarrow(k_2,p_2) + n_\downarrow(k_1,p_1)n_\uparrow(k_2,p_2)\Big]\Bigg\}. \end{aligned} \tag{F.53}$$

But C_T is constant in momentum so this simplifies to

$$V^c_{LO} = \frac{1}{2\mathcal{V}} \sum_{\substack{k_1k_2\\p_1p_2}} \Bigg\{ \Big[C_S - 3C_T\Big]\Big[n_\uparrow(k_1,p_1)n_\downarrow(k_2,p_2) + n_\downarrow(k_1,p_1)n_\uparrow(k_2,p_2)\Big]\Bigg\} \tag{F.54}$$

$$\boxed{V^c_{LO} = \frac{1}{2\mathcal{V}} \sum_{\substack{k_1k_2\\p_1p_2}} \Bigg\{ \Big[2C_S - 6C_T\Big] n_\uparrow(k_1,p_1)n_\downarrow(k_2,p_2)\Bigg\}.} \tag{F.55}$$

If $n_\uparrow = n_\downarrow = n$ then this simplifies to

$$V^c_{LO} = \frac{1}{2\mathcal{V}} \sum_{\substack{k_1k_2\\p_1p_2}} \Bigg\{ \Big[2C_S - 6C_T\Big] n(k_1,p_1)n(k_2,p_2)\Bigg\}. \tag{F.56}$$

One-pion exchange

At leading order the one-pion exchange term in momentum space reads [135]

$$V_{1\pi}(q) \sim -\frac{g_A^2}{4f_\pi^2}\frac{1}{q^2+m_\pi^2}\left(\sigma_1\cdot q\right)\left(\sigma_2\cdot q\right), \tag{F.57}$$

This is of the form $B(q)(\sigma_1 \cdot q)(\sigma_2 \cdot q)$ and the potential depends only on q^2 so we can use Eq. (F.22).

$$\begin{aligned} V^{1\pi}_{LO} = \frac{1}{2\mathcal{V}} \sum_{\substack{k_1k_2\\p_1p_2}} \Bigg\{ & \Big[q_z^2B(q) - \widetilde{q}_z^2B(\widetilde{q})\Big]\Big[n_\uparrow(k_1,p_1)n_\uparrow(k_2,p_2) + n_\downarrow(k_1,p_1)n_\downarrow(k_2,p_2)\Big] \\ & - 2\Big[q_z^2B(q) + \left(\widetilde{q}_x^2 + \widetilde{q}_y^2\right)B(\widetilde{q})\Big]n_\uparrow(k_1,p_1)n_\downarrow(k_2,p_2)\Bigg\}, \end{aligned} \tag{F.58}$$

$$\text{where } B(q) \equiv -\frac{g_A^2}{4f_\pi^2}\frac{1}{q^2+m_\pi^2}. \tag{F.59}$$

If $n_\uparrow = n_\downarrow = n$, then this simplifies to

$$V_{LO}^{1\pi} = \frac{1}{2\mathcal{V}} \sum_{\substack{k_1 k_2 \\ p_1 p_2}} \Bigg\{ -2\widetilde{q}^2 B(\widetilde{q}) n(k_1, p_1) n(k_2, p_2) \Bigg\}. \tag{F.60}$$

F.2.2 NLO Contributions

Contact term

At NLO, the contact term in momentum space in the general reference system is

$$\begin{aligned} V_{NLO}^{c}(q, \widetilde{q}) = C_1 q^2 + \frac{C_2}{4}\widetilde{q}^2 + \left(C_3 q^2 + \frac{C_4}{4}\widetilde{q}^2 \right) (\sigma_1 \cdot \sigma_2) \\ + C_5 \left[-\frac{i}{2} S \cdot q \times \widetilde{q} \right] + C_6 (\sigma_1 \cdot q)(\sigma_2 \cdot q) + \frac{C_7}{4} (\sigma_1 \cdot \widetilde{q})(\sigma_2 \cdot \widetilde{q}) . \end{aligned} \tag{F.61}$$

This has terms of the forms $A(q)$, $B(q)(\sigma_1 \cdot q)(\sigma_2 \cdot q)$, $D(q)(\sigma_1 \cdot \sigma_2)$, and $F(q)\left[-iS \cdot (q \times \widetilde{q})\right]$, so we will use Eqs. (F.10), (F.21), (F.32) and (F.42).

Combining these equations and using the shorthand $q_\perp \equiv q_x^2 + q_y^2$ yields

$$\begin{aligned} V_{NLO}^{c} = \frac{1}{2\mathcal{V}} \sum_{\substack{k_1 k_2 \\ p_1 p_2}} \Bigg\{ \Big[(C_1 + C_3)\left(q^2 - \widetilde{q}^2\right) + \frac{C_2 + C_4}{4}\left(\widetilde{q}^2 - q^2\right) + \left(C_6 - \frac{C_7}{4} \right)\left(q_z^2 - \widetilde{q}_z^2\right) \Big] \\ \times \Big[n_\uparrow(k_1, p_1) n_\uparrow(k_2, p_2) + n_\downarrow(k_1, p_1) n_\downarrow(k_2, p_2) \Big] \\ + \left[C_1 q^2 + \frac{C_2}{4}\widetilde{q}^2 - C_3\left(q^2 + 2\widetilde{q}^2\right) - \frac{C_4}{4}\left(\widetilde{q}^2 + 2q^2\right) - C_6\left(q_z^2 + \widetilde{q}_\perp^2\right) - \frac{C_7}{4}\left(\widetilde{q}_z^2 + q_\perp^2\right) \right] \\ \times \Big[n_\uparrow(k_1, p_1) n_\downarrow(k_2, p_2) + n_\downarrow(k_1, p_1) n_\uparrow(k_2, p_2) \Big] \\ - \frac{iC_5}{2} \Big[(q_x \widetilde{q}_y - q_y \widetilde{q}_x) - (\widetilde{q}_x q_y - \widetilde{q}_y q_x) \Big] \Big[n_\uparrow(k_1, p_1) n_\uparrow(k_2, p_2) - n_\downarrow(k_1, p_1) n_\downarrow(k_2, p_2) \Big] \Bigg\}. \end{aligned} \tag{F.62}$$

Since the terms in front of $[n_\uparrow(k_1, p_1) n_\downarrow(k_2, p_2) + n_\downarrow(k_1, p_1) n_\uparrow(k_2, p_2)]$ are all the same under the simultaneous label swap $k_1 \leftrightarrow k_2$ and $p_1 \leftrightarrow p_2$, we can simplify to

$$\begin{aligned} V_{NLO}^{c} = \frac{1}{2\mathcal{V}} \sum_{\substack{k_1 k_2 \\ p_1 p_2}} \Bigg\{ & \Big[\left(C_1 + C_3\right)\left(q^2 - \widetilde{q}^2\right) + \frac{C_2 + C_4}{4}\left(\widetilde{q}^2 - q^2\right) + \left(C_6 - \frac{C_7}{4}\right)\left(q_z^2 - \widetilde{q}_z^2\right) \Big] \\ & \times \Big[n_\uparrow(k_1, p_1) n_\uparrow(k_2, p_2) + n_\downarrow(k_1, p_1) n_\downarrow(k_2, p_2) \Big] \\ & + \left[C_1 q^2 + \frac{C_2}{4}\widetilde{q}^2 - C_3\left(q^2 + 2\widetilde{q}^2\right) - \frac{C_4}{4}\left(\widetilde{q}^2 + 2q^2\right) - C_6\left(q_z^2 + \widetilde{q}_\perp^2\right) - \frac{C_7}{4}\left(\widetilde{q}_z^2 + q_\perp^2\right) \right] \\ & \times 2\Big[n_\uparrow(k_1, p_1) n_\downarrow(k_2, p_2) \Big] \\ & - iC_5 \Big[q_x \widetilde{q}_y - q_y \widetilde{q}_x \Big] \Big[n_\uparrow(k_1, p_1) n_\uparrow(k_2, p_2) - n_\downarrow(k_1, p_1) n_\downarrow(k_2, p_2) \Big] \Bigg\}. \end{aligned} \tag{F.63}$$

If $n_\uparrow = n_\downarrow = n$, then we have

$$\begin{aligned} V_{NLO}^{c} = \frac{1}{2\mathcal{V}} \sum_{\substack{k_1 k_2 \\ p_1 p_2}} \Bigg\{ & \Bigg[2C_1\left(2q^2 - \widetilde{q}^2\right) - \frac{C_2}{2}\left(q^2 - 2\widetilde{q}^2\right) - \left(6C_3 + 2C_6\right)\widetilde{q}^2 \\ & - \left(\frac{3}{2}C_4 + \frac{1}{2}C_7\right) q^2 \Bigg] \times \Big[n(k_1, p_1) n(k_2, p_2) \Big] \Bigg\}. \end{aligned} \tag{F.64}$$

Two-pion exchange

At NLO, the two-pion exchange term reads

$$V_{NLO}^{2\pi} = W_C(q) + V_S(q)\left(\sigma_1 \cdot \sigma_2\right) + V_T(q)\left(\sigma_1 \cdot q\right)\left(\sigma_2 \cdot q\right), \tag{F.65}$$

with

$$W_C(q) \equiv -\frac{L(q)}{384\pi^2 f_\pi^4} \left[4m_\pi^2 \left(5g_A^4 - 4g_A^2 - 1\right) + q^2\left(23g_A^4 - 10g_A^2 - 1\right) + \frac{48 g_A^4 m_\pi^4}{w^2} \right], \tag{F.66}$$

$$V_T = -\frac{1}{q^2} V_S = -\frac{3g_A^4 L(q)}{64\pi^2 f_\pi^4}, \tag{F.67}$$

where

$$L(q) \equiv \frac{w}{q} \ln \frac{w + q}{2m_\pi} \tag{F.68}$$

and

$$w \equiv \sqrt{4m_\pi^2 + q^2}. \tag{F.69}$$

This is a combination of terms of the form $A(q)$, $B(q)(\sigma_1 \cdot q)(\sigma_2 \cdot q)$, and $D(q)\,(\sigma_1 \cdot \sigma_2)$. Since $L(q)$ depends on q rather than q^2 we will use Eqs. (F.10), (F.21) and (F.32). Thus

$$\begin{aligned} V_{NLO}^{2\pi} = \frac{1}{2\mathcal{V}} \sum_{\substack{k_1 k_2 \\ p_1 p_2}} \Bigg\{ & \Big[W_C(q) + V_S(q) + V_T(q) q_z^2 - W_C(\widetilde{q}) - V_S(\widetilde{q}) - V_T(\widetilde{q})\widetilde{q}_z^2\Big] \\ & \times \Big[n_\uparrow(k_1,p_1)n_\uparrow(k_2,p_2) + n_\downarrow(k_1,p_1)n_\downarrow(k_2,p_2)\Big] \\ & + \Big[W_C(q) - V_S(q) - V_T(q)q_z^2 - 2V_S(\widetilde{q}) - V_T(\widetilde{q})\left(\widetilde{q}_x^2 + \widetilde{q}_y^2\right)\Big] \\ & \times \Big[n_\uparrow(k_1,p_1)n_\downarrow(k_2,p_2) + n_\downarrow(k_1,p_1)n_\uparrow(k_2,p_2)\Big] \Bigg\}. \end{aligned} \tag{F.70}$$

If $n_\uparrow = n_\downarrow = n$ then this simplifies to

$$V_{NLO}^{2\pi} = \frac{1}{2\mathcal{V}} \sum_{\substack{k_1 k_2 \\ p_1 p_2}} \left\{ 2\Big[2W_C(q) - W_C(\widetilde{q}) - 3V_S(\widetilde{q}) - V_T(\widetilde{q})\widetilde{q}^2\Big] n(k_1,p_1)n(k_2,p_2) \right\} \tag{F.71}$$

$$= \frac{1}{2\mathcal{V}} \sum_{\substack{k_1 k_2 \\ p_1 p_2}} \left\{ 2\Big[2W_C(q) - W_C(\widetilde{q}) - 2V_S(\widetilde{q})\Big] n(k_1,p_1)n(k_2,p_2) \right\}. \tag{F.72}$$

F.2.3 N^2LO Contributions

Contact term

At N^{2}LO, there are no new contact terms [135].

Two-pion exchange

At N^{2}LO, the two-pion exchange term reads [135]

$$V_{\mathrm{N^2LO}}^{2\pi} = U_C(q) + U_S(q)\,(\sigma_1 \cdot \sigma_2) + U_T(q)\,(\sigma_1 \cdot q)\,(\sigma_2 \cdot q) + U_{LS}(q)\left(-\frac{i}{2} S \cdot q \times \widetilde{q}\right), \tag{F.73}$$

with

$$U_X \equiv V_X + W_X, \quad X \in \{C, S, T, LS\}. \tag{F.74}$$

The functions V and W will be defined later but it is enough to note that they only depend on q.

As with the NLO two-pion exchange term we will use Eqs. (F.10), (F.21) and (F.32). And since we have an addition term of the form $F(q)\left[-iS\cdot(q\times\widetilde{q})\right]$, we will also use Eq. (F.42).

$$\begin{aligned}
V^{2\pi}_{\mathrm{N^2LO}} = \frac{1}{2\mathcal{V}}\sum_{\substack{k_1k_2\\p_1p_2}}\Bigg\{&\Big[U_C(q)+U_S(q)+U_T(q)q_z^2-U_C(\widetilde{q})-U_S(\widetilde{q})-U_T(\widetilde{q})\widetilde{q}_z^2\Big]\\
&\times\Big[n_\uparrow(k_1,p_1)n_\uparrow(k_2,p_2)+n_\downarrow(k_1,p_1)n_\downarrow(k_2,p_2)\Big]\\
&+\Big[U_C(q)-U_S(q)-U_T(q)q_z^2-2U_S(\widetilde{q})-U_T(\widetilde{q})\left(\widetilde{q}_x^2+\widetilde{q}_y^2\right)\Big]\\
&\times\Big[n_\uparrow(k_1,p_1)n_\downarrow(k_2,p_2)+n_\downarrow(k_1,p_1)n_\uparrow(k_2,p_2)\Big]\Bigg\}\\
+\frac{1}{2\mathcal{V}}\sum_{\substack{k_1k_2\\p_1p_2}}\Bigg\{&-\frac{i}{2}\left[U_{LS}(q)+U_{LS}(\widetilde{q})\right](q_x\widetilde{q}_y-q_y\widetilde{q}_x)\times\\
&\Big[n_\uparrow(k_1,p_1)n_\uparrow(k_2,p_2)-n_\downarrow(k_1,p_1)n_\downarrow(k_2,p_2)\Big]\Bigg\}.
\end{aligned}\tag{F.75}$$

If $n_\uparrow = n_\downarrow = n$, then this simplifies to

$$V^{2\pi}_{\mathrm{N^2LO}} = \frac{1}{2\mathcal{V}}\sum_{\substack{k_1k_2\\p_1p_2}}\Bigg\{\Big[4U_C(q)-2U_C(\widetilde{q})-6U_S(\widetilde{q})-2U_T(\widetilde{q})\widetilde{q}^2\Big]\Big[n(k_1,p_1)n(k_2,p_2)\Big]\Bigg\} \tag{F.76}$$

$$= \frac{1}{2\mathcal{V}}\sum_{\substack{k_1k_2\\p_1p_2}}\Bigg\{\Big[4U_C(q)-2U_C(\widetilde{q})-4U_S(\widetilde{q})\Big]\Big[n(k_1,p_1)n(k_2,p_2)\Big]\Bigg\}. \tag{F.77}$$

F.2.4 N^{3}LO Contributions

Contact term

At N^{3}LO, the contact term in momentum space in the general reference system is [135]

$$
\begin{aligned}
V^c_{\mathrm{N^3LO}}(q,\widetilde{q}) = {} & D_1 q^4 + \frac{D_2}{16}\widetilde{q}^4 + \frac{D_3}{4} q^2 \widetilde{q}^2 + \frac{D_4}{4}\left(q\times\widetilde{q}\right)^2 \\
& + \left(D_5 q^4 + \frac{D_6}{16}\widetilde{q}^4 + \frac{D_7}{4} q^2\widetilde{q}^2 + \frac{D_8}{4}\left(q\times\widetilde{q}\right)^2\right)\sigma_1\cdot\sigma_2 \\
& + \left(D_9 q^2 + \frac{D_{10}}{4}\widetilde{q}^2\right)\left(-i\frac{S}{2}\cdot\left(q\times\widetilde{q}\right)\right) + \left(D_{11} q^2 + \frac{D_{12}}{4}\widetilde{q}^2\right)\left(\sigma_1\cdot q\right)\left(\sigma_2\cdot q\right) \\
& + \frac{1}{4}\left(D_{13} q^2 + \frac{D_{14}}{4}\widetilde{q}^2\right)\left(\sigma_1\cdot\widetilde{q}\right)\left(\sigma_2\cdot\widetilde{q}\right) + \frac{D_{15}}{4}\left(\sigma_1\cdot\left(q\times\widetilde{q}\right)\sigma_2\cdot\left(q\times\widetilde{q}\right)\right) \qquad \text{(F.78)}
\end{aligned}
$$

We will use the results in Eqs. (F.10), (F.21), (F.32), (F.42) and (F.50). This yields

$$
\begin{aligned}
V^c_{\mathrm{N^3LO}} = \frac{1}{2\mathcal{V}}\sum_{\substack{k_1k_2\\p_1p_2}} & \Bigg\{ \left(D_1 - \frac{D_2}{16} + D_5 - \frac{D_6}{16}\right)\left(q^4 - \widetilde{q}^4\right) \\
& \quad + \left[q_z^2\left(D_{11}q^2 + \frac{D_{12}}{4}\widetilde{q}^2\right) - \widetilde{q}_z^2\left(D_{11}\widetilde{q}^2 + \frac{D_{12}}{4}q^2\right)\right] \\
& \quad + \left[\widetilde{q}_z^2\left(\frac{D_{13}}{4}q^2 + \frac{D_{14}}{16}\widetilde{q}^2\right) - q_z^2\left(\frac{D_{13}}{4}\widetilde{q}^2 + \frac{D_{14}}{16}q^2\right)\right]\Bigg\} \\
& \quad \times \Big[n_\uparrow(k_1,p_1)n_\uparrow(k_2,p_2) + n_\downarrow(k_1,p_1)n_\downarrow(k_2,p_2)\Big] \\
& -i\left(\frac{D_9}{2} + \frac{D_{10}}{8}\right)\left(q^2 + \widetilde{q}^2\right)\left(q\times\widetilde{q}\right)_z\Big[n_\uparrow(k_1,p_1)n_\uparrow(k_2,p_2) - n_\downarrow(k_1,p_1)n_\downarrow(k_2,p_2)\Big] \\
& + \Bigg\{\left(D_1 - D_5 - \frac{D_6}{8}\right)q^4 + \left(\frac{D_2}{16} - 2D_5 - \frac{D_6}{16}\right)\widetilde{q}^4 + \left(\frac{D_3}{4} - \frac{3D_7}{4}\right)q^2\widetilde{q}^2 \\
& \quad + \left(\frac{D_4}{4} - \frac{3D_8}{4}\right)\left(q\times\widetilde{q}\right)^2 - q_z^2\left(D_{11}q^2 + \frac{D_{12}}{4}\widetilde{q}^2\right) - \widetilde{q}_z^2\left(\frac{D_{13}}{4}q^2 + \frac{D_{14}}{16}\widetilde{q}^2\right) \\
& \quad - q_\perp^2\left(\frac{D_{13}}{4}\widetilde{q}^2 + \frac{D_{14}}{16}q^2\right) - \widetilde{q}_\perp^2\left(D_{11}\widetilde{q}^2 + \frac{D_{12}}{4}q^2\right) - \frac{D_{15}}{4}\left(q\times\widetilde{q}\right)^2\Bigg\} \\
& \quad \times \Big[n_\uparrow(k_1,p_1)n_\downarrow(k_2,p_2) + n_\downarrow(k_1,p_1)n_\uparrow(k_2,p_2)\Big]. \qquad \text{(F.79)}
\end{aligned}
$$

If $n_\uparrow = n_\downarrow = n$, then this simplifies to

$$V^{c}_{\mathrm{N^3LO}} = \frac{1}{2\mathcal{V}} \sum_{\substack{k_1 k_2 \\ p_1 p_2}} \Bigg\{ \left(2D_1 - \frac{D_2}{16} - \frac{3D_6}{16}\right) q^4 - \left(D_1 - \frac{D_2}{8} + 3D_5\right) \widetilde{q}^4 + \left(\frac{D_3}{4} - \frac{3D_7}{4}\right) q^2 \widetilde{q}^2 - \widetilde{q}^2 \left(D_{11}\widetilde{q}^2 + \frac{D_{12}}{4} q^2\right) - q^2 \left(\frac{D_{13}}{4}\widetilde{q}^2 + \frac{D_{14}}{16} q^2\right) + \left(\frac{D_4}{4} - \frac{3D_8}{4} - \frac{D_{15}}{4}\right) (q \times \widetilde{q})^2 \Bigg\} \times \Big[2n(k_1, p_1) n(k_2, p_2)\Big] \tag{F.80}$$

Two-pion exchange

At N^{3}LO, the two-pion exchange term has the form

$$V^{2\pi}_{\mathrm{N^3LO}} = U_C(q) + U_S(q)\,(\sigma_1 \cdot \sigma_2) + U_T(q)\,(\sigma_1 \cdot q)\,(\sigma_2 \cdot q) + U_{LS}(q) \left(-\frac{i}{2} S \cdot q \times \widetilde{q}\right) + \frac{1}{4} U_{\sigma L} \sigma_1 \cdot (q \times \widetilde{q})\, \sigma_2 \cdot (q \times \widetilde{q})\,, \tag{F.81}$$

with

$$U_X \equiv V_X + W_X, \quad X \in \{C, S, T, LS\}. \tag{F.82}$$

Just as with the N^{2}LO two-pion exchange terms, the functions V and W are defined in Ref. [135] and depend only on q and $\widetilde{q}$. Except for the $U_{\sigma L}$ term, these terms are of the same form as the ones for N^{2}LO (with different definitions of U_X). Thus,

$$
\begin{aligned}
V^{2\pi}_{\mathrm{N^3LO}} = \frac{1}{2\mathcal{V}} \sum_{\substack{k_1k_2\\p_1p_2}} \Bigg\{ \Bigg[& U_C(q) + U_S(q) + U_T(q) q_z^2 - U_C(\widetilde{q}) - U_S(\widetilde{q}) - U_T(\widetilde{q}) \widetilde{q}_z^2 \\
& + \left[\frac{U_{\sigma L}}{4}(q) - \frac{U_{\sigma L}}{4}(\widetilde{q}) \right] (q \times \widetilde{q})_z^2 \Bigg] \\
& \times \Big[n_\uparrow(k_1,p_1) n_\uparrow(k_2,p_2) + n_\downarrow(k_1,p_1) n_\downarrow(k_2,p_2) \Big] \\
+ \Bigg[& U_C(q) - U_S(q) - U_T(q) q_z^2 - 2U_S(\widetilde{q}) - U_T(\widetilde{q}) \left(\widetilde{q}_x^2 + \widetilde{q}_y^2 \right) \\
& - \left[\frac{U_{\sigma L}}{4}(q) \, (q \times \widetilde{q})_z^2 + \frac{U_{\sigma L}}{4}(\widetilde{q}) \left((q \times \widetilde{q})_x^2 + (q \times \widetilde{q})_x^2 \right) \right] \Bigg] \\
& \times \Big[n_\uparrow(k_1,p_1) n_\downarrow(k_2,p_2) + n_\downarrow(k_1,p_1) n_\uparrow(k_2,p_2) \Big] \Bigg\} \\
- \frac{i}{4\mathcal{V}} \sum_{\substack{k_1k_2\\p_1p_2}} \Bigg\{ & [U_{LS}(q) + U_{LS}(\widetilde{q})] \, (q_x \widetilde{q}_y - q_y \widetilde{q}_x) \\
& \times \Big[n_\uparrow(k_1,p_1) n_\uparrow(k_2,p_2) - n_\downarrow(k_1,p_1) n_\downarrow(k_2,p_2) \Big] \Bigg\}.
\end{aligned}
\tag{F.83}
$$

If $n_\uparrow = n_\downarrow = n$, then this simplifies to

$$
V^{2\pi}_{\mathrm{N^2LO}} = \frac{1}{2\mathcal{V}} \sum_{\substack{k_1k_2\\p_1p_2}} \left\{ \left[4U_C(q) - 2U_C(\widetilde{q}) - 4U_S(\widetilde{q}) - \frac{1}{2} U_{\sigma L} \, (q \times \widetilde{q})^2 \right] \Big[n(k_1,p_1) n(k_2,p_2) \Big] \right\}.
\tag{F.84}
$$

Appendix G

CHIRAL THREE-BODY INTERACTIONS

In this appendix, we detail more tedious calculations of chiral interaction terms, this time for three-body interactions.

G.1 General three-body potential

Consider the general three-body momentum space interaction term

$$\begin{aligned} H^{\mathrm{3NF}} &= \frac{1}{3!} \sum_{\substack{\lambda_1\lambda_2\lambda_2 \\ \rho_1\rho_2\rho_3}} \int \frac{d^3p_i}{(2\pi)^{15}} V(q_1,q_2,q_3) \\ &\qquad \times a^\dagger_{\rho_1}(k_1) M_{\rho_1\lambda_1} a_{\lambda_1}(p_1) a^\dagger_{\rho_2}(k_2) M_{\rho_2\lambda_2} a_{\lambda_2}(p_2) a^\dagger_{\rho_3}(k_3) M_{\rho_3\lambda_3} a_{\lambda_3}(p_3) \qquad \text{(G.1)} \\ &= \frac{1}{3!} \sum_{\substack{\lambda_1\lambda_2\lambda_2 \\ \rho_1\rho_2\rho_3}} \int \frac{d^3p_i}{(2\pi)^{15}} V(q_1,q_2,q_3) \\ &\qquad \times M_{\rho_1\lambda_1} M_{\rho_2\lambda_2} M_{\rho_3\lambda_3} a^\dagger_{\rho_1}(k_1) a^\dagger_{\rho_2}(k_2) a^\dagger_{\rho_3}(k_3) a_{\lambda_3}(p_3) a_{\lambda_2}(p_2) a_{\lambda_1}(p_1), \qquad \text{(G.2)} \end{aligned}$$

where $a^\dagger$, a are creation and annihilation operators and the particles have incoming (outgoing) momenta p_1, p_2, p_3 (k_1, k_2, k_3) and incoming (outgoing) spins λ_1, λ_2, λ_3 (ρ_1, ρ_2, ρ_3). The matrices $M_{\alpha\beta}$ are constant spin 2×2 matrices. And the integration is over $p_i \in \{p_1, p_2, p_3, k_1, k_2\}$ with k_3 given by momentum conservation.

First, we introduce the combined momentum-spin indices $I = (i, \alpha)$, $J = (j, \beta)$, and so on. Then the matrix element for this interaction is given by [134]

$$\langle \psi_{I_1}\psi_{I_2}\psi_{I_3} | H^{\mathrm{3NF}} | \phi_{J_1}\phi_{J_2}\phi_{J_3} \rangle = \int \frac{d^3q_1}{(2\pi)^3} \frac{d^3q_2}{(2\pi)^3} V(q_1,q_2,q_3) (\mathscr{M}_{I_1J_1}(q_1) \mathscr{M}_{I_2J_2}(q_2) \mathscr{M}_{I_3J_3}(q_3)), \qquad \text{(G.3)}$$

where

$$\mathscr{M}_{I_iJ_i}(q) = \int \frac{d^3p}{(2\pi)^3} \psi^*_{I_i}(p-q) M_{\alpha\beta} \phi_{J_i}(p). \qquad \text{(G.4)}$$

Let us further introduce the overlap of the Slater determinants Ψ and Φ with the notation

$$D_{\Psi\Phi} \equiv \det\{d_{IJ}\} = \langle\Psi|\Phi\rangle\,, \tag{G.5}$$

where $d_{IJ} = \langle\psi_I|\phi_J\rangle$. Then the final matrix element involves only integration over two transfer momenta

$$\begin{aligned}\langle\Psi|H^{3\mathrm{NF}}|\Phi\rangle = \frac{1}{3!}D_{\Psi\Phi}\int\frac{d^3q_1}{(2\pi)^3}\frac{d^3q_2}{(2\pi)^3}V(q_1,q_2,q_3)&\\ \times\sum_{\substack{I_1,I_2,I_3\\ J_1J_2J_3}}\mathscr{M}_{I_1J_1}(q_1)\mathscr{M}_{I_2J_2}(q_2)\mathscr{M}_{I_3J_3}(-q_1-q_2)&\begin{vmatrix} d^{-1}_{J_1I_1} & d^{-1}_{J_2I_1}d^{1}_{J_3I_1}\\ d^{-1}_{J_1I_2} & d^{-1}_{J_2I_2}d^{1}_{J_3I_2}\\ d^{-1}_{J_1I_3} & d^{-1}_{J_2I_3}d^{1}_{J_3I_3}\end{vmatrix}\end{aligned} \tag{G.6}$$

G.2 NLO

There is no genuine three-body force at NLO [135].

G.3 N²LO

The three-body forces start at N^{2}LO and are depicted in Fig. G.1. They are comprised of a long-range 2π-exchange term, an intermediate-range 1π-exchange term, and a short-range contact interaction. For neutron matter, the contact term and the 1π-exchange term both

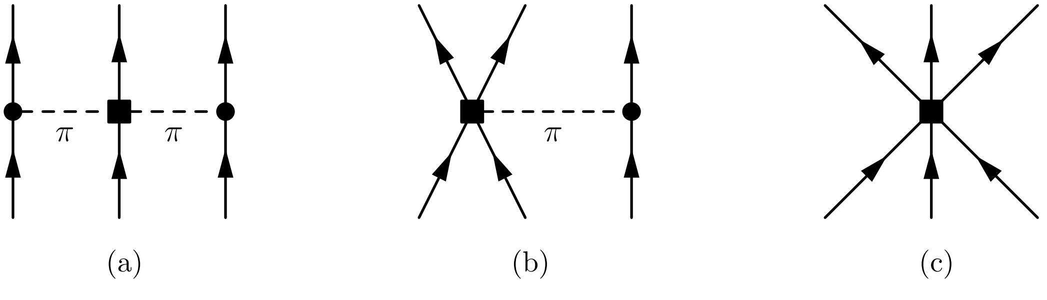

Figure G.1: Three-body interactions at N^{2}LO: (a) a long-range 2π-exchange component, (b) an intermediate-range 1π-exchange component, and (c) a short-range contact interaction.

vanish due to anti-symmetrization constraints [95]. So the only term that survives is

$$V_{2\pi}^{\mathrm{3NF}}(q_1, q_2, q_3) = \frac{g_A^2}{4f_\pi^4} \sum_{i \neq j \neq k} \frac{(\sigma_i \cdot q_i)(\sigma_j \cdot q_j)}{(q_i^2 + m_\pi^2)\big(q_j^2 + m_\pi^2\big)} \big[-2c_1 m_\pi^2 + c_3 q_i \cdot q_j\big] \tag{G.7}$$

Plugging this term into Eq. (G.6), we see that all 3! terms contribute equally, Switching to a discrete sum over momenta, we can write

$$\begin{aligned} \big\langle V_{\mathrm{N2LO}}^{\mathrm{3NF}} \big\rangle = {} & \frac{1}{\mathcal{V}^2} \sum_{q_1, q_2} V_{2\pi}^{\mathrm{3NF}\; ij}(q_1, q_2) \\ & \times \sum_{\substack{I_1 I_2 I_3 \\ J_1 J_2 J_3}} \mathscr{M}^i_{I_1 J_1}(q_1) \mathscr{M}^j_{I_2 J_2}(q_2) \mathscr{M}^0_{I_3 J_3}(-q_1 - q_2) \begin{vmatrix} d^{-1}_{J_1 I_1} & d^{-1}_{J_2 I_1} d^{1}_{J_3 I_1} \\ d^{-1}_{J_1 I_2} & d^{-1}_{J_2 I_2} d^{1}_{J_3 I_2} \\ d^{-1}_{J_1 I_3} & d^{-1}_{J_2 I_3} d^{1}_{J_3 I_3} \end{vmatrix}, \end{aligned} \tag{G.8}$$

where

$$V_{2\pi}^{\mathrm{3NF}\; ij}(q_1, q_2) = \frac{g_A^2}{4f_\pi^4} \frac{q_1^i q_2^j}{(q_1^2 + m_\pi^2)(q_2^2 + m_\pi^2)} \big[-2c_1 m_\pi^2 + c_3 q_1 \cdot q_2\big], \tag{G.9}$$

and the superscript on $\mathscr{M}$ carries through to the underlying sigma matrices, so that $M^i_{\alpha\beta} = \sigma^i_{\alpha\beta}$.

But we know that $d^{-1}_{IJ} = d^{-1}_{ij} \delta_{\alpha\beta}$ and that the leading $NN\pi$ vertex $\sim \sigma^i$, so only three contractions in the determinant are non-vanishing

$$\begin{vmatrix} d^{-1}_{J_1 I_1} & d^{-1}_{J_2 I_1} d^{1}_{J_3 I_1} \\ d^{-1}_{J_1 I_2} & d^{-1}_{J_2 I_2} d^{1}_{J_3 I_2} \\ d^{-1}_{J_1 I_3} & d^{-1}_{J_2 I_3} d^{1}_{J_3 I_3} \end{vmatrix} \to \underbrace{d^{-1}_{J_1 I_2} d^{-1}_{J_2 I_3} d^{-1}_{J_3 I_1}}_{A} + \underbrace{d^{-1}_{J_1 I_3} d^{-1}_{J_2 I_1} d^{-1}_{J_3 I_2}}_{B} - \underbrace{d^{-1}_{J_1 I_2} d^{-1}_{J_2 I_1} d^{-1}_{J_3 I_3}}_{C}, \tag{G.10}$$

where A and B represent genuine three body contributions and C represents a modified one-pion exchange.

Let us consider only the A contribution to the expectation value and separate the spin and momentum indices using $\mathscr{M}_{IJ} = \sigma_{\alpha\beta}\widetilde{\mathscr{M}}_{i,j}$ and $d^{-1}_{IJ} = d^{-1}_{ij}\delta_{\alpha\beta}$.

$$\begin{aligned}\left\langle V^{\text{3NF}}_{\text{N2LO}}\right\rangle^{(A)} = {}& \frac{1}{\mathcal{V}^2}\sum_{q_1,q_2} V^{\text{3NF}\;ij}_{2\pi}(q_1,q_2) \\ & \times \sum_{\substack{\alpha_1\alpha_2\alpha_3\\ \beta_1\beta_2\beta_3}}\sum_{\substack{i_1i_2i_3\\ j_1j_2j_3}} \sigma^i_{\alpha_1\beta_1}\sigma^j_{\alpha_2\beta_2}\delta_{\alpha_3\beta_3}\widetilde{\mathscr{M}}_{i_1j_1}(q_1)\widetilde{\mathscr{M}}_{i_2j_2}(q_2)\widetilde{\mathscr{M}}_{i_3j_3}(-q_1-q_2) \\ & \times d^{-1}_{j_1i_2}d^{-1}_{j_2i_3}d^{-1}_{j_3i_1}\delta_{\beta_1\alpha_2}\delta_{\beta_2\alpha_3}\delta_{\beta_3\alpha_1}. \end{aligned} \tag{G.11}$$

The δ-functions in Eq. (G.11) restrict the sums to $\alpha_3 = \beta_3 = \alpha_1 = \beta_2$ and $\alpha_2 = \beta_1$. So we have

$$\begin{aligned}\left\langle V^{\text{3NF}}_{\text{N2LO}}\right\rangle^{(A)} = {}& \frac{1}{\mathcal{V}^2}\sum_{q_1,q_2} V^{\text{3NF}\;ij}_{2\pi}(q_1,q_2) \\ & \times \sum_{\substack{i_1i_2i_3\\ j_1j_2j_3\\ \alpha_2\alpha_3}} \sigma^i_{\alpha_3\alpha_2}\sigma^j_{\alpha_2\alpha_3}\widetilde{\mathscr{M}}_{i_1j_1}(q_1)d^{-1}_{j_1i_2}\widetilde{\mathscr{M}}_{i_2j_2}(q_2)d^{-1}_{j_2i_3}\widetilde{\mathscr{M}}_{i_3j_3}(-q_1-q_2)d^{-1}_{j_3i_1} \end{aligned} \tag{G.12}$$

$$= \frac{1}{\mathcal{V}^2}\sum_{q_1,q_2} V^{\text{3NF}\;ij}_{2\pi}(q_1,q_2)\underbrace{\operatorname{Tr}\left(\sigma^i\sigma^j\right)}_{2\delta_{ij}}\operatorname{Tr}\left[\widetilde{\mathscr{M}}(q_1)d^{-1}\widetilde{\mathscr{M}}(q_2)d^{-1}\widetilde{\mathscr{M}}(-q_1-q_2)d^{-1}\right] \tag{G.13}$$

$$= \frac{2}{\mathcal{V}^2}\sum_{q_1,q_2} V^{\Sigma}_{2\pi}(q_1,q_2)\operatorname{Tr}\left[\widetilde{\mathscr{M}}(q_1)d^{-1}\widetilde{\mathscr{M}}(q_2)d^{-1}\widetilde{\mathscr{M}}(-q_1-q_2)d^{-1}\right], \tag{G.14}$$

where

$$V^{\Sigma}_{2\pi}(q_1,q_2) = \frac{g_A^2}{4f_\pi^4}\frac{q_1\cdot q_2}{(q_1^2+m_\pi^2)(q_2^2+m_\pi^2)}\left[-2c_1m_\pi^2 + c_3q_1\cdot q_2\right]. \tag{G.15}$$

We get the exact same result for part B so that

$$\left\langle V^{\text{3NF}}_{\text{N2LO}}\right\rangle^{(A+B)} = \frac{4}{\mathcal{V}^2}\sum_{q_1,q_2} V^{\Sigma}_{2\pi}(q_1,q_2)\operatorname{Tr}\left[\widetilde{\mathscr{M}}(q_1)d^{-1}\widetilde{\mathscr{M}}(q_2)d^{-1}\widetilde{\mathscr{M}}(-q_1-q_2)d^{-1}\right], \tag{G.16}$$

For part C, we have

$$\begin{aligned}\left\langle V^{\text{3NF}}_{\text{N2LO}}\right\rangle^{(C)} = {}& \frac{1}{\mathcal{V}^2}\sum_{q_1,q_2} V^{\text{3NF}\;ij}_{2\pi}(q_1,q_2) \\ & \times \sum_{\substack{\alpha_1\alpha_2\alpha_3\\ \beta_1\beta_2\beta_3}}\sum_{\substack{i_1i_2i_3\\ j_1j_2j_3}} \sigma^i_{\alpha_1\beta_1}\sigma^j_{\alpha_2\beta_2}\delta_{\alpha_3\beta_3}\widetilde{\mathscr{M}}_{i_1j_1}(q_1)\widetilde{\mathscr{M}}_{i_2j_2}(q_2)\widetilde{\mathscr{M}}_{i_3j_3}(-q_1-q_2) \\ & \times d^{-1}_{j_1i_2}d^{-1}_{j_2i_1}d^{-1}_{j_3i_1}\delta_{\beta_1\alpha_2}\delta_{\beta_2\alpha_1}\delta_{\beta_3\alpha_3}. \end{aligned} \tag{G.17}$$

The delta functions in Eq. (G.17) restrict the summation to $\alpha_3 = \beta_3$, $\alpha_1 = \beta_2$, and $\alpha_2 = \beta_1$. So we get

$$\begin{aligned}\left\langle V^{\text{3NF}}_{\text{N2LO}} \right\rangle^{(C)} &= \frac{1}{\mathcal{V}^2} \sum_{q_1,q_2} V^{\text{3NF}\; ij}_{2\pi}(q_1,q_2) \\ &\quad \times \sum_{\substack{i_1 i_2 i_3 \\ j_1 j_2 j_3 \\ \alpha_1\alpha_2\alpha_3}} \sigma^i_{\alpha_1\alpha_2}\sigma^j_{\alpha_2\alpha_1} \widetilde{\mathscr{M}}_{i_1 j_1}(q_1) d^{-1}_{j_1 i_2} \widetilde{\mathscr{M}}_{i_2 j_2}(q_2) d^{-1}_{j_2 i_1} \widetilde{\mathscr{M}}_{i_3 j_3}(-q_1-q_2) d^{-1}_{j_3 i_3} \end{aligned} \tag{G.18}$$

$$= \frac{2}{\mathcal{V}^2} \sum_{q_1,q_2} V^{\text{3NF}\; ij}_{2\pi}(q_1,q_2) \underbrace{\text{Tr}\big(\sigma^i\sigma^j\big)}_{2\delta_{ij}} \text{Tr}\Big[\widetilde{\mathscr{M}}(q_1)d^{-1}\widetilde{\mathscr{M}}(q_2)d^{-1}\Big] \text{Tr}\Big[\widetilde{\mathscr{M}}(-q_1-q_2)d^{-1}\Big] \tag{G.19}$$

$$= \frac{4}{\mathcal{V}^2} \sum_{q_1,q_2} V^{\Sigma}_{2\pi}(q_1,q_2) \,\text{Tr}\Big[\widetilde{\mathscr{M}}(q_1)d^{-1}\widetilde{\mathscr{M}}(q_2)d^{-1}\Big] \text{Tr}\Big[\widetilde{\mathscr{M}}(-q_1-q_2)d^{-1}\Big]. \tag{G.20}$$

Thus, the combined contributions are

$$\left\langle V^{\text{3NF}}_{\text{N2LO}} \right\rangle^{(A+B-C)} = \frac{4}{\mathcal{V}^2} \sum_{q_1,q_2} V^{\Sigma}_{2\pi}(q_1,q_2)[r(q_1,q_2) - \widetilde{m}(q_1,q_2)n(q_1+q_2)]. \tag{G.21}$$

where

$$r(q_1,q_2) \equiv \text{Tr}\Big(\widetilde{\mathscr{M}}(q_1)d^{-1}\widetilde{\mathscr{M}}(q_2)d^{-1}\widetilde{\mathscr{M}}(-q_1-q_2)d^{-1}\Big), \tag{G.22}$$

$$\widetilde{m}(q_1,q_2) \equiv \text{Tr}\Big(\widetilde{\mathscr{M}}(q_1)d^{-1}\widetilde{\mathscr{M}}(q_2)d^{-1}\Big), \tag{G.23}$$

and

$$n(q) \equiv \text{Tr}\Big(\widetilde{\mathscr{M}}(-q)d^{-1}\Big) \tag{G.24}$$